

Carnegie Mellon University

**Molecular Dynamics Study of Silicon
Thin Films Thermal Conductivity**

A DISSERTATION SUBMITTED TO THE CARNEGIE
INSTITUTE OF TECHNOLOGY IN PARTIAL FULFILLMENT
OF THE REQUIREMENTS

For the degree of

**DOCTOR OF PHILOSOPHY
IN
MECHANICAL ENGINEERING**

by
Carlos J. Gomes

**Pittsburgh, Pennsylvania
June 2005**

UMI Number: 3171946

INFORMATION TO USERS

The quality of this reproduction is dependent upon the quality of the copy submitted. Broken or indistinct print, colored or poor quality illustrations and photographs, print bleed-through, substandard margins, and improper alignment can adversely affect reproduction.

In the unlikely event that the author did not send a complete manuscript and there are missing pages, these will be noted. Also, if unauthorized copyright material had to be removed, a note will indicate the deletion.

UMI[®]

UMI Microform 3171946

Copyright 2005 by ProQuest Information and Learning Company.

All rights reserved. This microform edition is protected against unauthorized copying under Title 17, United States Code.

ProQuest Information and Learning Company
300 North Zeeb Road
P.O. Box 1346
Ann Arbor, MI 48106-1346

Carnegie Mellon University
CARNEGIE INSTITUTE OF TECHNOLOGY

THESIS

Submitted in Partial Fulfillment of the Requirements
For the Degree of doctor of Philosophy

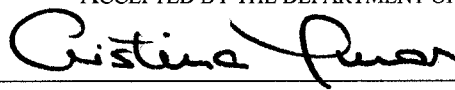

TITLE

**MOLECULAR DYNAMICS STUDY OF SILICON THIN FILMS
THERMAL CONDUCTIVITY**

PRESENTED BY


CARLOS J. GOMES

ACCEPTED BY THE DEPARTMENT OF MECHANICAL ENGINEERING

MAJOR PROFESSOR

DATE



6/28/05

DEPARTMENT HEAD

DATE

APPROVED BY THE COLLEGE COUNCIL



DEAN

7/1/05

DATE

To Ysomar

Acknowledgements

The path to this point in my life has been filled with countless faces and events. My professional and personal life has been highly enriched and changed by them.

I would like to thank my advisors Prof. Cristina Amon and Dr. Marcela Madrid for their guidance and support throughout my Ph.D. studies. I also thank my thesis committee members Prof. Mehdi Asheghi and Prof. Shi-Chune Yao for their comments and suggestions. Working with so many talented people has been a great experience and honor for me.

The financial support from the National Science Foundation (NSF) and Pittsburgh Infrastructure Technology alliance (PITA) grants is gratefully appreciated.

Abstract

Silicon thin films with dimensions in the nanometers are being increasingly used in silicon-on-insulator and strained silicon transistors. Experimental data at 300 K show that the in-plane thermal conductivity of thin films is as much as one order of magnitude smaller than bulk thermal conductivity at the same temperature. Therefore, it is essential to estimate the magnitude of the thermal conductivity of these films, in order to accurately design and predict the transistors' thermal response under operational conditions.

Heat in silicon is transported by phonons (the quantized lattice vibrations), the electronic contribution to heat transport is negligible below 1000 K. Molecular dynamics simulates the atomic motion and is used in this study to predict, for the first time, the in-plane thermal conductivity of silicon thin films. The film thicknesses and temperatures studied are between 2 and 217 nm and between 300 and 1000 K, respectively.

In this work, bulk silicon thermal conductivity is predicted to validate the computational code, and assess the influence of the simulation domain size and the periodic boundary conditions on the thermal conductivity predictions. The molecular dynamics studies show that not all the phonons present in bulk silicon are included in the simulation when using periodic boundary conditions. Nevertheless, our study shows that the predicted bulk silicon thermal conductivity is independent of the simulation domain size and the periodic boundary conditions, for domain sizes between $3 \times 3 \times 3$ and $10 \times 10 \times 10$ lattice constants per side, and temperatures between 300 and 1000 K. Our analytical studies, based on the Boltzmann transport equation, suggest that this non-dependency is due to an increment of the phonon relaxation time when using periodic boundary conditions.

The thermal conductivity of silicon thin films is predicted in the direction parallel (in-plane) to the film surfaces using equilibrium molecular dynamics, the Green-Kubo relation and the Stillinger-Weber interatomic potential. To treat the film surfaces, we propose to add to the Stillinger-Weber potential of the atoms that are near the film surfaces, a repulsive potential. We verify that equilibrium molecular dynamics simulations using this repulsive potential conserve energy, number of atoms and volume. Therefore, the repulsive potential strategy is suitable for the prediction of in-plane thermal conductivity of thin films using the Green-Kubo formalism. The molecular dynamics simulations show that the repulsive potential allows the reconstruction of the atoms on the (100) silicon surfaces into aligned dimes, in agreement with existing experimental and *ab initio* studies. Thus, molecular dynamics using the repulsive potential appears to be a valuable tool to realistically simulate silicon surfaces.

Two available strategies for the treatment of free surfaces are also used for equilibrium molecular dynamics predictions of in-plane thin film thermal conductivity: 1. adding four layers of atoms kept frozen at their bulk equilibrium positions and, 2. free surfaces. The repulsive potential or the two available strategies result in similar in-plane thermal conductivities predictions for film thicknesses larger than approximately 10 nm, at the temperatures investigated (376 and 1000 K). Thus, in the thick limit, the predicted thermal conductivities do not depend strongly on the exact potential used to treat the surface

atoms. However, for film thicknesses smaller than ~ 10 nm, the thermal conductivity predicted using atoms kept frozen is higher than that predicted with the other boundary conditions, and remains constant with the film thickness. The planar radial distribution function shows that using atoms kept frozen as boundary conditions affects the vibration of the atoms adjacent to the frozen layers, which accounts for these differences. The agreement between the in-plane thermal conductivity predicted using repulsive potential and free surfaces indicates that the repulsive potential is more accurate than atoms kept frozen to reproduce the physics of free (100) silicon surfaces. This observation may be important for predictions of non-homogeneous properties close to the film's surfaces even in the thick limit.

The repulsive potential boundary condition is then used to predict the in-plane thermal conductivity of silicon thin films. The predicted in-plane thermal conductivity follows the trend reported experimentally at 300 K, the magnitude of the thermal conductivity decreases as the film thickness decreases. This trend is also observed at 1000 K. In addition, the atomistic system captures the reduction of the phonon mean free path with temperature, since smaller film thickness are required to predict bulk thermal conductivity values at 1000 K than at 376 K. The predictions also show good agreement between the predicted thermal conductivity for thick films and the available experimental data for bulk silicon.

Table of Contents

List of Tables	viii
List of Figures	ix
Nomenclature	xiii
Chapter 1:	
Introduction	1
1.1 Motivation	1
1.2 Nanoscale Numerical Approaches	2
1.3 Thermal Conductivity Predictions	3
1.4 Objective	4
1.5 Thesis Organization	5
1.6 References	5
Chapter 2:	
Background and Computational Challenges	8
2.1 Thermal Transport in Silicon	8
2.2 Computational Procedure	8
2.2.1 The molecular dynamics technique	8
2.2.2 Interatomic potentials for silicon	9
2.2.3 Heat current definition	10
2.2.4 Green-Kubo relation for determining thermal conductivity	12
2.2.5 Quantum corrections	13
2.3 Computational Challenges	17
2.3.1 The parallel molecular dynamics code	17
2.3.2 Parallel molecular dynamics code validation and flowchart	19
2.4 Conclusions	20
2.5 References	22
Chapter 3:	
Bulk Silicon Thermal Conductivity	23
3.1 Determination of the Parameters Needed for the Molecular Dynamics Prediction of Silicon Thermal Conductivity	23
3.2 Bulk Silicon Thermal Conductivity	25
3.3 Bulk Silicon Simulation Size Artifacts	26
3.3.1 Phonon Wavelength Restrictions in Molecular Dynamics Simulations with Periodic Boundary Conditions	27
3.4 Conclusions	35

3.5 References	36
Chapter 4:	
In-Plane Thin Film Thermal Conductivity Prediction	38
4.1 Thin Film Surface Boundary Condition Review	38
4.2 Potential-Like Boundary Condition	39
4.3 Repulsive Potential: Further Considerations and Validation	41
4.3.1 Microcanonical Ensemble Verification	41
4.3.2 Green-Kubo Relation for Determining the In-Plane Thermal Conductivity	43
4.3.3 Quantum Corrections for the In-Plane Thermal Conductivity	44
4.3.4 Insensitivity of the Predicted In-Plane Thermal Conductivity to the Repulsive Potential Parameters	44
4.3.5 Size Artifacts	45
4.3.6 Surface Reconstruction	48
4.4 In-Plane Thermal Conductivity Calculations	49
4.4.1 Simulation Domain and Boundary Conditions Definition	50
4.4.2 Results	52
4.4.3 In-Plane Silicon Thin Films Thermal Conductivity: Additional Results	56
4.5 In-plane Autocorrelation Time	56
4.6 Conclusions	58
4.7 References	59
Chapter 5:	
Conclusions and Future Work	61
5.1 Conclusions	61
5.2 Future Work	64
5.3 References	65
Appendix A:	
Boltzmann Transport Equation	66
A.1 Boltzmann Transport Equation in the Relaxation Time Approximation	66
A.2 Phonon Bands Approach	67
A.3 Bulk Thermal Conductivity Equation	68
A.4 Relaxation Times and Scattering Rules	69
A.5 Phonon Wavelength Restriction	72
A.6 References	72
Appendix B:	
Molecular Dynamics Thermal Conductivity Data	73
B.1 Bulk Thermal Conductivity	73
B.2 In-Plane Thin Film Thermal Conductivity	73

LIST OF TABLES

Table	Description	Page
2.2.1	Stillinger-Weber potential's constants for silicon.	9
2.2.2	Quantum correction factors determined from the experimental specific heat (T_c and k_c) and analytically (T_a and k_a).	16
2.3.1	Time benchmarks for the serial code (run on a 1.4GHz processor).	16
3.1.1	Predicted bulk silicon thermal conductivity for different values of the lattice parameter a_0 .	25
4.2.1	Repulsive potential parameters.	41
4.3.1	Comparison of the out-of-plane phonon frequencies captured by the molecular dynamics simulation of a $2 \times 2 \times 48$ lattice constants silicon thin film to the phonon frequencies predicted using the allowed wavelength in the out-of-plane direction.	48
4.3.2	Distance between atoms in a dimer in a (100) reconstructed silicon surface, predicted by means of molecular dynamics (MD), <i>ab initio</i> simulations and Low-Energy Ion Scattering Spectroscopy (ISS) studies.	49
4.4.1	Fraction of the in-plane thermal conductivity to the experimental bulk thermal conductivity at 376 and 1000 K.	56
B.1.1	Bulk silicon thermal conductivity.	73
B.2.1	In-plane thin film thermal conductivity predicted using the repulsive potential.	74
B.2.2	In-plane thin film thermal conductivity predicted using atoms kept frozen.	75
B.2.3	In-plane thin film thermal conductivity predicted using free surfaces.	75

LIST OF FIGURES

Figure	Description	Page
2.2.1	Silicon lattice (4x4x4 lattice constants) depicting the atoms as spheres and the atomic bonds as lines. The inset shows a silicon molecule.	9
2.2.2	Time evolution of (a) the heat current's convective term (first term in Eq. (2.2.7)) and the conductive terms: (b) two body and (c) three-body contributions, (second and third terms of Eq. (2.2.7) respectively). The results are for 5x5x5 silicon cells at 1000 K. The figure shows that for condensed matter the convective term is negligible with respect to the conductive ones.	11
2.2.3	Time evolution of the heat current autocorrelation function, (b) thermal conductivity variation with the integration time. Both for a 5x5x5 silicon cells at $T = 248$ K.	12
2.2.4	Variation of the quantum corrections for (a) the thermal conductivity and (b) the temperature, for Debye temperatures ranging from 600 to 700 K.	15
2.2.5	Quantum corrected temperature (right axis), and ratio of quantum corrected to molecular dynamics predicted thermal conductivity (k/k_{MD}) (left axis), as a function of the temperature of the MD simulations for silicon.	15
2.3.1	CPU time per step of molecular dynamics as a function of the number of atoms for different numbers of 450MHz processors, showing a linear dependence with the number of atoms.	17
2.3.2	Two-dimensional example illustrating the ghost cell strategy used for code parallelization.	18
2.3.3	CPU time per step of molecular dynamics versus number of processors, for number of atoms ranging from 2,744 to 110,592. Simulations were performed on the CRAY T3E at the Pittsburgh Supercomputing Center.	19
2.3.4	Flowchart of the serial and parallel molecular dynamics code.	21

Figure	Description	Page
3.1.1	Variation of the predicted bulk silicon thermal conductivity with the number of samples used to average the heat current autocorrelation function.	24
3.2.1	Bulk silicon thermal conductivity vs temperature for different simulation domain sizes and comparison with experimental results for natural silicon.	26
3.3.1	Variation of the pure silicon thermal conductivity with the simulation domain size for different temperatures.	27
3.3.2	Frequency spectra of the atomic velocities at 1000 K for (a) 4x4x4, (b) 5x5x5 and (c) 7x7x7 lattice constant domains.	28
3.3.3	Experimental silicon dispersion relation in the [100] crystallographic direction (Holland 1963). The dashed portion represents the phonons that are omitted from the molecular dynamics simulation because of periodic boundary conditions restrictions.	30
3.3.4	Variation of the BTE predicted bulk silicon thermal conductivity with wavelength cutoff for different temperatures (500 bands per acoustic polarization).	31
3.3.5	Contribution to the bulk thermal conductivity of the phonon bands (50 bands per acoustic polarization).	32
3.3.6	BTE predicted bulk silicon thermal conductivity including wavelength cutoff and filtering (50 bands per acoustic polarization).	36
3.3.7	Phonon bands' relaxation times for (a) longitudinal acoustic and (b) transversal acoustic at 300 K, computed using the phonon band approximation and the phonon filtering.	34
3.3.8	Band contribution to the thermal conductivity for a system with all the phonon bands and for a system with filtered bands.	34
4.1.1	(a) Sketch of a thin film defining the in-plane and out-of-plane directions and the film thickness d_s . (b) Molecular dynamics simulation domain consisting of 4x4x8 silicon lattice constants.	39

Figure	Description	Page
4.2.1	(a) Sketch of the repulsive potential reference point, reference plane, unit vector and distance d ; (b) Sketch of the repulsive potential location with respect to the thin film atoms.	41
4.3.2	Fluctuation of the heat flux through the film surface for a 7x7x8 lattice constants simulation at 1000 K.	43
4.3.3	Standard deviation of the heat flux through the film surface vs cross section size.	44
4.3.4	Variation of the repulsive potential (non-dimensional) with distance from the reference plane (non-dimensional) for values of ϵ given in the direction of the arrow of 0.5ϵ , ϵ , 2ϵ and 5ϵ .	45
4.3.5	Influence of simulation cross-section size on the predicted thermal conductivity for repulsive potential boundary condition.	46
4.3.6	Phonon spectra of a 2x2x8 lattice constants silicon thin film in (a) the in-plane direction and (b) the out-of-plane direction.	47
4.3.7	Phonon spectra of a 2x2x2 lattice constants bulk silicon simulation.	47
4.3.8	(a) Starting configuration of atoms located at the surface of a film of 10x10 silicon lattice constants cross section and 4.34 nm (8 lattices) thick. (b) Silicon surface reconstruction of the same thin film after 100,000 steps of molecular dynamics, showing the individual dimes oriented in [110] crystallographic direction and group of dimes aligning in $[\bar{1}\bar{1}0]$ direction.	48
4.4.1	Front view of: (a) Silicon film with repulsive potential at both free surfaces. (b) Silicon film with free surfaces. (c) Silicon film with four layers of frozen atoms delimiting each surface.	51
4.4.2	In-plane silicon thin film thermal conductivity at 300 K.	53
4.4.3	In-plane silicon thin film thermal conductivity at 1000 K.	53
4.4.4	Two-dimensional radial distribution function for the film's (a) center layer, (b) third layer from the surface, (c) second layer from the surface and (d) the surface layer. The two-dimensional radial distribution function computed using the repulsive potential and free boundary condition are overlapped in all the plots.	55

Figure	Description	Page
4.4.5	In-plane thermal conductivity vs ensemble temperature for different film thicknesses.	57
4.5.1	Variation of the time integral of the in-plane heat-current-autocorrelation-function for different film thickness.	58
A.2.1	Discrete acoustic dispersion curves using (a) equal size frequency bands and (b) equal size reduced wavenumber bands.	67
A.3.1	Variation of the thermal conductivity with temperature, predicted using the Boltzmann transport equation.	69
A.4.1	Longitudinal and transversal polarizations that undergo $T+T_{\text{zone}} \leftrightarrow L$ scattering processes while satisfying energy conservation.	70
A.4.2	Phonon band relaxation times vs. reduce wavenumber for (a) $T+L_{\text{zone}} \leftrightarrow L$, (b) $L+T_{\text{zone}} \leftrightarrow L$, (c) $T+T_{\text{zone}} \leftrightarrow L$, (d) $L+L_{\text{zone}} \leftrightarrow O$, (e) $T+L_{\text{zone}} \leftrightarrow O$ scattering rules, and (f) total relaxation time.	71

Nomenclature

a	lattice constant, m
A	two-body interatomic potential well depth factor
A_s	simulation cross section area, m ²
B	two-body interatomic potential repulsive factor
C	specific heat, W/m ³ K
d_w	distance between an atom and the repulsive potential reference plane, m
d_s	thin film thickness, nm
E_i	total energy stored in atom i , J
\vec{F}_i	total force on atom i , N
\vec{F}_{ij}^i	force on atom i due to the two-body interaction with atom j , N
\vec{F}_{jik}^i	force on atom i due to the three-body interaction with atom j and k , N
\vec{F}_{iw}^i	force on atom i due to the repulsive potential, N
\vec{J}	heat current, J/m ²
J_{cond}	heat current conductive term, Jm/s
J_{conv}	heat current convective term, Jm/s
\vec{J}_w	heat flux through the film surface, J/m ²
K_l	longitudinal acoustic thermal conductivity, W/mK
K_t	transversal acoustic thermal conductivity, W/mK
k	thermal conductivity, W/mK
k_B	Boltzmann's constant, 1.3807×10^{-23} J/K
k_{ip}	thin-film in-plane thermal conductivity, W/mK
k_{MD}	molecular dynamic determined thermal conductivity, W/mK
k_{oop}	thin-film out-of-plane thermal conductivity, W/mK
M	number of sampling steps
m_i	atomic mass of atom i , kg
N	number of atoms in the ensemble
N_s	number of heat current autocorrelation function averages
N_w	number of atoms within the repulsive potential cutoff radius
\vec{n}	unit vector perpendicular to the reference plane
$\langle n \rangle$	average phonon occupation number
p	two-body potential short-distance repulsive term power
q	two-body potential long-distance attractive term power
r_c	two- and three-body potential dimensionless cutoff radius

r_{cw}	repulsive potential dimensionless cutoff radius.
\vec{r}_{ij}	vectorial distance between particles i and j , m
r_{ij}	magnitude of the distance between particles i and j , m
\vec{r}_{ik}	vectorial distance between particles i and k , m
r_{ik}	magnitude of the distance between particles i and k , m
T	temperature, K
t	time, s
U_i	total potential energy stored in atom i , J
V	volume, m ³
\vec{v}_i	velocity of atom i , m/s
\vec{x}_i	position of atom i , m

Greek symbols

Δt	delta time, s
$\Delta\omega_i$	phonon frequency band, THz
ε	repulsive potential scaling factor, J
ϕ_2	two-body interatomic potential energy
ϕ_3	three-body interatomic potential energy
ϕ_w	one-body repulsive potential, J
γ	three-body interatomic potential cutoff factor
λ	three-body interatomic potential, well depth factor and phonon wave length
Λ	phonon mean free path
σ	one-body, two-body and three-body potential characteristic distance, nm
θ_{ijk}	angle between vectors \vec{r}_{ij} and \vec{r}_{ik} , radians
θ_D	Debye's temperature, K
τ_i	relaxation time for phonon band i , s
ω	frequency, THz

Chapter 1:

Introduction

1.1 Motivation

The constant demand for faster electronic devices, larger amount of portable storage capacity and the development of new microfabrication technologies have resulted in transistors with dimensions on the order of nanometers. One consequence of such miniaturization is that higher transistor packing densities can be achieved, resulting in smaller overall sizes and increased capabilities. For example, the overall size of cell phones has not only been reduced over the past decades, but extra capabilities, such as personal digital assistants, larger amounts of memory banks, better noise filters and picture processing, among others, have been added. Other everyday equipment improved with electronic device miniaturization and high device packing includes laptops, desktops, digital cameras, portable memory banks, health related equipment and military technology.

The silicon-on-insulator (SOI) transistor and the strained silicon (SS) transistor are among the transistor technologies available in today's market. SOI transistors are made of a single-crystal silicon film lying on top of a silicon dioxide matrix, while SS transistors are single-crystal strained silicon film lying on top of a Silicon-Germanium ($\text{Si}_{0.8}\text{Ge}_{0.2}$) layer. The transistor speed is increased by reducing the transistor overall dimensions. Reducing the transistor's dimensions reduce the capacitance of the transistor and the time required to switch from on to off, thereby increasing the transistor speed. The high transistor density is achieved by the high electrical resistance of the substrates, which prevent electrical leakage between transistors. The International Technology Roadmap for Semiconductors (<http://public.itrs.net/>) indicates that the transistor's gate length (the transistor's characteristic dimension) could reach 28 nm by the year 2009. It can be inferred from these predictions that the transistor industry is planning to develop smaller size transistors for at least one more decade. However, heat dissipation in these transistors could become a limiting factor as the transistor's dimensions are further miniaturized.

The heat generated by the Joule effect in the zone of high electronic activity (the transistor's gate) is mostly dissipated along the silicon thin film because the silicon dioxide and the $\text{Si}_{0.8}\text{Ge}_{0.2}$ substrates have a significantly smaller thermal conductivity ($k_{\text{oxide}} \sim 1\text{W/mK}$ (Sverdrup, Ju et al. 2001; Pop, Sinha et al. 2002), $k \sim 5\text{W/mK}$ (Abeles, Beers et al. 1962; Liu and Asheghi 2004)). Early analytical studies (Flik, Choi et al. 1992) showed that the magnitude of the in-plane and the out-of-plane silicon thin films thermal conductivity can be significantly smaller than that of bulk silicon at the same temperature. Recently, experimental determination of silicon thin films' thermal conductivity for film thickness down to 74 nm (Ju and Goodson 1999), and 20 nm (Liu and Asheghi 2004; Liu and Asheghi 2005) at 300 K have shown that reducing the film thickness reduces the in-plane thermal conductivity. The reduction in the magnitude of

the thin film thermal conductivity is a consequence of the additional resistance to the thermal energy flow imposed by the proximity of the film surfaces. Thus, decreasing the thickness of the silicon thin film results not only in a smaller transversal area for heat dissipation but also in smaller silicon thermal conductivity magnitudes, which can lead to overheating of the transistor. The overheating negatively affects the performance and reliability of the transistors. Therefore, an accurate prediction of the silicon thin film thermal conductivity for different film thicknesses and temperatures is important for the transistor industries, in order to properly design next-generation transistors. Currently, experimental data for in-plane silicon thin film thermal conductivity is available for temperatures below 450 K (Liu and Asheghi 2004; Liu and Asheghi 2005). To our knowledge, experimental data for the out-of-plane thermal conductivity of silicon thin films has not been reported. In this study, we complement this knowledge with the molecular dynamics predictions of in-plane silicon thermal conductivity for temperatures between 240 to 1000 K and film thickness of 2 to 217 nm.

1.2 Nanoscale Numerical Approaches

Due to the nature of its electronic configuration, the thermal energy in silicon is transported by phonons (Ashcroft and Mermin 1976), i.e. the quanta of the lattice vibration. Predictions of thin films' thermal conductivities require an accurate description of the phonons' transport in the nanometer regime, and their contribution to the thermal conductivity. Due to the particle-like characteristic of the phonons, the Boltzmann Transport Equation (BTE), which describes the transport and interaction among particles, is used to estimate lattice thermal conductivity (Holland 1963). The BTE describes the phonons' transport by means of a diffusive term and the phonons' interactions by means of a scattering term. The integral-differential scattering term is commonly modeled by means of the relaxation time approximation (Ziman 1960; Narumanchi, Murthy et al. 2003; Escobar and Amon 2004; Narumanchi, Murthy et al. 2004). In this approximation, the scattering term is taken to be proportional to the difference between the phonons' equilibrium distribution for the given temperature divided by the actual distribution to the average time required to reach equilibrium, i.e. the relaxation time. Models describing the interactions (scattering) among phonons have been developed (Klemens 1958; Han and Klemens 1993; Tamura, Tanaka et al. 1999). Additionally, models have been developed to account for the scattering between phonons and vacancies/impurities/isotopes (Klemens 1958; Balandin 1998; Tamura, Tanaka et al. 1999). It is through the relaxation time that the models developed for the different scattering mechanism enter the BTE. Finally, the scattering models have been validated via predictions of bulk silicon thermal conductivity at different temperatures (Holland 1963; Narumanchi 2003; Escobar 2005). These studies assume that the phonon properties (dispersion relation and relaxation time) are isotropic and equal to the phonon properties in the [100] crystallographic direction. More recent BTE-based numerical approaches (Narumanchi, Murthy et al. 2004) incorporate the phonon-phonon scattering mechanisms by using individual scattering terms for each possible phonon-phonon scattering mechanism. The individual scattering terms are simplified by the relaxation time approximation, where the phonon-phonon relaxation times are computed using perturbation

theory (Klemens 1958; Han and Klemens 1993). This approach is also validated by predicting the bulk silicon thermal conductivity, where the Grüneisen parameter is used as the tuning parameter (Narumanchi, Murthy et al. 2004).

The phonon-surface scattering mechanism present in thin films has been incorporated in different BTE-based numerical approaches through a combination of the specularly parameter and the reduction the magnitude of the phonon mean free path (MFP), i.e. the average distance between phonons collisions, as a function of the film thickness (Narumanchi 2003; Chantrenne and Barrat 2004; Liu and Asheghi 2004). This method have been tuned by predicting the in-plane silicon thin film thermal conductivity at 300 K and comparing it to the available experimental data.

BTE-based approaches offer a tremendous potential to model phonon transport. However, the parameters need to be tuned with existing experimental data. To predict bulk silicon thermal conductivity, BTE equation is solved at a time scale and length scales much larger than the phonons' relaxation time and mean free path, respectively. Different mathematical expressions can be used for these quantities and still reproduce the bulk silicon thermal conductivity over the solid-state temperature span (Chung, McGaughey et al. 2004). Studies towards the numerical prediction of the relaxation times (McGaughey and Kaviany 2004) and phonon scattering rules (Sinha, Schelling et al. 2003) are being performed.

A numerical technique that takes into account the discreteness of the crystalline structure, and does not incorporate semi empirical formulations of the thermal energy carrier behavior, can be an important complement to existing methodologies to predict the thin silicon thermal conductivity. In this work, the molecular dynamics technique is used to predict thermal conductivities, because it readily provides the lattice thermal conductivity. Additionally, no assumptions are made about any of the phonon scattering rules, since they are intrinsically incorporated in the method. Numerical techniques that incorporate the electronic configuration of the atoms, *ab initio* methods (Hirst 1990), are not considered since they are computationally prohibitive.

1.3 Thermal Conductivity Predictions

Different methods have been developed to calculate thermal conductivities using molecular dynamics (MD). The non-equilibrium molecular dynamics (NEMD) method consists of artificially imposing either a temperature gradient or a heat flux (Müller-Plathe 1997; Jund and Jullien 1999; Lukes, Li et al. 2000; Daly and Maris 2002; Schelling, Phillpot et al. 2002) in a specific direction and computing the thermal conductivity in this direction by means of Fourier's law. The equilibrium molecular dynamics (EMD) uses the Green-Kubo relation (McQuarrie 1976; Allen and Tildesley 1987; Frenkel and Smit 2001) between the thermal conductivity and the time integral of the heat current autocorrelation function.

The bulk thermal conductivities predicted with EMD and NEMD are in good agreement with experimental results (Volz and Chen 1999; Lukes, Li et al. 2000; Volz and Chen 2000; Schelling, Phillpot et al. 2002) and are within the statistical error of each other (Schelling, Phillpot et al. 2002). However, the thermal conductivity computed using the NEMD method is more sensitive to the simulation-domain size

than the thermal conductivity computed with EMD (Schelling, Phillpot et al. 2002). In order to obtain domain-size independent thermal conductivity using NEMD, several simulations have to be performed for different domain lengths in order to linearly extrapolate the bulk thermal conductivity, which is computationally expensive (Schelling, Phillpot et al. 2002). To our knowledge, there are no previous molecular dynamics predictions of in-plane silicon thin film thermal conductivity using either non-equilibrium or equilibrium molecular dynamics. The prediction of the in-plane silicon thin films thermal conductivity with non-equilibrium or equilibrium molecular dynamics (NEMD) may require a rather large number of atoms, since not only all the atoms in the out-of-plane direction have to be included to properly account for the surface scattering, but also enough atoms in the in-plane direction to accurately extrapolate the thermal conductivity to its thin film value (these conclusions are drawn based on Schelling et al. works for bulk silicon (Schelling, Phillpot et al. 2002)). Therefore, using NEMD for the prediction of in-plane silicon thin films thermal conductivity may be very computationally intensive even with today's available hardware. Based on this observation, in this work we use the EMD approach.

Previously, molecular dynamics have been successfully used to predict the bulk thermal conductivity of crystalline materials, such as pure argon (Lukes, Li et al. 2000), diamond (Che, Çagin et al. 2000) and silicon (Volz and Chen 1999; Volz and Chen 2000), SiGe (Volz, Saulnier et al. 2000) and GaAs (Daly and Maris 2002) superlattices, silicon nanowires (Volz and Chen 1999), silica based crystal (McGaughey and Kaviani 2002) and amorphous materials, silicon (Lee, Biswas et al. 1991) and germanium (Ding and Andersen 1986). Out-of-plane thin-film thermal conductivities have been predicted using non-equilibrium molecular dynamics (Lukes, Li et al. 2000; Feng, Li et al. 2001; Choi and Maruyama 2003; Feng, Li et al. 2003; Chantrenne and Barrat 2004). These studies focus on solid argon (Lukes, Li et al. 2000; Feng, Li et al. 2001; Choi and Maruyama 2003; Chantrenne and Barrat 2004) and on silicon at 500 K (Feng, Li et al. 2003).

1.4 Objective

This thesis presents the first molecular dynamics predictions of silicon thin film thermal conductivities using equilibrium molecular dynamics and the Green-Kubo formalism. This is achieved by first computing bulk silicon thermal conductivity to validate the computational code and address the dependence of the thermal conductivity on the periodic boundary conditions. Then, a boundary condition that takes into account the physics of the interactions between the atoms at the film's surface and a static isothermal gas is introduced for the treatment of the films surfaces. The feasibility of using the repulsive potential with the Green-Kubo relation is numerically verified. The in-plane thermal conductivity is predicted for film thicknesses ranging from 2 to 217 nm and temperatures of the molecular dynamics simulation (T_{MD}) equal to 400 and 1000 K. The predictions at 400 K are compared to existing experimental silicon thin film thermal conductivity data (Ju and Goodson 1999; Liu and Asheghi 2004; Liu and Asheghi 2005), while the predictions at 1000 K allow the verification of bulk behavior as the film's thickness increases.

1.5 Thesis Organization

Chapter 2 presents a review of the molecular dynamics technique and describes the computational procedure to compute bulk thermal conductivity using the Green-Kubo formalism and the Stillinger-Weber potential for silicon. The computational challenges and the quantum corrections are also addressed in this chapter.

Chapter 3 presents the numerical simulations and analyses of the predicted bulk silicon thermal conductivity using equilibrium molecular dynamics technique. Also presented in this Chapter is a discussion, based on the Boltzmann transport equation, of the independence of the molecular dynamics predicted bulk silicon thermal conductivity to the size of the simulation domain.

Chapter 4 presents the numerical prediction of the in-plane silicon thin film thermal conductivity using equilibrium molecular dynamics and the Green-Kubo formalism. A review of the boundary conditions used in molecular dynamics is presented, and a new set of boundary conditions, that takes into consideration the physics of a free-standing thin film surrounded by an isothermal, macroscopically static and inert gas, is introduced. Last, the silicon thin film thermal conductivity is predicted for temperatures ranging from 240 to 1000 K.

Chapter 5 presents the conclusion from this thesis and describes the future work.

1.6 References

- Abeles, B., D. S. Beers, et al. (1962). "Thermal Conductivity of Ge-Si Alloys at High Temperatures." Physical Review **125**(1): 44-46.
- Allen, M. P. and D. J. Tildesley (1987). Computer Simulation of Liquids. Oxford, UK, Clarendon Press.
- Ashcroft, N. W. and N. D. Mermin (1976). Solid State Physics. New York, Harcourt College Publishers.
- Balandin, A., and Wang, K.L. (1998). "Significant Decrease of the Lattice Thermal Conductivity due to Phonon Confinement in a Free-standing Semiconductor Quantum Well." Physical Review B **58**(3): 1544-1549.
- Chantrenne, P. and J.-L. Barrat (2004). "Finite Size Effects in Determination of Thermal Conductivities: Comparing Molecular Dynamics Results with Simple Models." Journal of Heat Transfer **126**: 577-585.
- Che, J., T. Çagin, et al. (2000). "Thermal Conductivity of Diamond and Related Materials from Molecular Dynamics Simulations." Journal of Chemical Physics **113**(16): 6888-6900.
- Choi, S.-H. and S. Maruyama (2003). "Evaluation of the Phonon Mean Free Path in Thin Films by Using Classical Molecular Dynamics." Journal of the Korean Physical Society **43**(5): 747-753.
- Chung, J. D., A. J. H. McGaughey, et al. (2004). "Role of Phonon Dispersion in Lattice Thermal Conductivity Modeling." Journal of Heat Transfer **126**: 376-380.
- Daly, B. C. and H. J. Maris (2002). "Calculation of the Thermal Conductivity of Superlattices by Molecular Dynamics Simulation." Physica B **316-317**: 247-249.
- Ding, K. and H. C. Andersen (1986). "Molecular-Dynamics Simulation of Amorphous Germanium." Physical Review B **34**(10): 6987-6991.
- Escobar, R. (2005). In Preparation. Mechanical Engineering. Pittsburgh, Carnegie Mellon University.
- Escobar, R. A. and C. H. Amon (2004). Lattice-Boltzmann Modeling of Sub-Continuum Energy Transport in Silicon-on-Insulator Microelectronics Including Dispersion Effects. Thermal and Thermomechanical Phenomena in Electronic Systems, Las Vegas, Nevada, USA.

- Feng, X.-L., Z.-X. Li, et al. (2003). "Molecular Dynamics Simulation of Thermal Conductivity of Nanoscale Thin Silicon Films." Microscale Thermophysical Engineering 7: 153-161.
- Feng, X.-L., Z.-X. Li, et al. (2001). "Molecular Dynamics Study on Thermal Conductivity of Nanoscale Thin-Films." Chinese Science Bulletin 46(7): 604-607.
- Flik, M. I., B. I. Choi, et al. (1992). "Heat Transfer Regimes in Microstructures." Journal of Heat Transfer 114: 666-674.
- Frenkel, D. and B. Smit (2001). Understanding Molecular Simulation from Algorithms to Applications. New York, Academic Press.
- Han, Y.-J. and P. G. Klemens (1993). "Anharmonic Thermal Resistivity of Dielectric Crystals at Low Temperatures." Physical Review B 48(9): 6033-6042.
- Hirst, D. M. (1990). A Computational Approach to Chemistry. Oxford London, Blackwell Scientific Publications.
- Holland, M. G. (1963). "Analysis of Lattice Thermal Conductivity." Physical Review 132(6): 2461-2471.
- Ju, Y. S. and K. E. Goodson (1999). "Phonon Scattering in Silicon Thin Films with Thickness of Order 100 nm." Applied Physics Letters 74(20): 3005-3007.
- Jund, P. and R. Jullien (1999). "Molecular Dynamics Calculation of the Thermal Conductivity of Vitreous Silica." Physical Review B 59(21): 13707-13711.
- Klemens, P. G. (1958). Thermal Conductivity and Lattice Vibrational Modes. Solid State Physics. F. Seitz and D. Turnbull. New York, Academic Press. 7: 1-98.
- Lee, Y. H., R. Biswas, et al. (1991). "Molecular-Dynamics Simulation of Thermal Conductivity in Amorphous Silicon." Physical Review B 43(8): 6573-6580.
- Liu, W. and M. Asheghi (2004). "Phonon-Boundary Scattering in Ultrathin Single-Crystal Silicon Layers." Applied Physics Letters 84(19): 3819-3821.
- Liu, W. and M. Asheghi (2004). Thermal Modeling of Self-Heating in Strained-Silicon MOSEFTs. Thermal and Thermomechanical Phenomena in Electronic Systems, Las Vegas, Nevada, USA.
- Liu, W. and M. Asheghi (2005). Thermal Conduction in Ultra-Thin Pure and Doped Single Crystal Silicon Layers at High Temperatures. 2005 ASME Summer Heat Transfer Conference, San Francisco, CA, USA.
- Lukes, J. R., D. Y. Li, et al. (2000). "Molecular Dynamics Study of Solid Thin-Film Thermal Conductivity." Journal of Heat Transfer 122: 536-543.
- McGaughey, A. J. and M. Kaviani (2004). "Quantitative Validation of the Boltzman Transport Equation Phonon Thermal Conductivity Model Under the Single-Mode Relaxation Time Approximation." Physical Review B 69(9): 094303(1)-094303(11).
- McGaughey, A. J. H. and M. Kaviani (2002). Molecular Dynamics Calculations of the Thermal Conductivity of Silica Based Crystal. 8th AIAA/ASME Joint Thermophysics and Heat Transfer Conference, St. Louis, MO.
- McQuarrie, D. A. (1976). Statistical Mechanics. New York, Harper Collins.
- Müller-Plathe, F. (1997). "A Simple Nonequilibrium Molecular Dynamics Method for Calculating the Thermal Conductivity." Journal of Chemical Physics 106(14): 6082-6085.
- Narumanchi, S. V. J. (2003). Heat Transport in Sub-micron Conduction. Mechanical Engineering. Pittsburgh, Ph.D. thesis, Carnegie Mellon University.
- Narumanchi, S. V. J., J. Y. Murthy, et al. (2003). "Simulation of Unsteady Small Heat Source Effects in Sub-micron Heat Conduction." ASME Journal of Heat Transfer 125(5): 896-903.
- Narumanchi, S. V. J., J. Y. Murthy, et al. (2004). "Comparison of Different Phonon Transport Models for Predicting Heat Conduction in Silicon-on-Insulator Transistors." ASME Journal of Heat Transfer(in review).
- Narumanchi, S. V. J., J. Y. Murthy, et al. (2004). "Submicron Heat Transport Model in Silicon Accounting for Phonon Dispersion and Polarization." ASME J. Heat Transfer, 126(6): 946-955.
- Pop, E., S. Sinha, et al. (2002). Monte Carlo Modeling of Heat Generation in Electronic Nanostructures. International Mechanical Engineering Conference and Exposition, New Orleans, Louisiana.
- Schelling, P. K., S. R. Phillpot, et al. (2002). "Comparison of Atomic-Level Simulation Methods for Computing Thermal Conductivity." Physical Review B 65: 144306(1)-144306(12).
- Sinha, S., P. K. Schelling, et al. (2003). Atomistic Simulations of Non-equilibrium Phonons in Nanotransistors. SRC-TECHCON, Dallas, TX.
- Sverdrup, P. G., Y. S. Ju, et al. (2001). "Sub-Continuum Simulations of Heat Conduction in Silicon-on-Insulator Transistors." Journal of Heat Transfer 123(1): 130-137.

- Tamura, S.-I., Y. Tanaka, et al. (1999). "Phonon group velocity and thermal conduction in superlattices." Physical Review B **60**(4): 2627-2630.
- Volz, S., J. B. Saulnier, et al. (2000). "Computation of Thermal Conductivity of Si/Ge Superlattice by Molecular Dynamics Technique." Microelectronics Journal **31**(9-10): 815-819.
- Volz, S. G. and G. Chen (1999). "Lattice Dynamic Simulation of Silicon Thermal Conductivity." Physica B **263-264**: 709-712.
- Volz, S. G. and G. Chen (1999). "Molecular Dynamics Simulation of Thermal Conductivity of Silicon Nanowires." Applied Physics Letters **75**(14): 2056-2058.
- Volz, S. G. and G. Chen (2000). "Molecular-Dynamics Simulation of Thermal Conductivity of Silicon Crystals." Physical Review B **61**(4): 2651-2656.
- Ziman, J. (1960). Electrons and Phonons; The Theory of Transport Phenomena in Solids, Oxford, Clarendon Press.

Chapter 2:

Background and Computational Challenges

This chapter begins by presenting a brief review of the thermal energy transport in crystalline silicon, which provides the justification for using the molecular dynamics technique for the calculation of thermal properties in silicon. A review of the available approaches for bulk silicon thermal conductivity calculations, using equilibrium molecular dynamics and the Green-Kubo formalism, is presented in the second section. The third section, on computational challenges, describes the motivation for a parallel code implementation, its validation and the code's flowchart.

2.1 Thermal Transport in Silicon

Thermal energy transport in solids is done mainly by electrons and phonons, i.e. the quanta of lattice vibrations (Tien, Majumdar et al. 1998). The electronic contribution to the thermal energy transport in silicon and other semiconductors with covalent bonds is negligible due to the lack of valence electrons. In fact, the electronic contribution to the bulk silicon thermal conductivity has been experimentally determined to be approximately 0.65 W/mK at 1000 K (about 2% of its total value at this temperature), and negligible below 1000 K (Glassbrenner and Slack 1964). Hence, accurate prediction of thermal properties in silicon at sub-continuum scales requires only an accurate description of the phonon's behavior or of the atomic trajectories in the lattice.

2.2 Computational Procedure

The following sections present an overview of the molecular dynamics technique and the equations for the prediction of bulk thermal conductivity using the microcanonical ensemble, i.e. a constant number of particles, volume and total energy.

2.2.1 The molecular dynamics technique

The molecular dynamics (MD) technique is a deterministic, non-quantum computational method, used to predict the trajectory of an ensemble of atoms by solving Newton's second law of motion for each atom:

$$m_i \frac{d^2 \vec{x}_i}{dt^2} = \vec{F}_i = -\vec{\nabla}_i U \quad (2.2.1)$$

where m_i and \vec{x}_i are the atom's mass and location, respectively. The total force \vec{F}_i on atom i is due to its interaction with all the other atoms in the ensemble, and is calculated by taking the gradient of the potential energy U , as indicated in the right hand side of Eq. (2.2.1).

2.2.2 Interatomic potentials for silicon

As seen from Eq. (2.2.1), a molecular dynamics simulation only requires the mass, the initial location and velocities of the atoms in the ensemble, and an accurate interatomic potential. Among the interatomic potentials available for silicon, the Stillinger-Weber (SW) potential (Stillinger and Weber 1985) accurately predicts temperature related properties, such as the melting point (Stillinger and Weber 1985; Broughton and Li 1987) and the thermal expansion of silicon (Cook and Clancy 1993), as well as the elastic properties (Karimi, Yates et al. 1998) and the yield strength (Kallman, Hoover et al. 1993). The SW potential models the interaction between atom i and its neighbors by independently adding the contributions of the two-body and three-body terms, given by:

$$U_i = \sum_{j \neq i} \phi_2(\vec{x}_i, \vec{x}_j) + \sum_{j \neq i} \sum_{k \neq j} \phi_3(\vec{x}_i, \vec{x}_j, \vec{x}_k) \quad (2.2.2)$$

where ϕ_2 is the two-body potential, which regulates the distance between two silicon atoms by means of a short-distance repulsive term and a long-distance attractive term; and ϕ_3 is the three-body potential, which is required to stabilize the diamond like structure of crystalline silicon by controlling the angle formed by the vectors joining the atom located at the center of the tetrahedron and the atoms located at the corners, see insert in Fig. 2.2.1. The mathematical expression of the two and three-body terms of the SW potential are shown in Eqs. (2.2.3) and (2.2.4), respectively:

$$\phi_2(r_{ij}) = \begin{cases} \epsilon \cdot A \left[B \left(\frac{\sigma}{r_{ij}} \right)^p - \left(\frac{\sigma}{r_{ij}} \right)^q \right] \cdot e^{\frac{\sigma}{r_{ij} - \sigma r_c}} & r_{ij} < \sigma r_c \\ 0 & r_{ij} \geq \sigma r_c \end{cases} \quad (2.2.3)$$

$$\phi_3(r_{ij}, r_{ik}) = \begin{cases} \epsilon \cdot \lambda \cdot e^{\left[\frac{\gamma \sigma}{(r_{ij} - \sigma r_c)} + \frac{\gamma \sigma}{(r_{ik} - \sigma r_c)} \right]} \cdot \left(\cos(\theta_{jik}) + \frac{1}{3} \right)^2 & r_{ij}, r_{ik} < \sigma r_c \\ 0 & \text{otherwise} \end{cases} \quad (2.2.4)$$

where: ϵ is the interatomic potential depth in Joules, σ is the characteristic distance in pair potential in nm, r_c is the dimensionless cutoff radius, and r_{ij} and r_{ik} are the magnitude of the distance between atoms i and j and atoms i and k , respectively. For the two-body potential, Eq. (2.2.3), A is the well-depth factor, B is the short-distance repulsive term factor, p is the short-distance repulsive term power, and q is the long-distance attractive term power. For the three-body potential, Eq. (2.2.4), λ is the well-depth factor, γ is the cutoff factor and θ_{jik} is the angle between vectors \vec{r}_{ij} and \vec{r}_{ik} in radians.

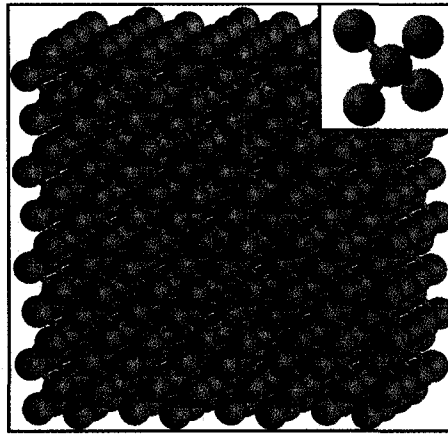


Figure 2.2.1. Silicon lattice (4x4x4 lattice constants) depicting the atoms as spheres and the atomic bonds as lines. The inset shows a silicon molecule.

The values of the potential's constants reported by Stillinger and Weber (Stillinger and Weber 1985), and reproduced in Table 2.2.1, give the most stable silicon structure at low pressure, as well as accurately predict the melting point and the liquid structure of silicon using MD simulations (Stillinger and Weber 1985). The lattice constant for silicon at 300 K and the atomic mass of ^{28}Si are also reported in Table 2.2.1.

Table 2.2.1. Stillinger-Weber potential's constants for silicon.

Parameter	Value
A	7.049556277
B	0.602224558
p	4.0
q	0.0
r_c	1.80
λ	21.0
γ	1.20
ϵ	3.472×10^{-19} J
σ	0.20951 nm
a	0.543 nm
$m (\text{Si}^{28})$	4.66×10^{-26} kg

2.2.3 Heat current definition

The heat current is given by (Hardy 1963; McQuarrie 1976; Allen and Tildesley 1987),

$$\vec{J} = \frac{\partial}{\partial t} \left(\sum_i \vec{x}_i \cdot E_i \right) \quad (2.2.5)$$

where \vec{x}_i is the atomic position of atom i , and the total energy, E_i , stored in atom i is the sum of the kinetic and potential energies,

$$E_i = \frac{1}{2} m_i \vec{v}_i \cdot \vec{v}_i + \frac{1}{2} \sum_{j \neq i} \phi_2 + \frac{1}{6} \sum_{j \neq i} \sum_{k \neq i, j} \phi_3 \quad (2.2.6)$$

where the first term on the right hand side is the kinetic energy of atom i , the second and third terms are the contributions from the two- and three-body Stillinger-Weber interatomic potential (Stillinger and Weber 1985) given by Eqs. (2.2.3) and (2.2.4), respectively. After differentiating Eq. (7) with respect to time and recognizing that the gradient of the potential energy with respect to the location is the negative of the force on the atoms, the expression for the heat current becomes

$$\vec{J} = \sum_i E_i \vec{v}_i + \frac{1}{2} \sum_i \sum_{j > i} \vec{r}_{ij} [\vec{F}_{ij} \cdot (\vec{v}_i + \vec{v}_j)] + \frac{1}{6} \sum_i \sum_{j \neq i} \sum_{k \neq i, j} (\vec{r}_{ij} + \vec{r}_{ik}) [\vec{F}_{ijk} \cdot \vec{v}_i] \quad (2.2.7)$$

where the first term represents the thermal energy transported by atomic convection, relevant for liquids and gases (Volz and Chen 2000). The second and third terms in Eq. (2.2.7) are the thermal energy transferred by conduction through interatomic interactions, which include the two-body interactions (second term) and three-body interactions (third term). We have numerically verified that the convective term is negligible with respect to the second and third terms in condensed matter by calculating their root-mean-squares (RMS) over 10^6 steps of MD (Gomes, Madrid et al. 2003). The RMS of the convective term is 0.69% of the RMS for the second term and 1.72% of the RMS for the third term at 1000 K. Since the present work is focused on the condensed phase, and the numerical simulations have confirmed the small contribution of the convective term to the heat current, it was not included in the calculation of the heat current. Figure 2.2.2 shows the time evolution of the heat current's convective and conductive terms, averaged over all the directions. The time averages of the different heat current contributors are zero, since there is no net heat flow in the ensemble.

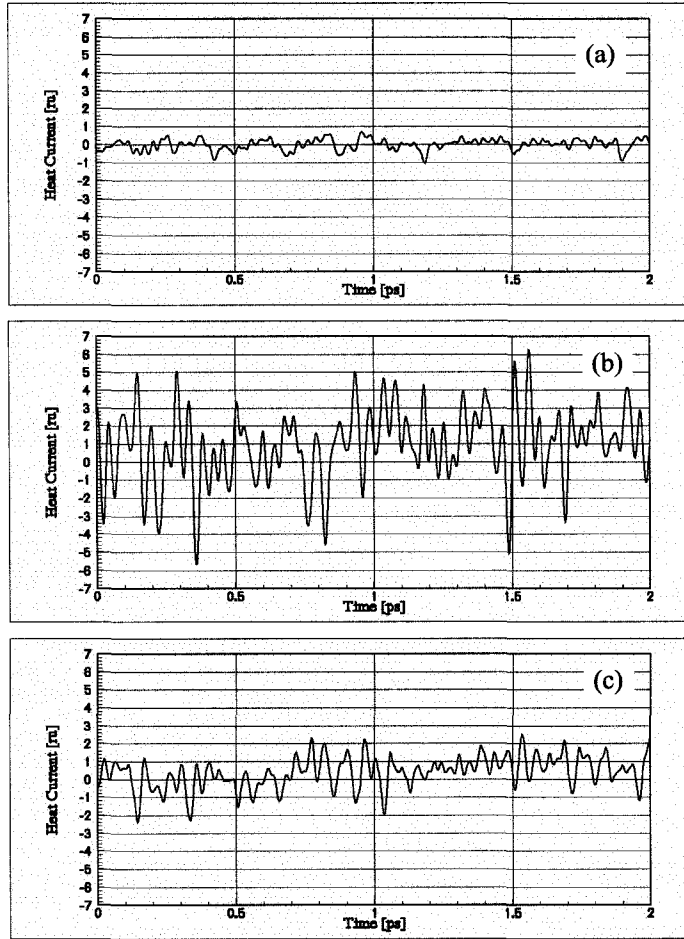


Figure 2.2.2. Time evolution of (a) the heat current's convective term (first term in Eq. (2.2.7)) and the conductive terms: (b) two body and (c) three-body contributions, (second and third terms of Eq. (2.2.7) respectively). The results are for 5x5x5 silicon cells at 1000 K. The figure shows that for condensed matter the convective term is negligible with respect to the conductive ones.

2.2.4 Green-Kubo relation for determining thermal conductivity

The Green-Kubo expression (Kubo 1966) for the thermal conductivity of isotropic materials is given by:

$$k = \frac{1}{3Vk_B T^2} \int_0^\infty \langle \vec{J}(\tau) \cdot \vec{J}(0) \rangle dt \quad (2.2.8)$$

where k is the thermal conductivity in W/mK, V is the ensemble volume in m^3 , T is the temperature in K, k_B is the Boltzmann's constant, J is the heat current and the integrand is the heat-current-autocorrelation-function's (HCACF) ensemble average. The ensemble average of the HCAF can be replaced by its time average in accordance with the ergodic hypothesis (Frenkel and Smit 2001). Using the trapezoidal rule to integrate Eq. (2.2.8) over a finite number of constant size time steps, it becomes:

$$k_{MD}(\tau_M) = \frac{\Delta t}{3Vk_B T_{MD}^2} \sum_{m=1}^M (N_s - m)^{-1} \sum_{n=1}^{N_s - m} \vec{J}(m+n) \cdot \vec{J}(n) \quad (2.2.9)$$

where k_{MD} is the molecular dynamics determined thermal conductivity in W/mK, T_{MD} is the temperature of the molecular dynamics simulation in K, Δt is the simulation time step in s, N_s is the total number of HCAF samples, M is the number of time steps required for the HCAF to decay to zero and $N_s - m$ is the number of HCAF averages at time $\Delta t \cdot m$. The integration time, τ_M , is the upper limit of the integral in Eq. (2.2.9) $\tau_M = \Delta t \cdot M$, in s. The main drawback of using equilibrium molecular dynamics for the calculation of the thermal conductivity in silicon is that the heat current autocorrelation function decays slowly to zero, requiring long MD simulations to compute the thermal conductivity.

Figure 2.2.3 (a) shows the time evolution of the heat current autocorrelation function for isotopically pure bulk silicon for a 5x5x5 lattice constants simulation at $T_{MD} = 300$ K, the heat current autocorrelation function appears to have decayed to zero after 200 ps. Figure 2.2.3 (b) shows the variation of the molecular dynamics determined thermal conductivity, Eq. (2.2.9), as the upper limit of the integral is increased. The plateau after 200 ps in the molecular dynamics determined thermal conductivity corroborates that the heat current autocorrelation function has, in fact, decayed to zero. Figure 2.2.3 (b) also shows the quantum corrected thermal conductivity for this simulation, see Section 2.2.5.

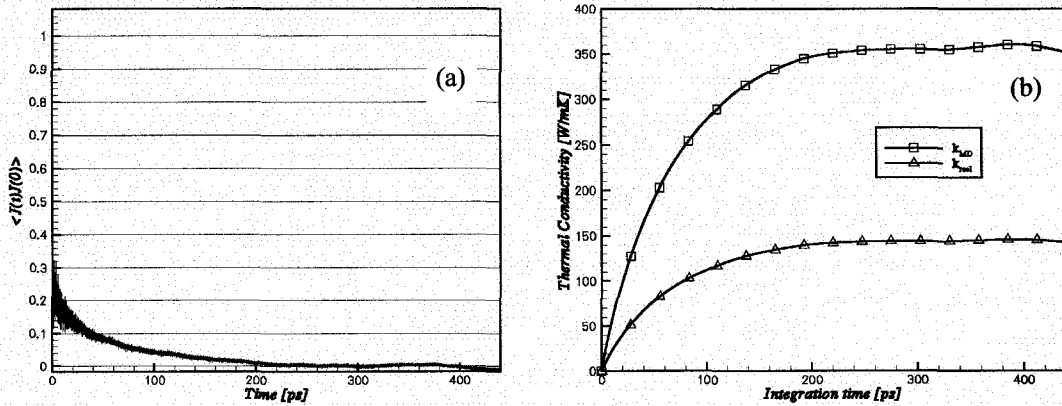


Figure 2.2.3. (a) Time evolution of the heat current autocorrelation function, (b) thermal conductivity variation with the integration time. Both for a 5x5x5 silicon cells at $T = 248$ K.

2.2.5 Quantum corrections

The temperature (T_{MD}) of the molecular dynamics simulation is set at the beginning of the simulation by scaling the atomic velocities according to the classical statistical mechanics equipartition theorem (Reif 1965):

$$\frac{3}{2} N k_B T_{MD} = \frac{1}{2} \sum_{i=1}^N m_i \vec{v}_i \cdot \vec{v}_i \quad (2.2.10)$$

where N is the number of atoms in the ensemble and \vec{v}_i is the velocity of atom i .

Since molecular dynamics is a classical method, quantum corrections must be applied to the MD-predicted thermal conductivity and to the temperature given by Eq. (2.2.10) at temperatures below the Debye temperature (θ_D), where, for a solid, quantum effects start to become important. Quantum corrections can be estimated by equating the ensemble's total energy to the phonons' total energy (Lee, Biswas et al. 1991; Volz and Chen 1999; Volz, Saulnier et al. 2000) as:

$$\frac{3k_B T_{MD}}{V} = e_{LA}(T) + 2e_{TA}(T) + e_{LO}(T) + 2e_{TO}(T) \quad (2.2.11)$$

where, e is the phonon energy per unit of volume at temperature T , J/m^3 :

$$e_i(T) = \frac{1}{2\pi^2} \int_{\omega_{min}}^{\omega_{max}} \left(f_{\omega_i}^0 + \frac{1}{2} \right) \hbar \omega_i \frac{(q(\omega_i))^2}{v(\omega_i)} d\omega_i \quad (2.2.12)$$

where \hbar is Plank's constant divided by 2π , $v(\omega)$ is the phonon's propagation velocity at frequency ω , $q(\omega)$ is the wave number at frequency ω , $f_{\omega_i}^0$, Eq. (2.2.13), is the equilibrium phonon distribution function, given by the Bose-Einstein distribution function, T_{MD} is the temperature of the molecular dynamics simulation, and T is the temperature and the integration limits ω_{min} and ω_{max} are given by the dispersion relation for the different branches and polarizations (longitudinal acoustic LA, transverse acoustic TA, longitudinal optical LO and transverse optical TO). Equation (2.2.12) is solved analytically assuming that the medium is isotropic; the first Brillouin zone is approximated by a sphere and the number of atoms is large enough so that the dispersion relation can be treated as a continuum curve. The dispersion relation for silicon is calculated from the Stillinger Weber potential (Porter, Justo et al. 1997):

$$f_{\omega_i}^0 = \frac{1}{e^{\frac{\hbar \omega_i}{k_B T}} - 1} \quad (2.2.13)$$

The quantum energy of a system includes the zero-point energy, the factor $\frac{1}{2} \hbar \omega$ in Eq. (2.2.12). Controversy surrounds the correction factors that should be used to account for quantum effects in a molecular dynamics simulation; in particular, whether the zero-point energy should or should not be

included in Eq. (2.2.12). In this study we have included this factor, because our objective is to correct the classical energy (left hand side of Eq. (2.2.11)), and obtain the quantum one (right hand side of Eq. (2.2.11)). Quantum-correction factors for the thermal conductivity and temperature can be estimated as (Volz, Saulnier et al. 2000):

$$\frac{k}{k_{MD}} = \frac{\partial T_{MD}}{\partial T} \quad (2.2.14)$$

where k and T are the corrected thermal conductivity and temperature, respectively, and k_{MD} and T_{MD} are the molecular dynamics predicted thermal conductivity and temperature of the simulation, respectively. Since the derivative with respect to the temperature of the energy is the specific heat, Eqs. (2.2.11) and (2.2.14) become:

$$\frac{k}{k_{MD}} = \frac{\partial T_{MD}}{\partial T} = \frac{C(T)}{3Nk_B} \quad (2.2.15)$$

where C is the specific heat, $\text{W/m}^3\text{K}$. Therefore, the correction factor for the thermal conductivity can be taken from the reported experimental specific heat for silicon. The correction factors for the temperature are obtained by integrating Eq. (2.2.14).

$$T_{MD}(T) = \frac{V}{3k_b} \int_0^T C_v(T) dT + T_{MD}^* \quad (2.2.16)$$

where T_{MD}^* , the integration constant, is adjusted such that T is equal to T_{MD} for temperatures larger or equal to a given T_{MD} ; this temperature is $T = T_{MD} = \theta_D$ throughout this work. The Debye's temperature depends on the experimental parameters used to compute it. Figures 2.2.4 (a) and (b) show the variation of the quantum corrections with the Debye temperature, for θ_D between 600 and 700 K. Figures 2.2.4 show that the variation of the quantum corrections with θ_D are small for high temperatures of the molecular dynamics simulation and increase for low temperatures of the molecular dynamics simulation. For instance, the thermal conductivity quantum correction varies from 0.66 to 0.72 for θ_D ranging from 600 to 700 K, at the lowest temperature of the molecular dynamics simulation used in this work, $T_{MD} = 300$ K, while the temperature varies from 229 to 263 K. These variations are acceptable from an engineering point of view and the quantum corrections shown in Fig. 2.2.5 for $\theta_D = 645$ K is used throughout this work.

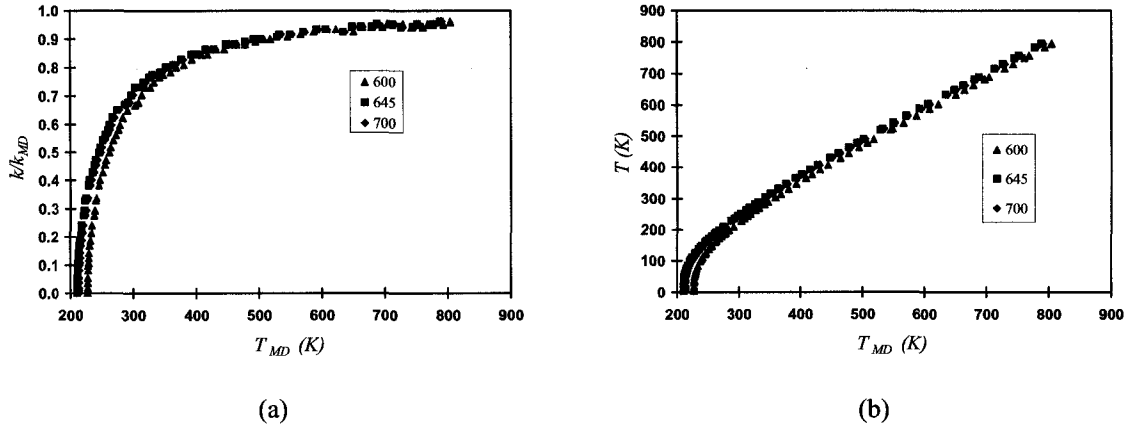


Figure 2.2.4. Variation of the quantum corrections for (a) the thermal conductivity and (b) the temperature, for Debye temperatures ranging from 600 to 700 K.

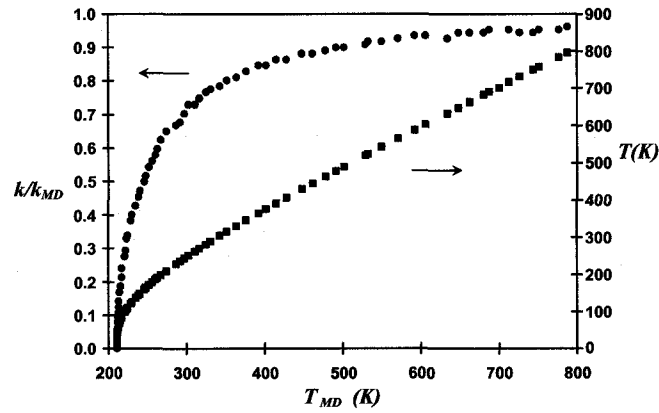


Figure 2.2.5. Quantum corrected temperature (right axis), and ratio of quantum corrected to molecular dynamics predicted thermal conductivity (k/k_{MD}) (left axis), as a function of the temperature of the MD simulations for silicon.

Table 2.2.2 lists the temperature of the molecular dynamics simulation (T_{MD}) and the correction factors for the temperature and the thermal conductivity obtained from the experimentally determined specific heat (T_c and k_c), and analytically (T_a and k_a). Notice that for $T > \theta_D$, (with $\theta_D = 645$ K for silicon (Ashcroft and Mermin 1976)), where the system behaves classically, these corrections are negligible. All molecular dynamics predicted thermal conductivities reported in this paper have been corrected according to the experimental specific heat correction curves shown in Fig. 2.2.5.

Table 2.2.2. Quantum correction factors determined from the experimental specific heat (T_c and k_c) and analytically (T_a and k_a).

T_{MD}	T_c	T_a	k_c/k_{MD}	k_a/k_{MD}
300	248	140	0.72	0.40
400	375	305	0.85	0.75
500	480	430	0.91	0.85
700	700	650	0.94	0.93
1000	1000	970	0.99	0.97

2.3 Computational Challenges

To obtain the thermal conductivity from equilibrium molecular dynamics, the heat current autocorrelation function needs to be averaged over millions of MD steps (Schelling, Phillpot et al. 2002), parameter N_s in Eq. (3.2.6). Predicting the quantities needed for the calculation of the heat current autocorrelation function (the atomic locations, velocities and forces) over millions of MD steps may take several weeks, even months, depending on the number of atoms in the simulation. Table 2.3.1 lists the computational time required per step of simulation and for 6 million steps of molecular dynamics for systems of different sizes. Extrapolating from Table 2.3.1, we expect that the simulation of a 100 nm thick silicon thin-film with $8 \times 8 \times 185$ lattice constants and a total of 94,848 atoms will take about 819 days (2.24 years) in a single 1.4 GHz processor computer. To address this problem and to be able to handle even larger systems in a reasonable amount of time, a parallel molecular dynamics code (PMD) was implemented.

Table 2.3.1. Time benchmarks for the serial code (run on a 1.4GHz processor).

<i>Number of lattice constants</i>	<i>Number of atoms</i>	<i>Time per step (s)</i>	<i>6×10^6 MD steps (days)</i>
4x4x4	512	0.0362	2.5
5x5x5	1,000	0.0712	4.9
10x10x10	8,000	0.5890	41
20x20x20	64,000	6.8090	473

2.3.1 The parallel molecular dynamics code

Three main criteria were considered during the developmental phase of the parallel version of the code: (1) portability, (2) good scaling with the number of atoms and (3) good scaling with the number of processors. The first criterion was achieved by using the standard MPI (Gropp, Lusk et al. 1996) library for message passing. The code was run on two massively parallel systems Jaromir (CRAY T3E) and Lemieux (HP Alphaserver) at the Pittsburgh Super Computer Center.

The second criterion was accomplished with the use of the neighbor list scheme. The neighbor list consists of storing the list of atoms that are located within a certain distance from the atom in consideration.

The force on the atom is calculated assuming that the atom interacts only with those atoms in the neighbor list. This strategy keeps the CPU time proportional to the number of atoms. Since we are focused on the condensed phase and atomic diffusion is not present, the neighbor list is calculated only at the beginning of the simulation for bulk silicon or every 25 steps during the equilibrium part of the simulation for thin-films, which is about 50,000 MD steps. Figure 2.3.1 shows the CPU time per step as a function of the number of atoms for different numbers of processors.

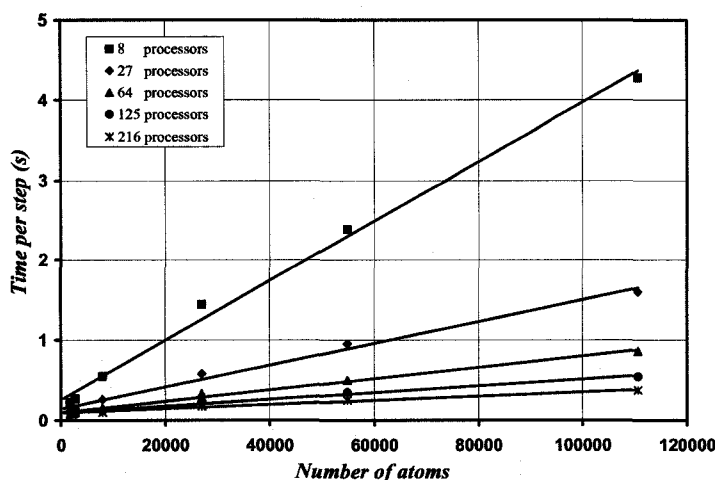


Figure 2.3.1. CPU time per step of molecular dynamics as a function of the number of atoms for different numbers of 450MHz processors, showing a linear dependence with the number of atoms.

The third criterion was met with the use of the ghost cell strategy, also known as a buffer cell strategy (Stadler, Mikulla et al. 1997). The ghost cell strategy consists of dividing the simulation domain into several smaller subdomains, and assigning each subdomain to a processor. Then, each processor labels the atoms according to whether they are located inside its subdomain (internal atoms) or in the ghost cell (ghost atoms). The ghost cell is defined as the space between the subdomain's boundary and twice the cutoff radius, $2\sigma r_c$. The criterion of twice the cutoff radius is required to properly include the atoms that interact with the internal atoms via the three-body potential. Figure 2.3.2 (b) shows that atoms j (internal) and k (ghost) interact with atom i , via the three-body term involving angle θ_{jik} . However, the interaction between atoms k and n , both ghosts, and atom i via the three-body term involving angle θ_{ikn} would have been missed if the criterion $2\sigma r_c$ had not been used. The atoms that are located more than two cutoff radii from the subdomain's boundary are ignored by the processor because they do not interact with the internal atoms.

Internal and ghost atoms are treated differently, each processor has all the information related to its internal atoms, but it only has the location (needed to calculate the force) and the velocity (for the heat current calculation) of the ghost atoms. This strategy reduces the amount of memory required per processor. Moreover, communication between processors is limited to exchanging the information about the ghost atoms, which reduces the amount of information transferred over the network.

The simulation domain is divided using a Cartesian grid, guaranteeing that each processor interchanges information with a maximum of 26 processors, independent of the total number of processors used. Figure 2.3.2(a) shows a two-dimensional representation of the ghost cell approach, where the simulation domain is divided among nine processors. In this example, each processor interchanges information with a maximum of eight processors.

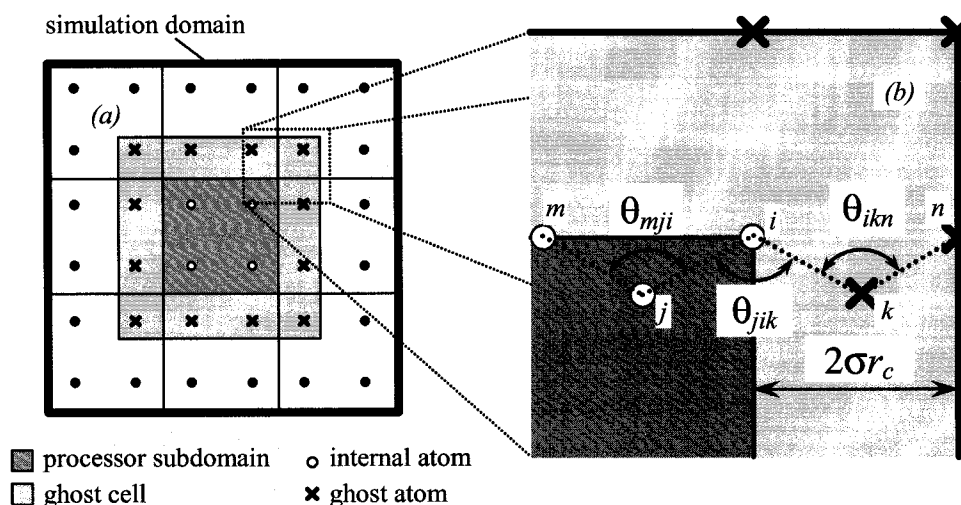


Figure 2.3.2. Two-dimensional example illustrating the ghost cell strategy used for code parallelization.

Figure 2.3.3 shows the time per step as a function of the number of processors for different numbers of atoms. It can be seen that the computational time per step decreases with the number of processors, up to the number of processors tested, specifically 216.

2.3.2 Parallel molecular dynamics code validation and flowchart

The parallelized integration algorithm, the force calculation function and the neighbor list determination, all initially coded in serial, were validated by comparing the trajectories of a set of atoms to the trajectories predicted with the serial version of the code, for the same initial and boundary conditions. The comparison was made after several thousand MD steps, obtaining identical results. The parallelized thermal conductivity calculation was validated by computing the bulk silicon thermal conductivity for temperatures ranging from 300 K to 1100 K for different domain sizes; see Section 3.2 for details. A basic flowchart of the parallel code is shown in Fig. 2.3.4.

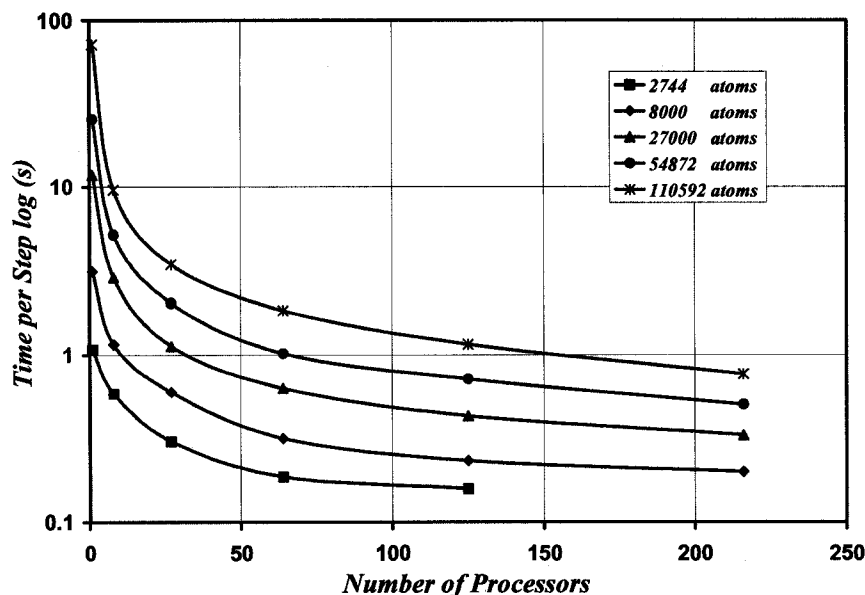


Figure 2.3.3. CPU time per step of molecular dynamics versus number of processors, for number of atoms ranging from 2,744 to 110,592. Simulations were performed on the CRAY T3E at the Pittsburgh Supercomputing Center.

2.4 Conclusions

In this chapter we describe the equilibrium molecular dynamics with the Green-Kubo formalism to predict the lattice contribution to the bulk thermal conductivity. Previously, this formalism has been applied to study the thermal conductivity of bulk materials (Volz and Chen 1999; Schelling, Phillpot et al. 2002). For the first time, we will apply the Green-Kubo formalism to determine the thermal conductivity of thin film silicon.

Since molecular dynamics is a classical method, it does not account for quantum effects, which are important at temperatures below the Debye temperature. In this chapter we describe previously proposed quantum correction factors (Volz and Chen 2000), which are important at temperatures below the Debye temperature. The total energy per unit of volume of the classical system is set equal to the energy per unit of volume of the phonon system. Instead of using mathematical simplifications to predict the phonon energy and its derivative, we have taken advantage of the fact that the derivative of the phonon energy is the specific heat. We have used the experimental silicon specific heat per unit of volume to predict the thermal conductivity quantum corrections. The integral of the specific heat gives the quantum corrections for the temperature. We believe this approach is more accurate because it uses experimental data, avoiding several mathematical simplifications. We show that, at $T < \theta_D$ the quantum correction factors depend on the method used to calculate them.

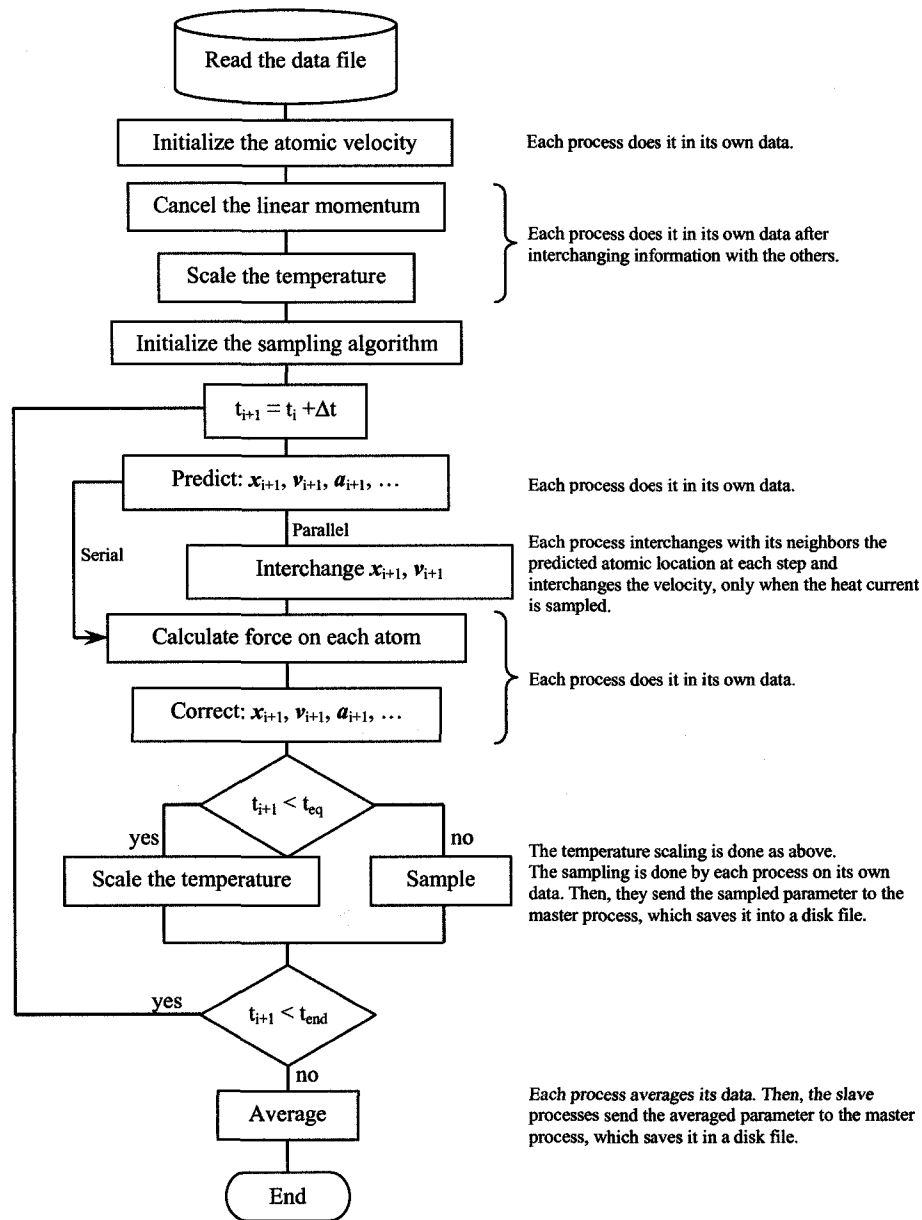


Figure 2.3.4. Flowchart of the serial and parallel molecular dynamics code.

Predicting the thermal conductivity of thin films (whose surfaces are of physical importance) requires the inclusion of the actual surface in the atomistic simulation. This requires the inclusion of a large number of atoms in the simulation. Hence the need of a computer code capable of managing large atomic systems within reasonable amount of time. We developed a molecular dynamics code that incorporates the Stillinger-Weber potential and runs in serial and massively parallel computers. The serial code was validated by comparing the location of a set of atoms after 100,000 molecular dynamics steps to their location predicted using a serial shareware code known as XMD (<http://xmd.sourceforge.net/about.html>) for the same initial conditions and integration algorithm. The atomic location was identical up to the 8th significant figure in reduced units. Then the serial code was used to validate the parallel code by comparing

the atomic locations of periodic and semi-periodic systems after 10^6 molecular dynamics steps. The parallel version of the code has been tested in two massively parallel systems Jaromir (CRAY T3E) and Lemieux (HP Alphaserver) at the Pittsburgh Supercomputing Center (PSC). Although additional improvements in the performance of the program are desired (described in the Future Work section), it ran in both platforms without changes.

2.5 References

- Allen, M. P. and D. J. Tildesley (1987). Computer Simulation of Liquids. Oxford, UK, Clarendon Press.
- Ashcroft, N. W. and N. D. Mermin (1976). Solid State Physics. Saunders College Publishers.
- Broughton, J. Q. and X. P. Li (1987). "Phase Diagram of Silicon by Molecular Dynamics." Physical Review B **35**(17): 9120-9127.
- Cook, S. J. and P. Clancy (1993). "Comparison of Semi-Empirical Potential Functions for Silicon and Germanium." Physical Review B **47**(13): 7686-7699.
- Frenkel, D. and B. Smit (2001). Understanding Molecular Simulation from Algorithms to Applications. New York, Academic Press.
- Glassbrenner, C. J. and G. A. Slack (1964). "Thermal Conductivity of Silicon and Germanium from 3K to the Melting Point." Physical Review **134**(4A): A1058-A1068.
- Gomes, C., M. Madrid, et al. (2003). Parallel Molecular Dynamics Code Validation Through Bulk Silicon Thermal Conductivity Calculations. 2003 ASME International Mechanical Engineering Congress and Exposition, Washington DC, ASME.
- Gropp, W., E. Lusk, et al. (1996). Using MPI: Portable Parallel Programming with the Message-Passing Interface. Cambridge, The MIT Press.
- Hardy, R. J. (1963). "Energy-Flux Operator for a Lattice." Physical Review **132**(1): 168-177.
- Kallman, J. S., W. G. Hoover, et al. (1993). "Molecular Dynamics of Silicon Indentation." Physical Review B **47**(13): 7705-7709.
- Karimi, M., H. Yates, et al. (1998). "Elastic Constants of Silicon Using Monte Carlo Simulations." Physical Review B **58**(10): 6019-6025.
- Kubo, R. (1966). "The Fluctuation-Dissipation Theorem." Report of Progress in Physics **29**: 255-284.
- Lee, Y. H., R. Biswas, et al. (1991). "Molecular-Dynamics Simulation of Thermal Conductivity in Amorphous Silicon." Physical Review B **43**(8): 6573-6580.
- McQuarrie, D. A. (1976). Statistical Mechanics. New York, Harper Collins.
- Porter, L. J., J. F. Justo, et al. (1997). "The Importance of Gruneisen Parameters in Developing Interatomic Potentials." Journal of Applied Physics **82**: 5378-5381.
- Reif, F. (1965). Fundamentals of Statistical and Thermal Physics. New York, McGraw-Hill.
- Schelling, P. K., S. R. Phillpot, et al. (2002). "Comparison of Atomic-Level Simulation Methods for Computing Thermal Conductivity." Physical Review B **65**: 144306(1)-144306(12).
- Stadler, J., R. Mikulla, et al. (1997). "IMD: A Software Package for Molecular Dynamics Studies on Parallel Computer." International Journal of Modern Physics **8**(5): 1131-1140.
- Stillinger, F. H. and T. A. Weber (1985). "Computer Simulation of Local Order in Condensed Phases of Silicon." Physical Review B **31**(8): 5262-5271.
- Tien, C.-L., A. Majumdar, et al., Eds. (1998). Microscale Energy Transport. Series in Chemical and Mechanical Engineering. Washington DC, Taylor and Francis.
- Volz, S., J. B. Saulnier, et al. (2000). "Computation of Thermal Conductivity of Si/Ge Superlattice by Molecular Dynamics Technique." Microelectronics Journal **31**(9-10): 815-819.
- Volz, S. G. and G. Chen (1999). "Lattice Dynamic Simulation of Silicon Thermal Conductivity." Physica B **263-264**: 709-712.
- Volz, S. G. and G. Chen (2000). "Molecular-Dynamics Simulation of Thermal Conductivity of Silicon Crystals." Physical Review B **61**(4): 2651-2656.

Chapter 3:

Bulk Silicon Thermal Conductivity

This chapter presents the MD-predicted bulk silicon thermal conductivity. In Section 3.1, we determine the number of averages needed to compute the heat current autocorrelation function, and study the influence of the value of the lattice constant on the MD-predicted thermal conductivity with the Stillinger-Weber potential. We report the thermal conductivity of pure silicon (100% ^{28}Si) in Section 3.2, for temperatures ranging from 240 to 1000 K. In Section 3.3 we study the effect of using periodic boundary conditions on the predicted thermal conductivity. We calculate the Fourier spectra of the atomic velocities obtained during the MD trajectory, to show that the frequencies obey the restrictions imposed by the periodic boundary conditions. We analyze the effect of these boundary conditions on the predicted thermal conductivity by solving the Boltzmann transport equation. The findings are summarized in Section 3.4.

3.1 Determination of the Parameters Needed for the Molecular Dynamics Prediction of Silicon Thermal Conductivity

In this section, we estimate the number of samples (parameter N_s in Eq. (2.2.9)) required to predict bulk silicon thermal conductivity that is independent of the number of averages of the heat-current-autocorrelation-function. This study is required because there is no consensus in the existing literature (Porter, Li et al. 1997; Volz and Chen 2000; Schelling, Phillpot et al. 2002) about the number of samples required, and in order to determine the most accurate yet efficient value for N_s . Figure 3.1.1 shows the variation of the predicted bulk silicon thermal conductivity with the number of samples (N_s) used to average the heat current autocorrelation function, for a $10 \times 10 \times 10$ simulation domain at 500 K. The results show that the predicted thermal conductivity is strongly affected by the number of samples when less than one million samples are used. Then the predicted thermal conductivity reaches a maximum value, in this particular case, at approximately 1.5 million samples, to finally reach a plateau. Similar behaviors were found for other domain sizes and temperatures of the molecular dynamics simulation (T_{MD}). Since the variation, once the plateau is reached, is in the order of the statistical error (20%) a number of samples equal to 6 million is used.

Another issue concerning the numerical prediction of the bulk thermal conductivity is the value of the lattice constant to be used at each temperature. It has been previously shown that, for Lennard-Jones materials, the use of a lattice constant different than the equilibrium one at the corresponding temperature affects the MD-predicted thermal conductivity (McGaughey and Kaviani 2004). However, this information is not available for molecular dynamics simulations using the Stillinger-Weber potential. Therefore, we estimate the value of the Stillinger-Weber silicon lattice constant at different temperatures. Then, we study the influence of the lattice constant value on the predicted thermal conductivity by computing the thermal

conductivity using lattice constants that are larger or smaller than the equilibrium lattice constant. We perform several molecular dynamics simulations, each with a different value of the lattice constant, from which we evaluated the normal stress Eq. (3.1.1). The Stillinger-Weber equilibrium lattice constant is that for which the average normal stress is zero. The Stillinger-Weber silicon equilibrium lattice constant is 0.5434 and 0.5437 nm for temperatures of the molecular dynamics simulation (T_{MD}) of 300 and 1000 K, respectively. The simulation domain used consists of five lattice constants in each direction.

$$\sigma = \frac{1}{3V \cdot N_s} \sum_{j=1}^{N_s} \sum_{i=1}^{N_{atoms}} \bar{r}_i \cdot \bar{f}_i \quad (3.1.1)$$

where σ is the normal stress in Pa, V is the ensemble volume in m^3 , r_i is the coordinate of the atom in m, f_i is the force on atom i in N, N_{atoms} is the number of atoms in the assemble and N_s is the number of samples.

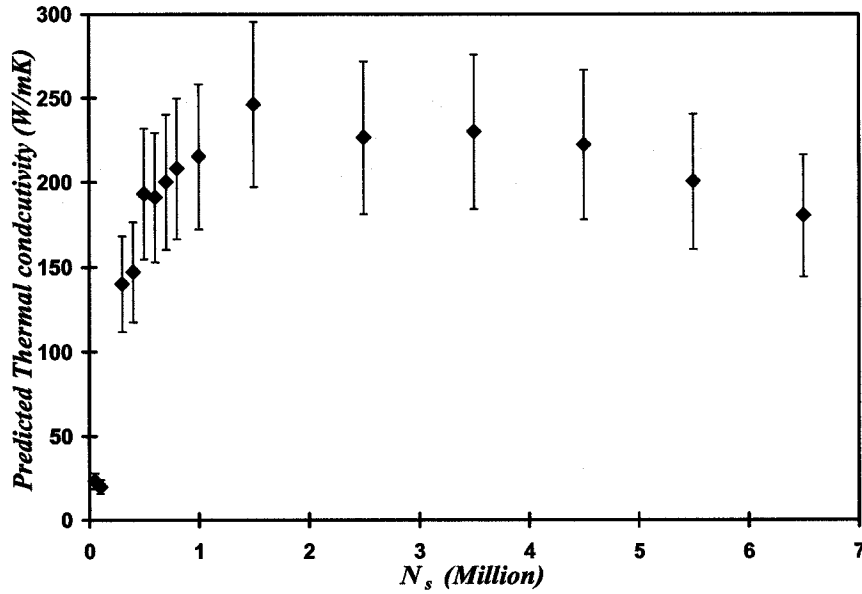


Figure 3.1.1. Variation of the predicted bulk silicon thermal conductivity with the number of samples used to average the heat current autocorrelation function.

Table 3.1.1 shows the predicted bulk silicon thermal conductivity and stress levels for different values of the lattice constant. The thermal conductivity and pressure are evaluated for two cases of the lattice constant 0.543 and 0.545 nm corresponding to compressing and stretching the crystallographic lattice, respectively. The results show that increasing the lattice constant reduces the MD-predicted bulk silicon thermal conductivities. However, since the reduction of the thermal conductivity is within the MD error (about 20%), more detailed studies at intermediate temperatures and lattice constants are needed. Therefore, the silicon experimental lattice constant of 0.543 nm (Madelung 1996) is used for bulk and thin film calculations.

Table 3.1.1. Predicted bulk silicon thermal conductivity for different values of the lattice parameter a_o .

Molecular dynamics temperature (K)	Stillinger-Weber equilibrium lattice constant (nm)	$a_o = 0.543$ nm		$a_o = 0.545$ nm	
		Thermal Conductivity (W/mK)	Stress (MPa)	Thermal Conductivity (W/mK)	Stress (MPa)
300	0.5434	297	-204	252	905
1000	0.5437	51	-407	48.56	687

3.2 Bulk Silicon Thermal Conductivity

The MD-predicted bulk silicon thermal conductivity is shown in Fig. 3.2.1 for simulation domains of 2x2x2, 3x3x3, 4x4x4, 5x5x5, 7x7x7 and 10x10x10 lattice constants, as a function of temperature. Both the temperature and the thermal conductivity reported were corrected for quantum effects using the experimental specific heat approach described in Section 2.2.5. The predicted thermal conductivity is compared to available experimental thermal conductivity data for single crystal natural silicon (92.23% ^{28}Si , 4.67% ^{29}Si and 3.10% ^{30}Si) (Abeles, Beers et al. 1962; Glassbrenner and Slack 1964; Ho, Powell et al. 1972). Comparing pure silicon thermal conductivity predictions to natural silicon experimental data is possible since recent publications (Kremer, Graf et al. 2004) show that the thermal conductivity of isotopically enriched silicon (99.982% ^{28}Si) is approximately 10% higher than the thermal conductivity of natural silicon (92.23% ^{28}Si , 4.67% ^{29}Si and 3.10% ^{30}Si) at 300 K, where the main scattering mechanism is phonon-phonon collision. Additionally, theoretical studies (Tien, Majumdar et al. 1998) suggest that at high temperatures ($T > \theta_D$) inelastic phonon scattering (Umklapp processes) are the dominant phonon scattering mechanism, independently of the presence of isotopes, and therefore, the magnitude of the thermal conductivity should be the same for natural and isotopically enriched silicon. Although the molecular dynamics predicted thermal conductivity is higher than the experimental data over the range of temperature studied, the predictions follow the trend reported for the experimental thermal conductivity data, that is, the thermal conductivity is inversely proportional to the temperature. The over-prediction of the bulk silicon thermal conductivity can be a consequence of the use of periodic boundary conditions in the three directions. When we simulate thin films, periodic boundary conditions are used only in the two directions parallel to the film surfaces. In this case, the in-plane thermal conductivities predicted for thick films (which approach bulk-like dimensions) are closer to the experimental values (See Section 4.4.2) than those predicted using periodic boundary conditions in the three directions.

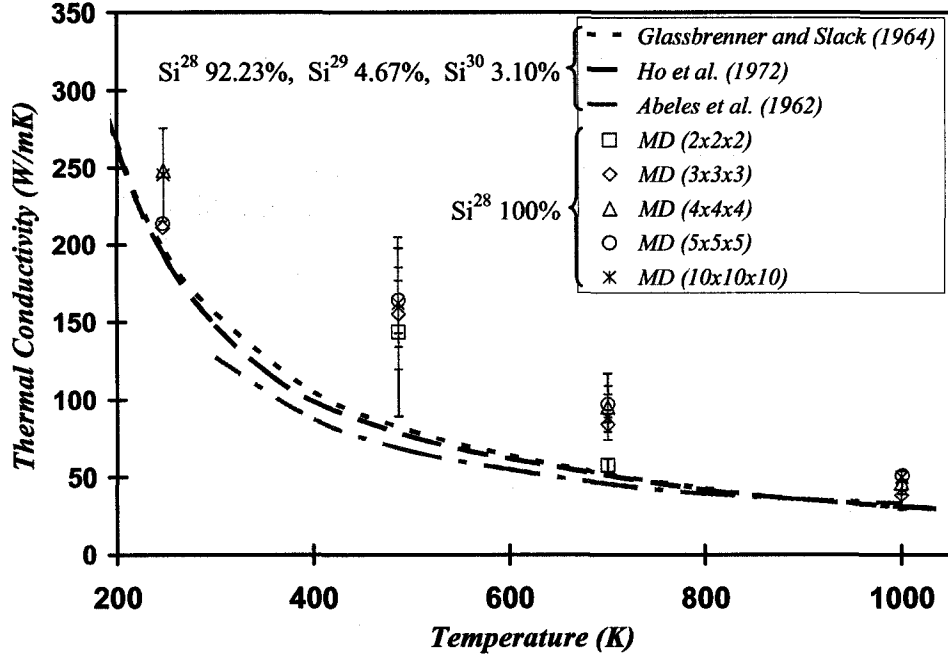


Figure 3.2.1. Bulk silicon thermal conductivity vs temperature for different simulation domain sizes and comparison with experimental results for natural silicon.

3.3 Bulk Silicon Simulation Size Artifacts

An infinite system such as bulk silicon is simulated by means of molecular dynamics by using a simulation domain consisting of a finite number of lattice constants, and applying periodic boundary conditions. The use of periodic boundary conditions restricts the allowed wave vectors k to those of the form

$$k = n_1/N b_1 + n_2/N b_2 + n_3/N b_3 \quad (3.3.1)$$

where $k = 2\pi/\lambda$, λ is the wavelength, n_1, n_2, n_3 are integers, $N \times N \times N$ are the dimensions of the simulation domain, and b_i are reciprocal lattice vectors (Ashcroft and Mermin 1976). In this section we study the effect that using a finite simulation domain and periodic boundary conditions has on the MD-predicted thermal conductivity.

Figure 3.3.1 shows the predicted thermal conductivity for pure bulk silicon, using simulation domains ranging from 2x2x2 to 10x10x10 lattice constants, for different temperatures. The results show that the predicted thermal conductivity is independent of the size of the simulation domain, for simulation domains larger than 3x3x3 lattice constants, for all the temperatures studied. These results indicate that simulations performed with a relatively small simulation domain can accurately predict the thermal conductivity of bulk silicon.

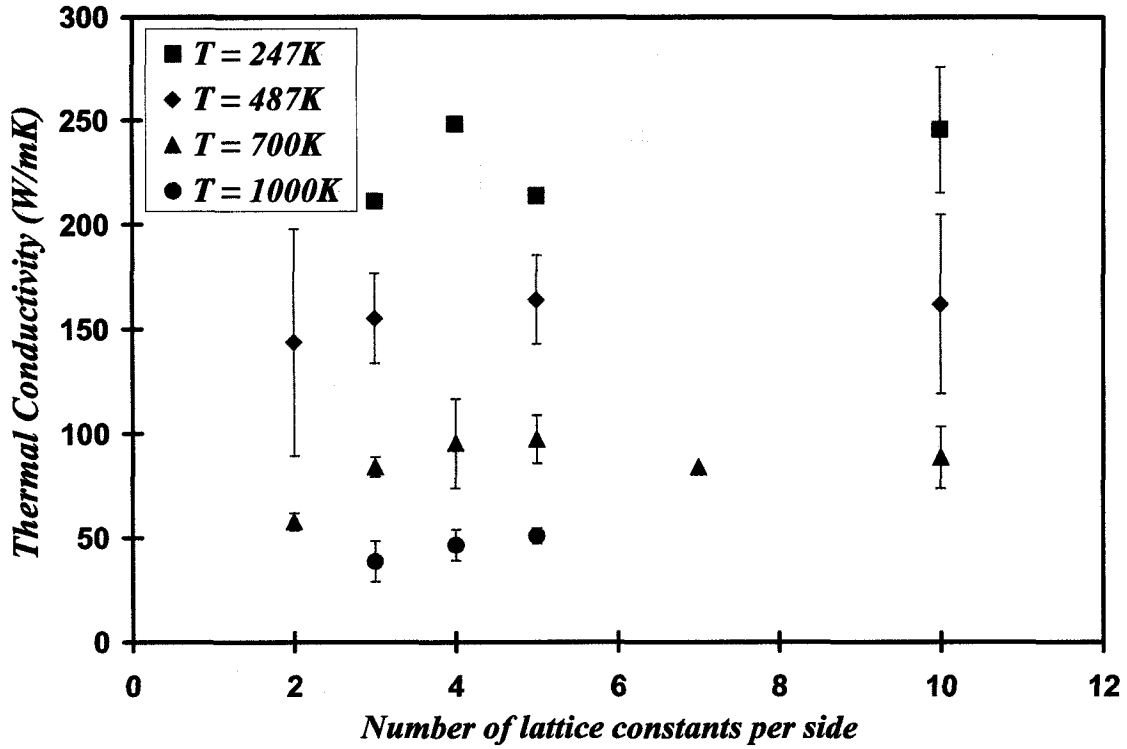


Figure 3.3.1. Variation of the pure silicon thermal conductivity with the simulation domain size for different temperatures.

Next, we analyze the Fourier spectra of the atomic velocities obtained during the molecular dynamics trajectories. This analysis is followed in Section 3.3.2 by a Boltzmann transport equation based explanation for the predicted independence of bulk silicon thermal conductivity on the molecular dynamics simulation domain size.

3.3.1 Phonon wavelength restrictions in molecular dynamics simulations with periodic boundary conditions.

Figure 3.3.2 shows the spectra of the phonons allowed by the molecular dynamics simulation for different domain sizes, when periodic boundary conditions are used (Gomes, Madrid et al. 2003). The spectra are obtained by taking the Fourier transform of the velocities of an atom during the molecular dynamics trajectory. Similar results are obtained when considering other atoms and directions, or with simulations that use different starting atomic velocities. The spectra are compared to the frequencies calculated using the Stillinger-Weber potential in the [100] crystallographic direction (Porter, Justo et al. 1997). These frequencies are calculated for the one-dimensional case of Eq. (3.3.1), that is, for phonons with wavelengths λ obeying the relation $\lambda=L/i$, where i is an integer ranging from one to the number of lattice constants in each direction, and L is the domain length. The symbols in the upper section of Fig. 3.3.2 (a)-(c) are placed at these frequencies for the two phonon branches and the two polarizations (longitudinal acoustic LA, transversal acoustic TA, longitudinal optical LO and transversal optical TO).

Since the molecular dynamics simulation includes not only the frequencies of the phonons traveling in the [100] crystallographic directions but also the frequencies of the phonons traveling in any of the allowed directions (Eq. 3.3.1), there are more frequency peaks in the Fourier spectra than calculated frequencies in Figs. 3.3.2 (a)-(c).

The frequency spectra are consistent with the observation that the MD simulations with periodic boundary conditions do not allow phonons with wavelengths larger than the dimensions of the computational domain (Lukes, Li et al. 2000; Volz and Chen 2000; Schelling, Phillpot et al. 2002). The smallest phonon frequency captured by the simulation coincides with the longitudinal acoustic frequency calculated from the dispersion relation (2.10 THz, 1.69 THz and 1.21 THz in Fig. 3.3.2 (a) through (c), respectively). These frequencies correspond to phonon wavelengths equal to the domain length ($\lambda=L$). The magnitude of the minimum allowed frequency decreases as the domain length increases and longer phonon wavelengths are allowed.

The spectra were computed up to 450 THz, and no frequencies were observed above approximately 18 THz. This is consistent with the dispersion relation calculated with the Stillinger-Weber potential, in which the maximum frequency, corresponding to the optical branch with $\lambda = \infty$, is approximately 17.8 THz (Porter, Justo et al. 1997).

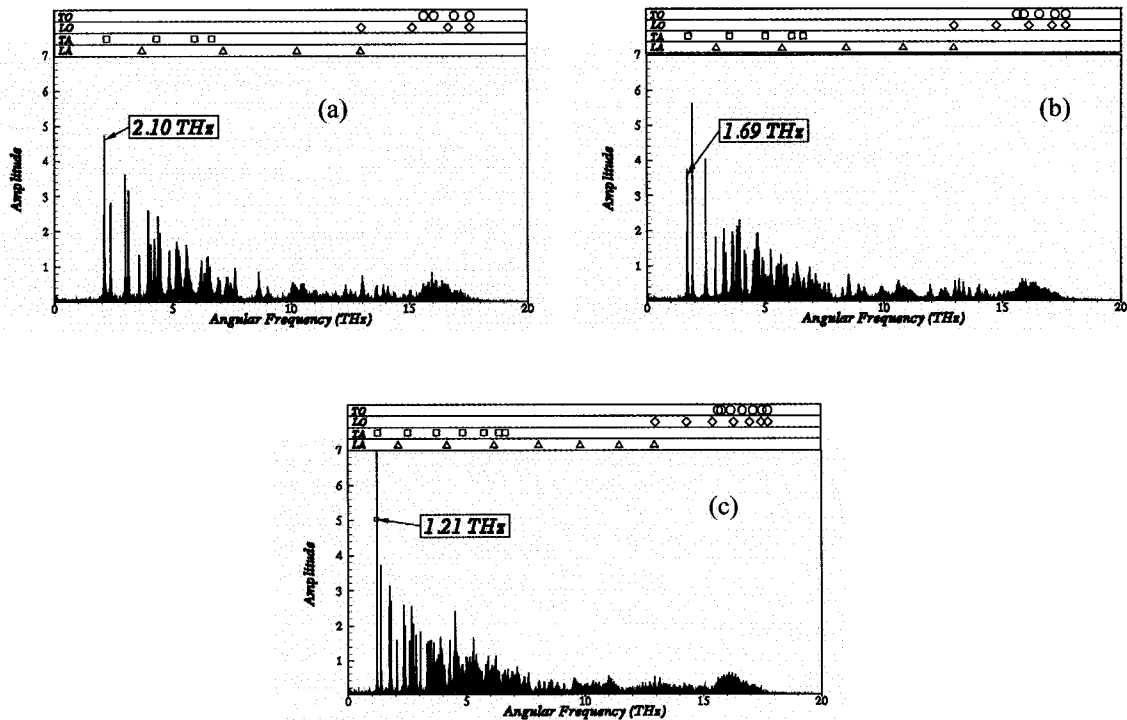


Figure 3.3.2. Frequency spectra of the atomic velocities at 1000 K for (a) 4x4x4, (b) 5x5x5 and (c) 7x7x7 lattice constant domains.

The Fourier spectra also show the frequency restrictions given by Eq. (3.3.1). The peaks shown in Figs. 3.3.2 (a)-(c) correspond to the allowed frequencies. The number of allowed frequencies, and therefore, the number of phonons, increases as the number of atoms (number of lattice constants used in the simulation) increases.

3.3.2 Effect of the phonon wavelength restrictions on the bulk thermal conductivity.

In this section we explain the influence of the phonon wavelength restrictions given by Eq. (3.3.1) on the predicted thermal conductivity by means of a Boltzmann transport equation (BTE)-based analytical model. Our goal is to show how the wavelength restrictions affect the phonon physics, and therefore the magnitude of the predicted thermal conductivity.

The analysis is done by incorporating the wavelength restrictions into the scattering term of the BTE, and then computing the bulk silicon thermal conductivity. The restrictions on the wavelengths imposed by Eq. (3.3.1) mean that no phonons are allowed with wavelengths larger than the simulation domain, the “wavelength cutoff” limitation. In addition, the allowed wavelengths are discrete, because they must satisfy Eq. (3.3.1) (where n_1, n_2, n_3 are integers ranging from one to the number of lattice constants in the respective direction). First, we consider only the effect of the wavelength cutoff on the bulk thermal conductivity, Case A. Next, we study the effect of both the wavelength cutoff and discreteness, Case B. The details of the mathematical formulation and equations are presented in Appendix A. The analysis incorporates phonon scattering rules (Klemens 1958) and uses the experimental dispersion relation for silicon (Holland 1963), Fig. 3.3.3. The acoustic dispersion relation is divided into phonon bands, while the optical branch is assumed to have constant frequency (zero propagation velocity). Therefore, the optical phonons only influence the thermal conductivity via their scattering with acoustic phonons (Narumanchi, Murthy et al. 2004).

Case A: BTE-analysis of the wavelength cutoff restriction

We incorporate the wavelength cutoff restriction into the Boltzmann transport equation by omitting phonons with wavelengths larger than the simulation domain length, and all interactions with those phonons. The dashed portion of Fig. 3.3.3 represents the phonons omitted from the analysis. The size of the dashed region in Fig. 3.3.3 is inversely proportional to the number of lattice constants, N , used in each simulation domain direction. The frequency cutoff is included in Eq. (A.3.2) by setting the lower summation index of the longitudinal and transversal polarizations equal to $k/k_{max} = 1/N$.

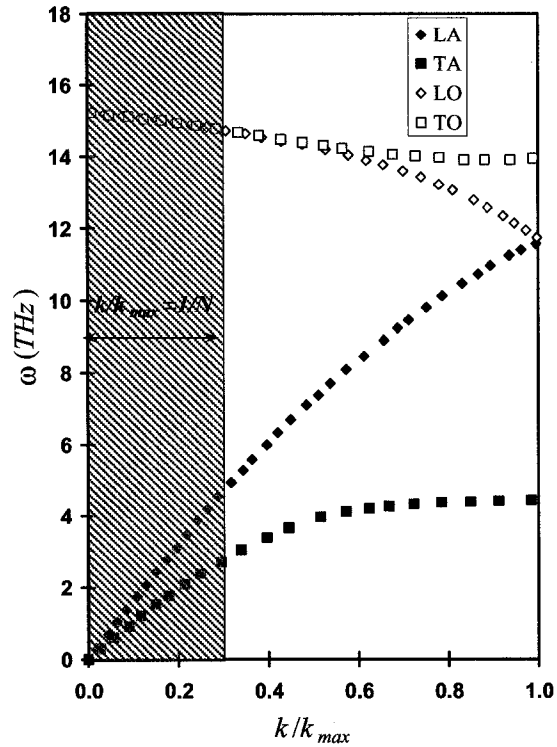


Figure 3.3.3. Experimental silicon dispersion relation in the [100] crystallographic direction (Holland 1963). The dashed portion represents the phonons that are omitted from the molecular dynamics simulation because of periodic boundary conditions restrictions.

Figure 3.3.4 shows the effect of the wavelength cutoff on the thermal conductivity predicted using BTE Eq. (A.3.2) for different domain sizes and temperatures. The results show that the predicted thermal conductivity increases with the number of lattice constants. For example, the BTE-predicted thermal conductivity with a wavelength cutoff corresponding to $10 \times 10 \times 10$ lattice constants is 31.37% and 29.56% smaller than the expected bulk value at 200 and 1000 K, respectively. Therefore, according with these results, the MD-predicted bulk thermal conductivity should approach the bulk thermal conductivity from below as larger molecular dynamics simulations domains are used. The results show that the reduction of the thermal conductivity with the reduction of the simulation domain size is slightly more severe at low temperatures (percentage wise). This is because the model predicts that phonons with large wavelength carry slightly more thermal energy at low temperature than they do at high temperature. For example, the combined longitudinal and transversal contribution to the thermal conductivity of the phonons excluded on a $4 \times 4 \times 4$ lattice constant simulation is 66.6% at 200 K while it is 61.5% at 1000 K. Most of this contribution comes from the transversal polarization (28.1% and 24.1% at 1000 and 200 K, respectively).

The results shown in Fig 3.3.4 can be explained by considering how the removal of phonons bands from the simulation alters the physics of the remaining phonon bands and, concurrently, the magnitude of the predicted thermal conductivity. The omission of certain phonon wavelengths (phonon bands) results in

two opposing effects. On one hand, excluding phonons bands from the simulation reduces the magnitude of the thermal conductivity because the energy carried by the omitted phonon bands is no longer included in the computation of the thermal conductivity. On the other hand, the removal of phonon bands results in less phonon bands to scatter with, which can increase the phonon mean free path and relaxation time of the allowed phonon bands, thereby increasing the thermal conductivity. Since the BTE-predicted thermal conductivity is smaller to or equal to the bulk value, it appears that the reduction in the magnitude of the thermal conductivity due to the absence of phonon bands is larger than any increase in thermal conductivity that might result from longer phonon mean free paths for the case under consideration.

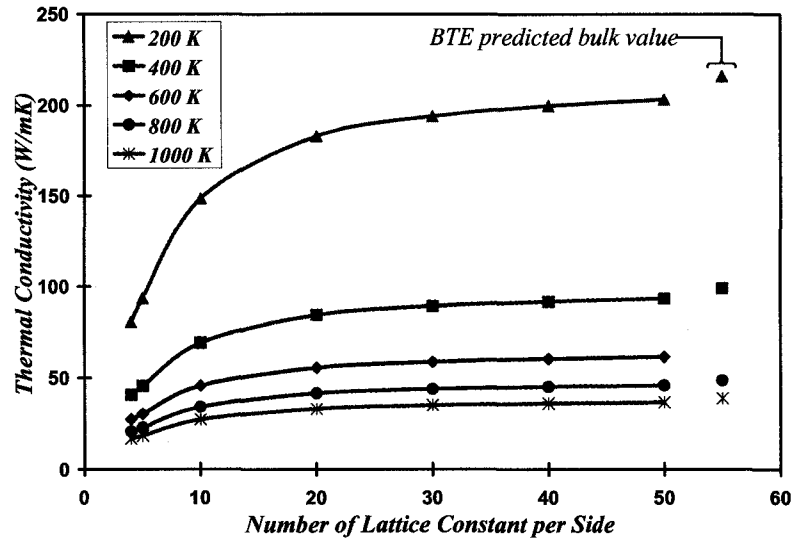


Figure 3.3.4. Variation of the BTE predicted bulk silicon thermal conductivity with wavelength cutoff for different temperatures (500 bands per acoustic polarization).

Figure 3.3.5 compares the phonon band contribution to the bulk thermal conductivity of two systems. One system includes all the phonon bands and their scattering processes (the entire dispersion curve), while the other system includes the phonon bands of phonons with wavelengths smaller than 10 lattice constants. Figure 3.3.5 suggest that excluding wavelengths larger than the simulation domain (wave-vectors to the left of the vertical line in Fig. 3.3.5) does not increase the contribution to the thermal conductivity of the remaining phonons (does not increase the remaining phonons' relaxation time as explained in section A.4). Therefore, the wavelength cutoff artifact reduces the magnitude of the thermal conductivity because it excludes the contribution of phonon bands to the thermal energy transport. The discontinuities in Fig. 3.3.5 are due to the range of application of Klemens' scattering rules, as explained in the Appendix A.

The size artifact predicted with this approach suggests that a system which excludes wavelengths larger than the simulation domain must have a reduced thermal conductivity. However, this is not the trend shown by the predicted molecular dynamics thermal conductivity (Fig. 3.2.3), in which the magnitude of the predicted thermal conductivity is found with a relatively small simulation domain (3x3x3) and

fluctuates around the value predicted using a simulation domain consisting of $10 \times 10 \times 10$ lattice constants. Therefore, we next analyze the effect of both wavelength cutoff and discreteness on the BTE-predicted thermal conductivity.

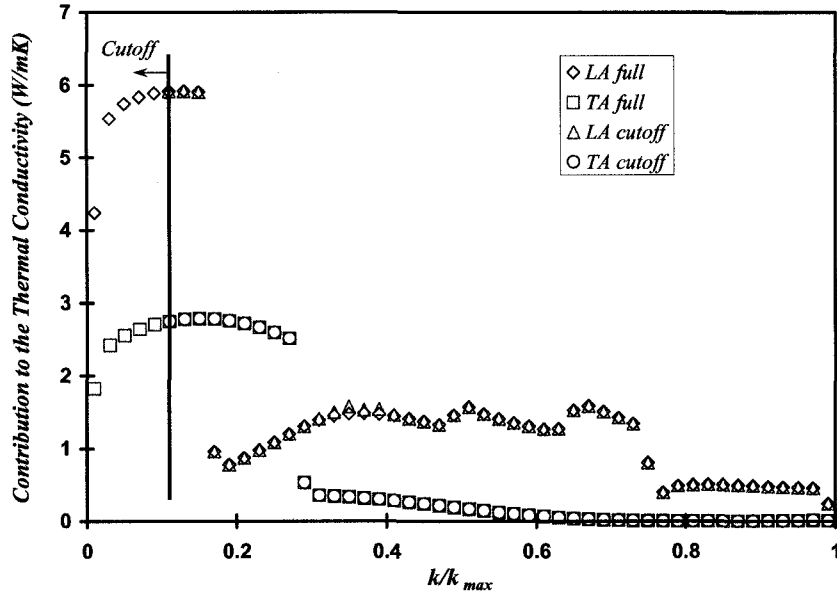


Figure 3.3.5. Contribution to the bulk thermal conductivity of the phonon bands (50 bands per acoustic polarization).

Case B: BTE-analysis of the discrete wavelength

The discrete wavelength are incorporated into the scattering term of the BTE by considering only those phonon bands centered at the allowed wavelengths ($\lambda=L/i$, where i is an integer ranging from one to the number of lattice constants in each direction) in the $[100]$ crystallographic direction. Klemens' scattering rules are used, but only scattering amongst the allowed phonon bands are considered.

Figure 3.3.6 shows the variation of the predicted thermal conductivity with the number of lattice constants per domain side. The vertical line separates two well-defined tendencies. To the left of the vertical line, the BTE-predicted thermal conductivity does not depend on temperature, and increases up to two orders of magnitude with respect to the bulk thermal conductivity as the simulation domain increases. This behavior is due to the lack of scattering processes among different phonon bands. Scattering occurs within each phonon band (intra-band scattering) and not with other phonon bands (multi-band scattering). Since this intra-scattering mechanism is temperature independent, the results are similar for the two temperatures studied. The thermal conductivity increases with the number of lattice constants because more phonon bands are included in a larger system. The vertical line in Fig. 3.3.6 defines the threshold at which scattering across different phonon bands starts. The thermal conductivities computed using simulation domains larger than the threshold exhibit two characteristics. First, in contrast to what was observed in *Case A*, the thermal conductivity predicted using only phonon bands center at the allowed wavelengths is

not smaller than that predicted using all the phonon bands. Second, the thermal conductivity fluctuates around the magnitude of the thermal conductivity predicted using all the phonon bands. Since a considerable number of bands are omitted from the analysis, the relaxation time of the allowed bands increases by up to one order of magnitude (Fig. 3.3.7). This increment in the relaxation time, within the context treated herein, is equivalent to an increment on the phonon mean free path of the allowed phonon bands due to the absence of scattering processes with the excluded phonon bands. Therefore, since the contribution of the allowed phonon bands to the thermal conductivity is proportional to the relaxation time (Eq. A.3.2), the predicted thermal conductivity magnitude does not decrease as in *Case A*. In addition, as the number of lattice constants is increased, different phonon bands are allowed. The contribution of each of these phonon bands to the thermal conductivity is different, resulting in a predicted thermal conductivity that fluctuates around the bulk value.

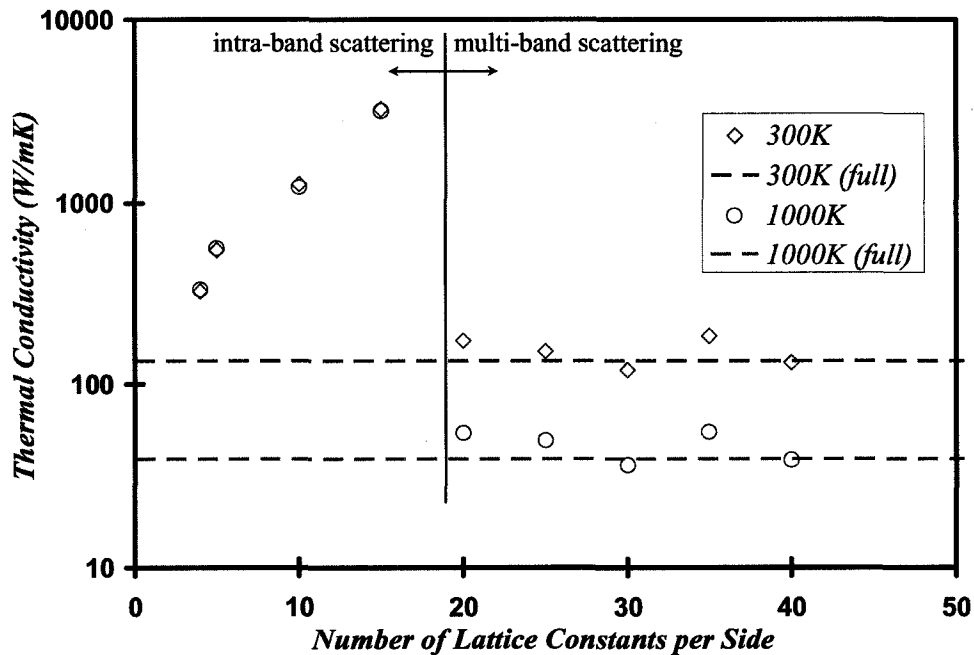


Figure 3.3.6. BTE predicted bulk silicon thermal conductivity including wavelength cutoff and filtering (50 bands per acoustic polarization).

Figures 3.3.7 (a) and (b) shows the phonon bands relaxation times for the longitudinal and transversal acoustic polarizations, respectively. Two different systems are studied: one system includes all the phonon bands and their scattering processes (the entire dispersion curve), while the other system includes those phonon bands centered at the allowed wavelengths $\lambda=L/i$, with L equal to 25 lattice constants. The figures show that the relaxation times of the discrete system are equal to or larger than those of the system that includes all the phonon bands. The relaxation time of the allowed phonon bands that have all the other phonon bands they scatter with included in the system remain the same. However, the relaxation time of the

allowed phonon bands that have some of the phonon bands they scatter with removed from the system increases. This behavior was found for all the systems with a simulation domain size larger than the threshold indicated by the vertical line in Fig. 3.3.5.

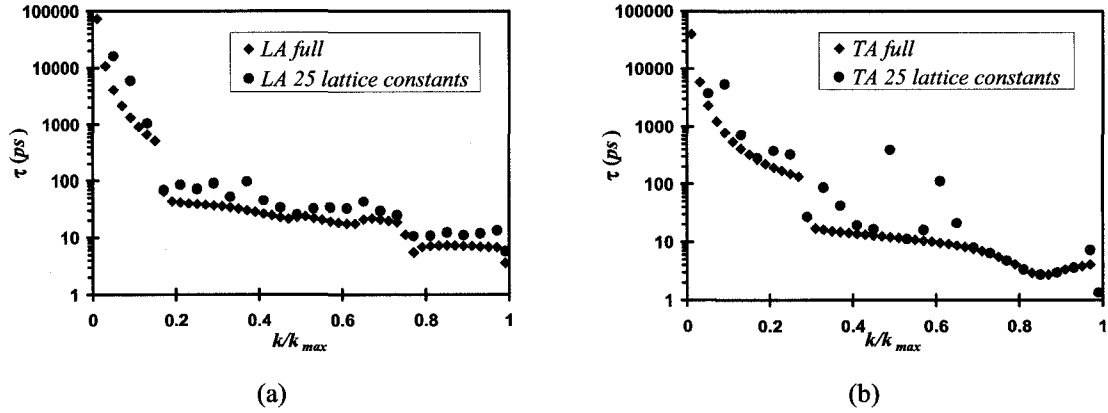


Figure 3.3.7. Phonon bands' relaxation times for (a) longitudinal acoustic and (b) transversal acoustic at 300 K, computed using the phonon band approximation and the phonon filtering.

Figure 3.3.8 shows the contribution to the thermal conductivity of each of the longitudinal and transversal acoustic bands, for the system with all the phonon bands (solid symbols) and for the system with the allowed phonon bands (open symbols). The phonon contribution of the system with all the phonon bands is plotted on the left vertical axis, while the contribution of the restricted system is plotted on the right vertical axis. The figure shows that the contribution of the phonon bands of the discrete system to the thermal conductivity is larger than the contribution of the phonon bands of the complete system.

The number of allowed phonon frequencies, Eq. (3.3.1) and phonon-phonon scattering events in a system of size $L \times L \times L$ is larger than that allowed by the one-dimensional restriction enforced for the analysis presented in this section, $\lambda = L/i$. Therefore, the threshold between a system with intra-band scattering and a system with multi-bands scattering (the vertical line reported in Fig. 3.3.5) should occur at a lower simulation domain size. That is, the predicted thermal conductivity using periodic boundary conditions should equal to the bulk thermal conductivity using fewer lattice constants per side.

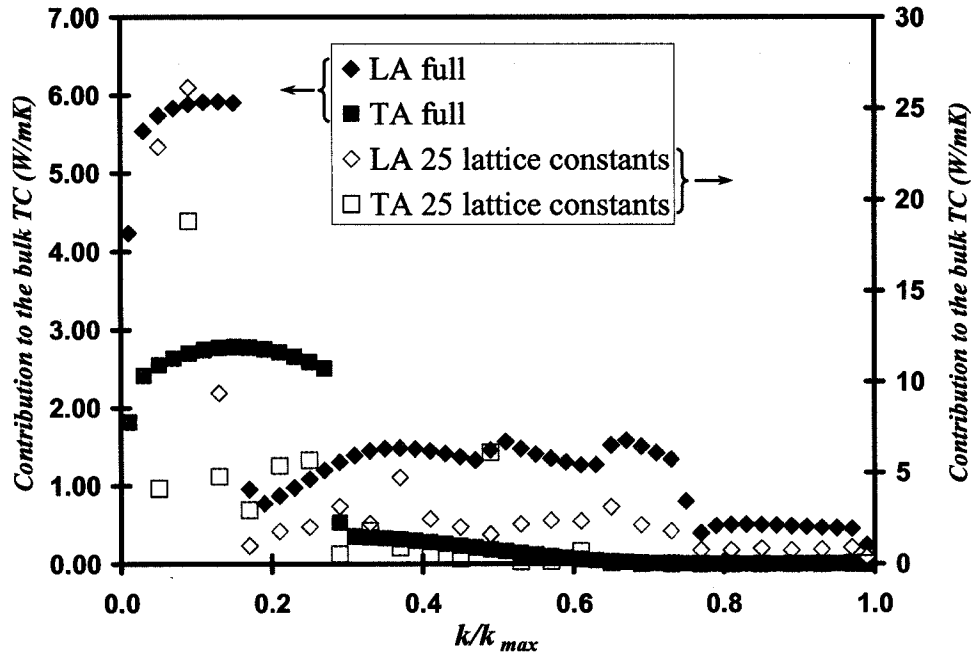


Figure 3.3.8. Band contribution to the thermal conductivity for a system with all the phonon bands and for a system with filtered bands.

3.4 Conclusions

This chapter presents the bulk silicon thermal conductivity computed using equilibrium molecular dynamics, the Green-Kubo formalism and the Stillinger-Weber potential, in the temperature range 240 to 1000 K. We show that the MD-predictions follow the temperature dependence observed experimentally. Simulations are performed using different sizes of simulation domains (from 2x2x2 to 10x10x10 lattice constants), and applying periodic boundary conditions to simulate an infinite system.

Our results show that using less than two million samples to average the heat current autocorrelation function affects the predicted bulk silicon thermal conductivity. Additionally, our molecular dynamics simulations performed using different values of the lattice constant show that the predicted bulk silicon thermal conductivity with the Stillinger-Weber potential is independent (within the statistical error) of the stretching or compressing of the crystalline lattice for temperatures of the molecular dynamics simulation of 300 and 1000 K, and lattice constants of 0.543 and 0.545 nm. Therefore, the experimentally determined silicon lattice parameter at 300 K (0.543 nm) (Madelung 1996) is used for all simulations.

Our predictions also show that, for simulation domains between 3x3x3 and 10x10x10 lattice constants, there is no dependence of the bulk silicon thermal conductivity on the simulation domain size. Therefore, a relatively small simulation domain can be used to predict bulk silicon thermal conductivity, saving computational time.

As a consequence of using periodic boundary conditions, the phonon wavelengths are discrete and there is a maximum wavelength allowed. The effect of these wavelength restrictions on the predicted thermal conductivity is studied using the Boltzmann transport equation. The results show that the relaxation times of the allowed phonons, computed using Klemens' scattering rules, do not change considerably when only phonons with wavelengths larger than the simulation domain are not considered. Therefore, the magnitude of the thermal conductivity predicted with this wavelength cutoff restriction is always smaller than that of a system that includes all phonon wavelengths. This conclusion does not agree with our molecular dynamics results, which show that the thermal conductivity predicted with relatively small simulation domains equals that of larger domains. Thus, the wavelength cutoff restriction does not explain the lack of size artifact observed in the MD simulations.

The effect of the discrete phonon on the predicted thermal conductivity is also considered. The study shows that the magnitude of the predicted thermal conductivity remains nearly constant with the number of lattice constants when enough lattice constants are used. The magnitude of the thermal conductivity remains constant because, although fewer phonon bands are allowed by the system, the relaxation time - and the mean free path - of the allowed phonon band increases. The increment in the magnitude of the relaxation time compensates for the contribution of the missing bands to the thermal conductivity. In other words, the phonons allowed by the system carry the energy longer distances in their propagation direction before scattering with other phonons. The trend shown by the thermal conductivity computed in the discrete wavelength study agrees with that shown by the molecular dynamics determined thermal conductivity. That is, the magnitude of the thermal conductivity computed using relatively smaller simulation domains fluctuates around the magnitude of the thermal conductivity computed using a large domain.

3.5 References

- Abeles, B., D. S. Beers, et al. (1962). "Thermal Conductivity of Ge-Si Alloys at High Temperatures." Physical Review **125**(1): 44-46.
- Ashcroft, N. W. and N. D. Mermin (1976). Solid State Physics. New York, Harcourt College Publishers.
- Glassbrenner, C. J. and G. A. Slack (1964). "Thermal Conductivity of Silicon and Germanium from 3K to the Melting Point." Physical Review **134**(4A): A1058-A1068.
- Gomes, C., M. Madrid, et al. (2003). Parallel Molecular Dynamics Code Validation Through Bulk Silicon Thermal Conductivity Calculations. 2003 ASME International Mechanical Engineering Congress and Exposition, Washington DC, ASME.
- Ho, C. Y., R. W. Powell, et al. (1972). "Thermal Conductivity of the Elements." Journal of Physical Chemistry Ref. Data **1**: 279-421.
- Holland, M. G. (1963). "Analysis of Lattice Thermal Conductivity." Physical Review **132**(6): 2461-2471.
- Klemens, P. G. (1958). Thermal Conductivity and Lattice Vibrational Modes. Solid State Physics. F. Seitz and D. Turnbull. New York, Academic Press. **7**: 1-98.
- Kremer, R. K., K. Graf, et al. (2004). "Thermal Conductivity of Isotopically Enriched ²⁸Si: Revisited." Solid State Communications **131**: 499-503.
- Lukes, J. R., D. Y. Li, et al. (2000). "Molecular Dynamics Study of Solid Thin-Film Thermal Conductivity." Journal of Heat Transfer **122**: 536-543.
- Madelung, O., Ed. (1996). Semiconductors Basic Data. Berlin, Springer-Verlag.

- McGaughey, A. J. and M. Kaviany (2004). "Quantitative Validation of the Boltzman Transport Equation Phonon Thermal Conductivity Model Under the Single-Mode Relaxation Time Approximation." Physical Review B **69**(9): 094303(1)-094303(11).
- Narumanchi, S. V. J., J. Y. Murthy, et al. (2004). "Comparison of Different Phonon Transport Models for Predicting Heat Conduction in Silicon-on-Insulator Transistors." ASME Journal of Heat Transfer(in review).
- Porter, L. J., J. F. Justo, et al. (1997). "The Importance of Grüneisen Parameters in Developing Interatomic Potentials." Journal of Applied Physics **82**(11): 5378-5381.
- Porter, L. J., J. Li, et al. (1997). "Atomistic modeling of finite-temperature properties of B-SiC. I. Lattice vibrations, heat capacity and thermal expansion." Journal of Nuclear Materials **246**: 53-59.
- Schelling, P. K., S. R. Phillpot, et al. (2002). "Comparison of Atomic-Level Simulation Methods for Computing Thermal Conductivity." Physical Review B **65**: 144306(1)-144306(12).
- Tien, C.-L., A. Majumdar, et al., Eds. (1998). Microscale Energy Transport. Series in Chemical and Mechanical Engineering. Washington DC, Taylor and Francis.
- Volz, S. G. and G. Chen (2000). "Molecular-Dynamics Simulation of Thermal Conductivity of Silicon Crystals." Physical Review B **61**(4): 2651-2656.

Chapter 4:

In-Plane Thin film Thermal Conductivity Prediction

This chapter presents the numerical prediction of silicon thin film thermal conductivity using equilibrium molecular dynamics and the Green-Kubo formalism. Section 4.1 presents a review of the boundary conditions used in molecular dynamics to model films surfaces. Section 4.2 deals with the definition of an appropriate set of boundary conditions for the film's out-of plane direction. Section 4.3 defines the mathematical expression for the heat current through the film surfaces. This section also verifies, numerically, that the proposed boundary conditions can be used with the Green-Kubo formalism. We show that molecular dynamics simulations using the proposed boundary condition can reproduce the surface reconstruction of the [100] silicon surface. Section 4.4 presents the numerical methodology used to estimate the silicon thin film thermal conductivity. Last, Section 4.5 presents the predicted in-plane¹ silicon thin film thermal conductivity for temperatures ranging from 240 to 1000 K.

4.1 Thin Film Surface Boundary Condition Review

To simulate an infinite slab, molecular dynamics can be performed on a simulation domain consisting of a finite number of lattice constants by applying periodic boundary conditions in the directions parallel to the film surfaces (the in-plane directions) (Fig. 4.1.1). Strategies used to treat the surfaces of thin films include free boundary conditions (Weakliem and Carter 1992; Yu and Clancy 1994; Lukes, Li et al. 2000; Feng, Li et al. 2003), constraining the surface atoms by either adding layers of atoms kept frozen (Lukes, Li et al. 2000; Chantrenne and Barrat 2003) or by linking the surface atoms to their equilibrium position through a weak harmonic potential (Chantrenne and Barrat 2004). Free surface boundary conditions have been used to predict the out-of-plane thermal conductivity of argon (Lukes, Li et al. 2000) and silicon (Feng, Li et al. 2003) thin films using non-equilibrium molecular dynamics, the longitudinal thermal conductivity of silicon nanowires (Volz and Chen 1999), and the atomic reconstruction of silicon surfaces (Weakliem and Carter 1992; Yu and Clancy 1994). Ideally, this technique provides zero heat flux through the free surfaces, while allowing for the reordering of the surface atoms. Special attention has to be given to prevent rigid body motion perpendicular to the free surfaces. However, molecular dynamics simulations using this technique may not finish successfully, because atoms on the first layers can escape the simulation domain creating a chain reaction that propagates to the internal layer (Yu and Clancy 1994; Lukes, Li et al. 2000). A strategy used to avoid this problem involves reducing the time step with respect to that used for bulk silicon simulations (Volz and Chen 1999). Although this strategy has been successfully implemented, it increases the computational cost and does not guarantee the successful completion of the simulation. To

¹ The term *in-plane* or *parallel* is used to indicate the direction parallel to the film surface. In the same way, the term *perpendicular* or *out-of-plane* is used to indicate the direction normal to the film surfaces.

prevent the evaporation of the surface atoms, the system can be delimited with a few layers of atoms kept frozen at their equilibrium positions (Volz and Chen 1999; Lukes, Li et al. 2000), or restrained by a weak harmonic potential (Chantrenne and Barrat 2004). These strategies allow controlling the stress levels perpendicular to the surfaces and the use of a reasonable time step, while preventing rigid body motion in the direction perpendicular to the frozen surface. However, these strategies prevent the first layers of non-restrained atoms from rearrange themselves into the minimum potential energy configuration. Therefore, due to the discussed limitations of current techniques to simulate free surfaces, it is important to develop an appropriate boundary condition to treat the surface atoms in a realistic and computationally efficient manner.

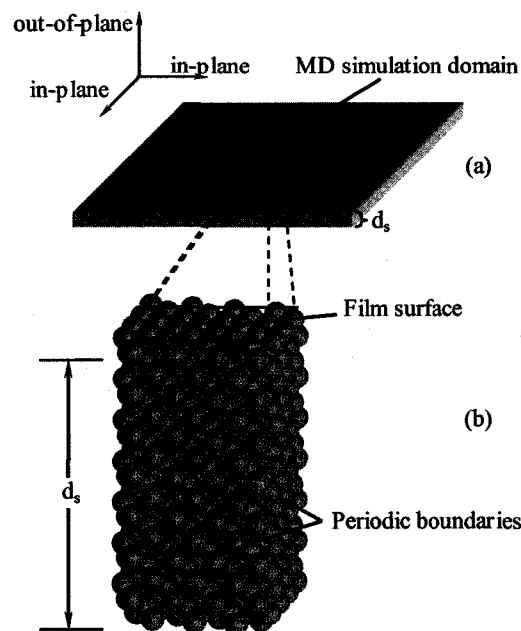


Figure 4.1.1. (a) Sketch of a thin film defining the in-plane and out-of-plane directions and the film thickness d_s . (b) Molecular dynamics simulation domain consisting of $4 \times 4 \times 8$ silicon lattice constants.

4.2 Potential-Like Boundary Condition

We are seeking a potential to represent the effect that a surrounding isothermal and inert gas would have on the free surfaces of a silicon thin film. The gas is assumed to be macroscopically static and in thermal equilibrium with the silicon film. Under these conditions, the net heat flux through the film's surfaces is zero and the average shear stresses due to gas flow must be zero. To represent the gas-solid interaction, we propose a potential with the following characteristics:

- *Short-ranged*, because the gas molecules colliding with the solid surfaces interact only with the first few atomic layers.
- *One-dimensional*, because the net effect of a macroscopically static surrounding gas on the film is a pressure acting perpendicular to the film's surfaces.

- *Repulsive*, so that there is no attractive term that may result in bonds between the surface atoms and the gas molecules. A repulsive potential also results in a positive pressure that prevents the evaporation of the surface atoms.

The mathematical expression of the proposed surface potential is similar to the two-body repulsive term of the Stillinger-Weber (Stillinger and Weber 1985) potential for silicon,

$$\phi_w(d) = \begin{cases} \varepsilon \left(\frac{\sigma}{d} \right)^p \cdot e^{-\frac{\sigma}{d - \sigma_{cw}}} & d < \sigma_{cw} \\ 0 & d \geq \sigma_{cw} \end{cases} \quad (4.2.1)$$

where ϕ_w is the repulsive potential, ε is the potential energy scaling factor in Joules, σ is the characteristic distance in m, and r_{cw} is the dimensionless cutoff radius. While in the two-body Stillinger-Weber potential, d is the interatomic distance; here, d is the distance between any given atom and the repulsive potential reference plane, Fig. 4.2.1(b).

The position of the reference plane is given by an arbitrary point located on the plane, while the orientation of the plane (the direction of action of the potential) is given by the unit vector \vec{n} :

$$\vec{n} = n_x \vec{e}_x + n_y \vec{e}_y + n_z \vec{e}_z \quad (4.2.2)$$

where n_x , n_y and n_z are the components of the unit vector along the x , y and z direction, respectively. Figure 4.2.1(a) shows the graphical representation of the reference point, the reference plane, the unit vector and the distance d , while, Figure 4.2.1(b) shows, schematically, the location of the repulsive potential with respect to the film's surfaces.

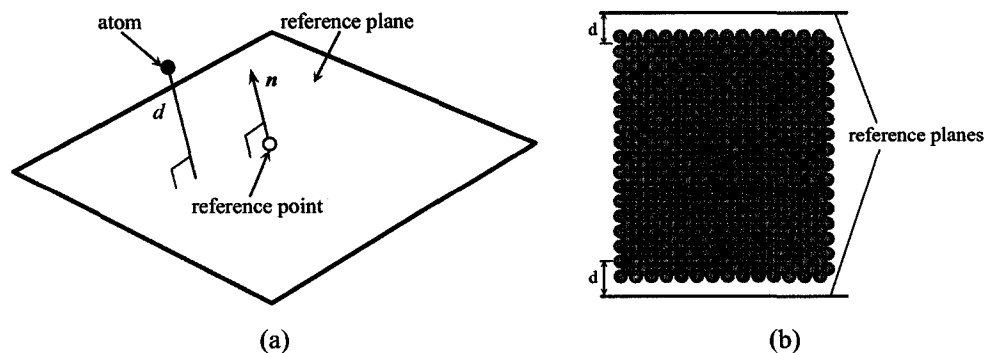


Figure 4.2.1. (a) Sketch of the repulsive potential reference point, reference plane, unit vector and distance d ; (b) Sketch of the repulsive potential location with respect to the thin film atoms.

The magnitudes of the repulsive potential parameters used are listed in Table 4.2.1.

Table 4.2.1. Repulsive potential parameters.

Parameter	Value
ϵ	1.474×10^{-19} J
σ	2.0951×10^{-10} m
p	4.0
r_{cw}	1.26

The force on atom i due to the repulsive potential is given by:

$$\vec{F}_{iw}^i = \phi_w(d_i) \left(\frac{p}{d_i} + \frac{\sigma}{(d_i - \sigma r_c)^2} \right) \vec{n} \quad (4.2.3)$$

where \vec{F}_{iw}^i is the force on atom i , in N. The scalar quantities in Eq. (4.2.3) are always positive; therefore, the direction of the repulsive force coincides with the direction of the unit vector. Hence, the unit vector should point into the thin film to result in a positive net pressure. Additionally, since the repulsive potential acts in the direction perpendicular to the film, it allows for the free reconfiguration of the atoms in the surface (Section 4.3.1).

4.3 Repulsive Potential: Further Considerations and Validation

This Section addresses additional theoretical and computational aspect of predicting silicon in-plane thermal conductivity using the Green-Kubo formalism and the proposed potential-like boundary condition.

4.3.1 Microcanonical ensemble verification

To predict thermal conductivities using the Green-Kubo formalism, the number of particles, volume and total energy in the ensemble should remain constant, i.e. the ensemble should be microcanonical. The number of atoms in the ensemble is preserved because the repulsive potential prevents the surface atoms from evaporating (Gomes, Madrid et al. 2004). Additionally, the location of the reference planes is chosen such that the atomic ensemble cannot expand or translate, remaining within a fixed volume. Next, we show, analytically, that, at low temperatures the average energy of the ensemble is constant.

The heat flow is defined as (Hardy 1963; Allen and Tildesley 1987; McGaughey and Kaviany 2002):

$$\vec{J} = \frac{\partial}{\partial t} \left(\sum_{i=1}^N \vec{x}_i \cdot E_i \right) \quad (4.3.1)$$

where \vec{x}_i represents the atomic positions of atom i , and the total energy, E_i , stored in atom i is the sum of the kinetic and potential energies:

$$E_i = \frac{1}{2} m_i \vec{v}_i \cdot \vec{v}_i + \frac{1}{2} \sum_{j \neq i} \phi_2 + \frac{1}{6} \sum_{j \neq i} \sum_{k \neq i, j} \phi_3 + \frac{1}{2} \phi_w(d_i) \quad (4.3.2)$$

where the first term on the right hand side is the kinetic energy of atom i ; the second and third terms are the contributions from the two- and three-body Stillinger-Weber interatomic potentials (Stillinger and Weber 1985) and the last term is the contribution from the repulsive potential, which is non-zero only for atoms that are within the repulsive potential cutoff radius.

The heat flowing through a film surface, \bar{J}_w , is obtained by isolating the contribution of the repulsive potential to the heat flow, Eq. (4.3.3):

$$\bar{J}_w = \bar{n} \sum_i^{N_w} \left[\phi_w(d_i) \left(p + \frac{\sigma d_i}{(d_i - \sigma r_c)^2} \right) \right] (\bar{n} \cdot \vec{v}_i) \quad (4.3.3)$$

where the sum is over the number of atoms within the repulsive potential cutoff radius, N_w . Note, that \bar{J}_w is a vector whose direction is given by the unit vector \bar{n} (which is perpendicular to the film surface). Additionally, the sign of the atomic velocity perpendicular to the film surface (dot product between the normal vector and the atomic velocity) give the direction of propagation of the heat flow, since the term between brackets in Eq. (4.3.3) is always positive. Therefore, atoms moving towards the repulsive potential lose thermal energy to the repulsive potential (the surrounding gas), while atoms moving away from the repulsive potential gain thermal energy from the repulsive potential (the surrounding gas).

At low temperatures, it can be assumed that the amplitudes of vibration in the out-of-plane direction of the atoms on the surface are small enough so that the distance between the surface atoms (atoms on the first layers) and the reference plane can be considered constant. Thus, the term within brackets in Eq. (4.3.3) becomes a constant and can be taken out of the summation, reducing Eq. (4.3.3) to the multiplication of a constant by the arithmetic summation of the atomic velocity perpendicular to the film surface (the inter product between the atomic velocity and the unit vector normal to the surface). This summation fluctuates around zero because in average the number of atoms on the film's surface moving towards the film equals those moving away from it. Therefore, the time average of the heat flow through the film's surfaces is equal to zero and the energy in the ensemble is conserved at low temperatures.

The heat flux through the film surfaces, (given by \bar{J}_w divided by the simulation surface area), is computed during the molecular dynamics simulations. Figure 4.3.2 shows that the heat flux through the

surface of a simulation domain composed of $7 \times 7 \times 8$ lattice constants at 1000 K fluctuates around zero during the simulation. The same behavior is found for all the cross sections studied (2×2 , 4×4 , 7×7 and 10×10). Thus, simulations performed with the repulsive potential represent appropriately two systems at thermal equilibrium (the net thermal energy interchanged between a thin film and the surrounding gas at thermal equilibrium is zero). In addition, as the simulation cross section area increases, so does the probability of finding atoms that are transferring the same amount of thermal energy to and from the surroundings, leading to a decrease of the heat current standard deviation, this is shown in Fig. 4.3.3.

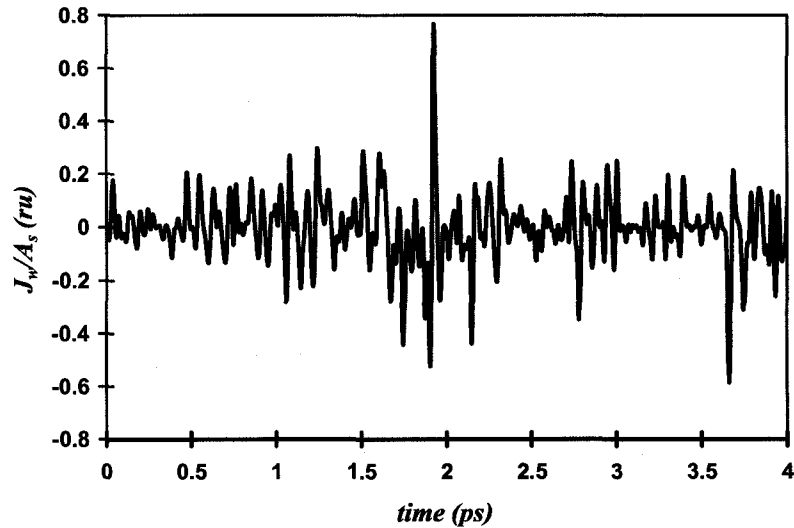


Figure 4.3.2. Fluctuation of the heat flux through the film surface for a $7 \times 7 \times 8$ lattice constants simulation at 1000 K.

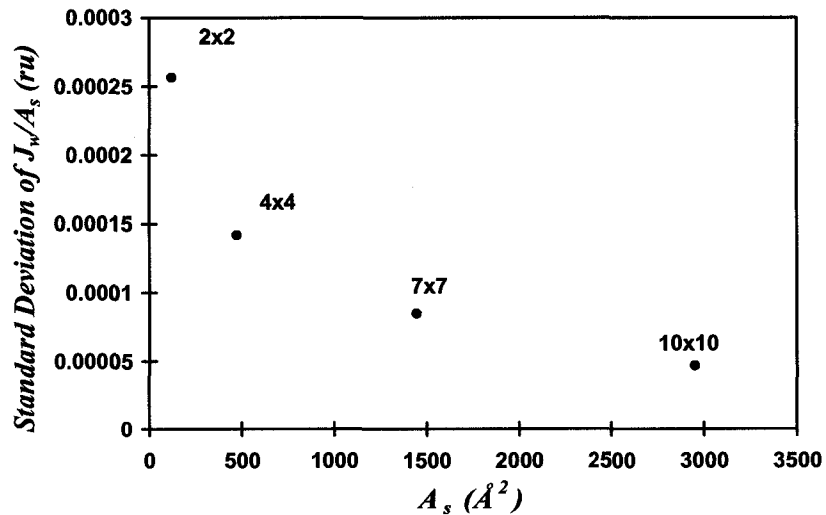


Figure 4.3.3. Standard deviation of the heat flux through the film surface vs cross section size.

4.3.2 Green-Kubo relation for determining the in-plane thermal conductivity

For in-plane thin films thermal conductivity predictions, the heat current autocorrelation is averaged over the two in-plane directions, Eq. (4.3.4), instead of three directions as used for isotropic bulk thermal conductivity, Section 2.2.4. Since \vec{J}_w (Eq. (4.3.3)) acts in the out-of-plane direction, it does not contribute to the in-plane thermal conductivity calculation,

$$k_{ip} = \frac{1}{2Vk_B T^2} \int_0^{\infty} \langle \vec{J}(\tau) \cdot \vec{J}(0) \rangle d\tau \quad (4.3.4)$$

where k_{ip} is the equivalent in-plane film thermal conductivity, V is the ensemble volume, T is the ensemble average temperature, k_B is Boltzmann's constant, \vec{J} is the in-plane heat current vector, and the integrand is the ensemble average of the in-plane heat current autocorrelation function.

Replacing the integral in Eq. (4.3.4) by a sum over equal-sized time steps Δt :

$$k_{ip_{MD}}(\tau_M) = \frac{\Delta t}{2Vk_B T_{MD}^2} \sum_{m=1}^M \frac{1}{N_s - m} \sum_{n=1}^{N_s - m} \vec{J}(m+n) \cdot \vec{J}(n) \quad (4.3.5)$$

where N_s is the number of heat current autocorrelation function averages; M is the number of time steps required for the heat current autocorrelation function to decay to zero; and τ_M is the integration time given by $\Delta t.M$. As for the bulk thermal conductivity predictions, the integration time should be longer than the time required for the heat current autocorrelations to decay to zero. We found that $N_s \approx 5.5 \times 10^6$ samples (with samples collected every time step of 0.55 fs) are enough for molecular dynamics estimation of silicon thin film thermal conductivity using the repulsive potential boundary condition (Gomes, Madrid et al. 2004).

4.3.3 Quantum corrections for the in-plane thermal conductivity

Hu et al. (Hu, Wang et al. 2004) proved analytically that the magnitude of the specific heat of silicon nanocrystal is very similar to that of bulk silicon. Due to lack of additional experimental data, the quantum corrections computed using the bulk specific heat experimental data, Section 2.2.4, are used for the quantum correction of the thin film temperature of the molecular dynamics simulation and the in-plane thermal conductivity.

4.3.4 Insensitivity of the predicted in-plane thermal conductivity to the repulsive potential parameters

Figure 4.3.4 shows the dependence of the repulsive potential with the distance from the reference plane, for different values of ϵ . We found that the choice of ϵ does not affect the value of the predicted in-plane thermal conductivity for values of ϵ ranging between 1.736×10^{-19} J to 1.736×10^{-18} J.

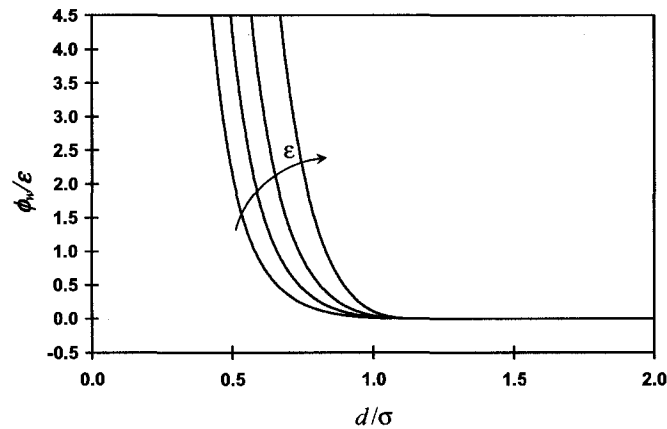


Figure 4.3.4. Variation of the repulsive potential (non-dimensional) with distance from the reference plane (non-dimensional) for values of ϵ given in the direction of the arrow of 0.5ϵ , ϵ , 2ϵ and 5ϵ .

The distance between the first layer of atoms and the reference plane is set to 0.264 nm at the beginning of the simulation. This distance was chosen because preliminary simulations showed that smaller separations generate unrealistic elastic waves at the beginning of the simulation, while larger separations allow the film to bounce back and forward between the reference planes creating fluctuations in the heat current autocorrelation functions.

4.3.5 Size artifacts

Figure 4.3.5 shows the variation of the predicted in-plane thermal conductivity with the number of lattice constants used in each of the in-plane direction for a film thickness of 4.344 nm (8 lattice constants) and temperatures of the molecular dynamics simulation of 300 and 1000 K. Given the insensitiveness of the predicted bulk thermal conductivity to the simulation domain size at 1000 K and the small variation (about 2%) of the predicted in-plane thermal conductivity with the simulation cross-section size ranging from 2x2 to 7x7 lattice constants at 1000 K, no further domain sizes were considered. The predicted in-plane thermal conductivity at 300 K for 2x2 and 10x10 lattice constants cross sections are within the standard deviation of each other. In conclusion, given the negligible variation of the predicted in-plane thermal conductivity at 1000 K, the acceptable variation of the predicted in-plane thermal conductivity at 300 K and the considerable increment in the computational cost of incrementing the cross section size to 10x10 lattice constants, only 2x2 lattice constant cross-sections are considered.

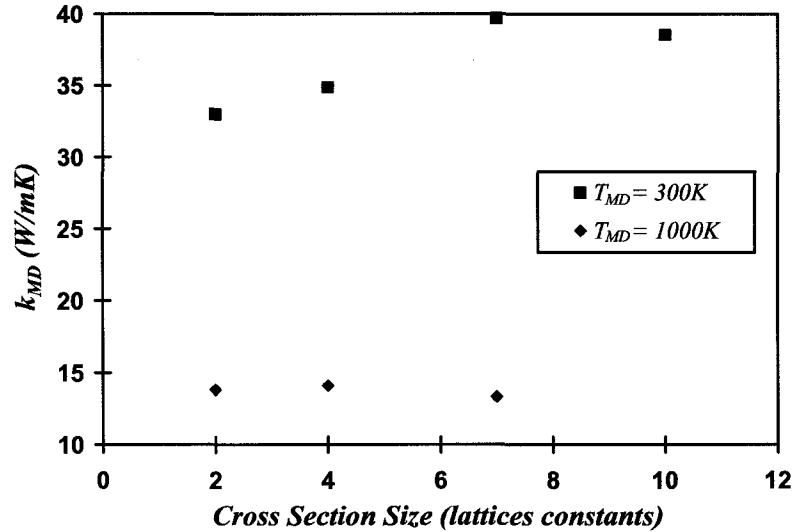


Figure 4.3.5. Influence of simulation cross-section size on the predicted thermal conductivity for repulsive potential boundary condition.

Figure 4.3.6 shows the phonon frequency spectra of a $2 \times 2 \times 48$ lattice constants thin film simulations at 1000 K when using the repulsive potential as boundary conditions. The spectra of frequencies reported in Fig. 4.3.6(a) and (b) are computed using the in-plane and out-of-plane components of the atomic velocity of an atom located on the film center layer, respectively. The spectra of frequencies computed using the in-plane component of the atomic velocity is the same for both in-plane directions.

Note that the phonon spectra captured by the simulation differs depending on whether the velocity component used for computing the Fourier spectra coincides with the in-plane direction (Fig. 4.3.6(a)) or the out-of-plane direction (Fig. 4.3.6(b)). This discrepancy is due to the difference on the allowed phonons in the in-plane direction and the out-of-plane direction. Additionally, the spectra reported in Figs. 4.3.6 (a)-(b) differ from the bulk phonon spectra of a $2 \times 2 \times 2$ lattice constants simulation reported in Fig. 4.3.7 in two aspects. First, the number of peaks (phonon frequencies) allowed by the thin film simulation above the cutoff frequencies reported in Fig. 4.3.7 is larger than the phonon frequencies allowed by the bulk simulation due to the larger number of atoms in the thin film simulation domain. Second, Fig. 4.3.6 (a)-(b) show additional peaks (at the allowed wavelengths) below the cutoff frequencies reported in Fig. 4.3.7. These frequencies are due to the large number of lattice constant used in the out-of-plane direction. The transversal acoustic out-of-plane phonon frequencies are captured in the in-plane spectra while the longitudinal acoustic out-of-plane phonon frequencies are captured on the out-of-plane spectra. Table 4.3.1 compares the magnitude of the additional frequencies reported in Fig. 4.3.6(a) and (b) to the allowed transversal and longitudinal acoustic frequencies computed from the Stillinger-Weber dispersion relation in the [100] crystallographic direction (Porter, Yip et al. 1997). The allowed frequencies are computed at the phonon wavelengths given by $\lambda = 48a_0/i$. The additional out-of-plane phonon frequencies captured by the

molecular dynamics simulation are in good agreement with the frequencies computed using the Stillinger-Weber dispersion relation at the allowed wavelength.

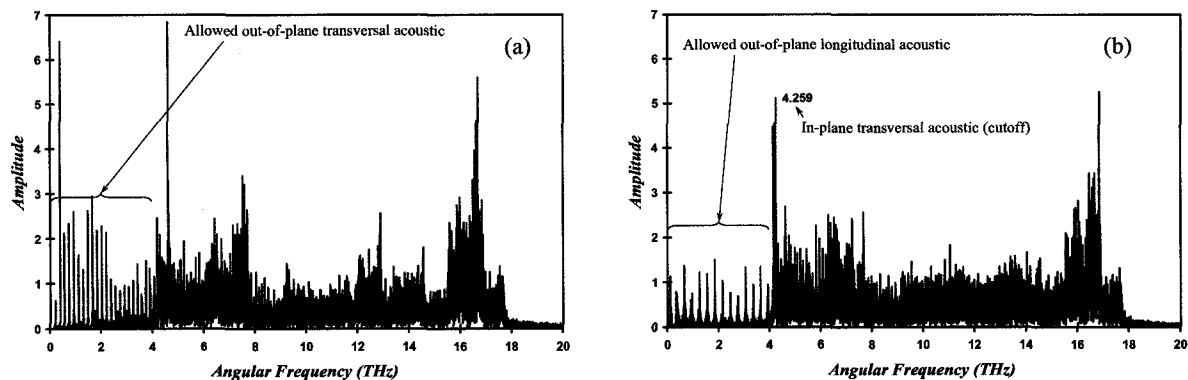


Figure 4.3.6. Phonon spectra of a 2x2x48 lattice constants silicon thin film in (a) the in-plane direction and (b) the out-of-plane direction.

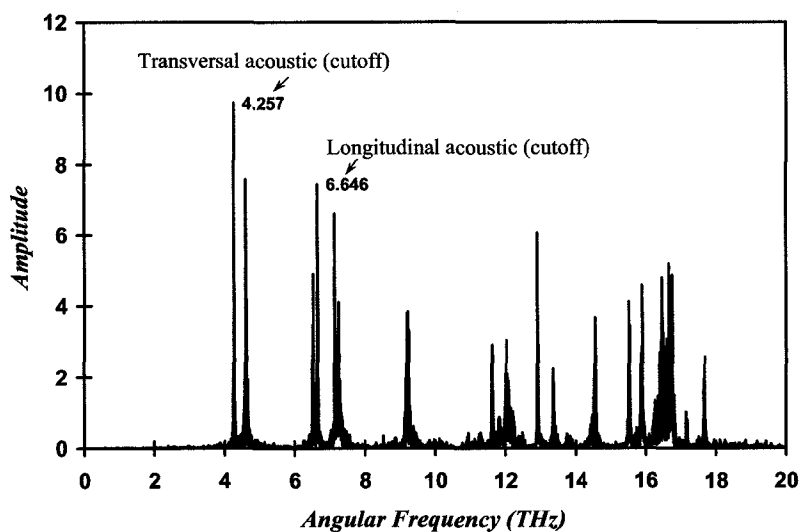


Figure 4.3.7. Phonon spectra of a 2x2x2 lattice constants bulk silicon simulation.

Due to the larger number of phonons allowed in the thin film simulation, it is expected that the physics of the phonons allowed in a thin film simulation with 2x2 lattice-constants cross section to be closer to the physics of the phonons captured by a thin film simulation with infinite cross section, than the physics of the phonons of a 2x2x2 bulks silicon simulation is from an infinite bulk silicon simulation.

Table 4.3.1. Comparison of the out-of-plane phonon frequencies captured by the molecular dynamics simulation of a 2x2x48 lattice constants silicon thin film to the phonon frequencies predicted using the allowed wavelength in the out-of-plane direction.

i	Transversal Acoustic (THz)		Longitudinal Acoustic (THz)	
	Fourier (Fig. 4.3.6 (a))	Predicted	Fourier (Fig. 4.3.6 (b))	Predicted
1	0.178	0.187	0.313	0.369
2	0.358	0.371	0.625	0.655
3	0.539	0.553	0.936	0.955
4	0.722	0.737	1.246	1.248
5	0.906	0.921	1.554	1.547
6	1.091	1.106	1.862	1.848
7	1.276	1.287	2.168	2.148
8	1.462	1.47	2.473	2.454
9	1.649	1.652	2.776	2.75
10	1.835	1.829	3.078	3.05
11	2.021	2.011	3.379	3.352
12	2.207	2.19	3.678	3.647
13	2.392	2.363	3.975	3.943
14	2.576	2.542	The Fourier spectra in the out-of-plane direction becomes too crowded above ~4 THz to retrieve the desired data	
15	2.759	2.721		
16	2.941	2.894		

4.3.6 Surface reconstruction

The effect of the repulsive potential on the silicon surface in the [100] crystallographic direction is examined by performing a molecular dynamics simulation on a domain with 10x10x8 lattice constants (eight lattice constants in the out-of-plane direction). Figure 4.3.8(a) shows the starting configuration of the silicon atoms on the surface layer, with the atoms located at the face centered cube location. Figure 4.3.8(b) shows the same first atomic layer after 100,000 steps of molecular dynamics. The silicon atoms have spontaneously rearranged to form dimers aligned in the [110] crystallographic direction, while the group of dimers form lines aligned in the $[\bar{1}\bar{1}0]$ crystallographic direction. This reconstructed surface is consistent with experimental observations and previous numerical and theoretical studies of the silicon (100) surface.

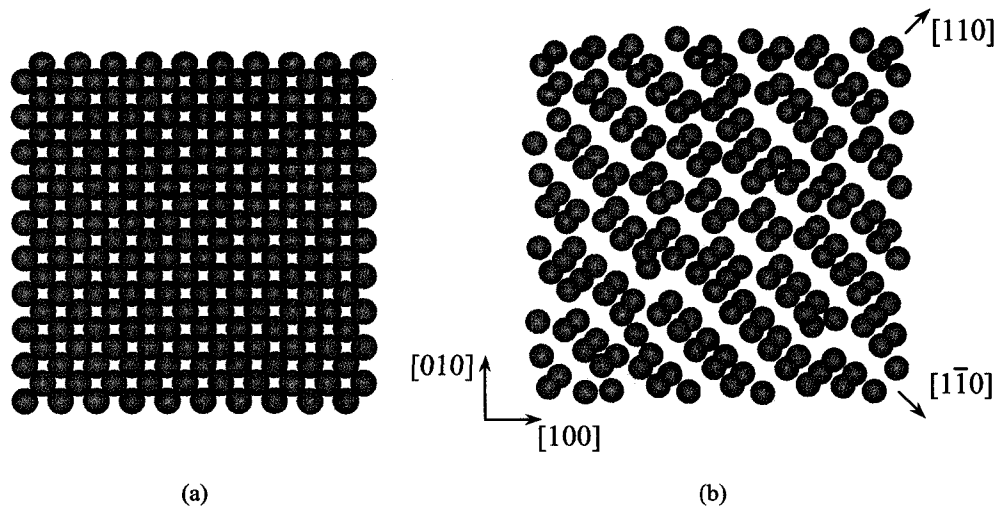


Figure 4.3.8. (a) Starting configuration of atoms located at the surface of a film of 10x10-silicon lattices cross section and 4.34 nm (8 lattices) thick. (b) Silicon surface reconstruction of the same thin film after 100,000 steps of molecular dynamics, showing the individual dimes oriented in [110] crystallographic direction and group of dimes aligning in the $[1\bar{1}0]$ direction.

Table 4.3.2 compares the computed distance between the atoms in a dime to those previously reported from molecular dynamics (Weakliem and Carter 1992; Yu and Clancy 1994), *ab initio* simulations (Yang, Jona et al. 1983) and experimental studies (Aono, Hou et al. 1982). Figure 4.3.8(b) and Table 4.3.2 show that the repulsive potential can reproduce the previously reported interatomic distances of the surface layer of the (100) silicon surface.

Table 4.3.2. Distance between atoms in a dime in a (100) reconstructed silicon surface, predicted by means of molecular dynamics (MD), *ab initio* simulations and Low-Energy Ion Scattering Spectroscopy (ISS) studies.

Technique	Distance (Å)
MD at 1510 K (Yu and Clancy 1994)	2.46
MD at 300 K (Weakliem and Carter 1992)	2.42
MD at 1000 K [this work]	2.40
<i>ab initio</i> (Yang, Jona et al. 1983)	2.54
ISS (Aono, Hou et al. 1982)	2.4±0.1

4.4 In-Plane Thermal Conductivity Calculations

This section compares the predicted silicon thin film thermal conductivity computed using the proposed boundary condition with two other boundary conditions: frozen atoms and free surfaces. The MD-predictions are compared to the available experimental data at 300 K (Liu and Asheghi 2004; Liu and Asheghi 2005).

4.4.1 Simulation domain and boundary conditions definition

The thermal conductivity of silicon thin films is predicted at thicknesses of 2.172, 3.258, 4.344, 5.43, 6.516, 8.688, 13.032, 17.376, 34.75, 81.45, 108.6, 135.75, 190.05 and 217.2 nm (corresponding to 4, 6, 8, 10, 12, 16, 32, 64, 150, 200, 250, 350 and 400 silicon lattice constants in the out-of-plane direction). The molecular dynamics temperature (T_{MD}) ranges from 300 to 1000K. Since thin films are characterized by having lateral dimensions considerably larger than their thicknesses, periodic boundary conditions are used in the in-plane direction to simulate a system that is infinite in the lateral dimensions while using a finite number of atoms, Fig. 4.1.1. Repulsive potentials are added to the Stillinger-Weber potential of the atoms that are near the surfaces, Fig. 4.4.1(a). Simulations are also performed using free surfaces, Fig. 4.4.1(b), and adding four layers of atoms kept frozen at their bulk equilibrium position to each surface, Fig. 4.4.1(c), in order to compare the dependence of the predicted in-plane thermal conductivities on the surface boundary conditions. The layer of frozen atoms does not contribute to the thermal conductivity, and the film thickness, d_s , is measured between the centers of the atoms of the first non-frozen layers.

The simulations with free surface boundary conditions conserve energy, and once the simulations are stabilized and the linear momentum in the out-of-plane direction has been cancelled, the number of atoms and volume are constant. Therefore, the ensemble is canonical and the Green-Kubo relation can be used to predict the thermal conductivity. Additionally, it can be proved that the time average of the energy flowing through the film surfaces for the frozen atoms boundary condition is zero and, since the volume and number of atoms are constant, the Green-Kubo relation can be used for the prediction of the in-plane thin film thermal conductivity.

The three boundary conditions used to handle the interface between the film computational domain and the surrounding media represent adiabatic boundary conditions when they are seen from a continuum frame of reference. However, these boundary conditions may represent different thermal transport processes when they are applied at the atomistic level for short time scales of the order of picoseconds.

The free surface boundary condition represents an adiabatic surface, in which there is no net energy transfer through the surface at any time scale. For this free surface boundary condition, all the energy of the phonons that scatter with the film surface is reflected back to the film.

The repulsive potential boundary condition resembles a continuum convective boundary condition, in which the film behaves as it is surrounded by an isothermal environment. Heat is transferred to and from the isothermal environment, with a frequency of approximately 33 THz, such that the time average of the net heat flux through the surface is zero. This means that the portion of the phonons' energy that scatters with the surface is absorbed by the surrounding environment. The remaining of the scattered phonons' energy is reflected back into the film. At the same time, the isothermal environment transfers energy into the thin film.

The frozen atoms boundary condition resembles two solids in thermal contact with null phonon transmission through the solid-solid interface. The phonons propagating toward the solid-solid interface are scattered with the interface and are reflected back into the thin film. For this boundary condition, the

scattering process is affected by the immobility of the frozen atoms since the atoms kept frozen impose a stiffer constraint than that imposed by either the repulsive potential or the free surface boundary conditions.

For the three boundary conditions described above, phonons that scatter with the surface are reflected into the film. The reflection has some degree of diffusivity, which is attested by the reduction of the thermal conductivity with the film thickness reduction. It is the diffusive phonon-boundary scattering process which accounts for the reduction on the thermal conductivity since a specular boundary condition does not affect the phonons propagating in the in-plane direction and therefore would not induce a reduction of the thermal conductivity. However, which phonons (characterized by wavevector, branch, polarization and frequency) are reflected diffusively and which ones are reflected specularly is still a subject of open discussion.

The computational domain for the three types of boundary conditions considered consists of 2×2 lattice constants in the in-plane directions (the simulation cross-section), with periodic boundary conditions. Each simulation is repeated three times with different initial atomic velocities for statistical purposes. The value of the thermal conductivity is obtained from the time integral of the heat current autocorrelation function. The upper limit of the time integral is larger than the time it takes for the autocorrelation function to decay to zero. The simulations are typically stabilized for 100,000 molecular dynamics steps, during which the temperature is scaled every ten time steps to compensate for the kinetic energy transformed into potential energy. The neighbor list for simulations with repulsive potentials (Gomes, Madrid et al. 2003) and free boundaries is updated every 25 time steps to properly account for silicon-silicon bond formation during the surface reconstruction process. Initially, the neighbor list for simulations with frozen atoms as boundary conditions was updated, but this practice was dropped once it was verified that the frozen atoms boundary conditions do not allow the reconfiguration of the first non-frozen atomic layer.

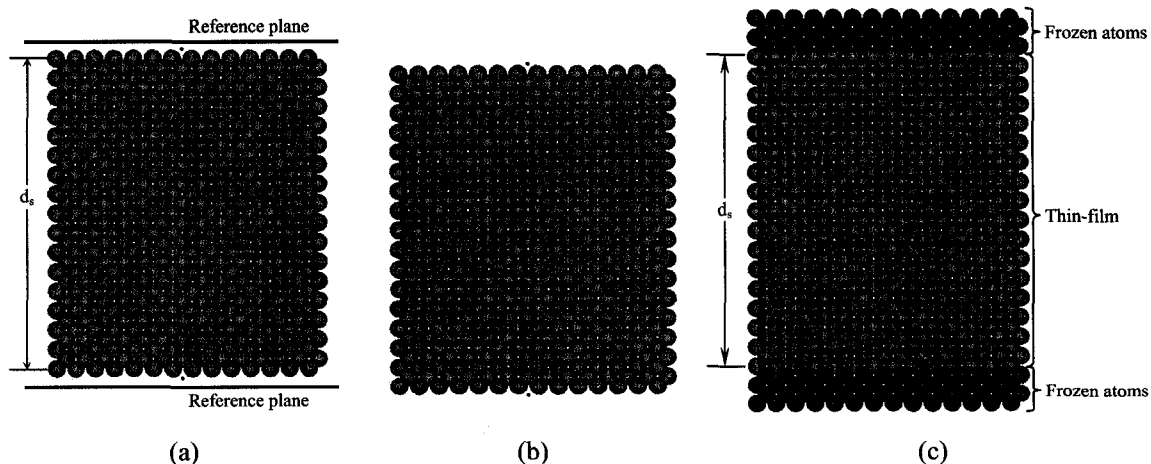


Figure 4.4.1. Front view of: (a) Silicon film with repulsive potential at both free surfaces. (b) Silicon film with free surfaces. (c) Silicon film with four layers of frozen atoms delimiting each surface.

4.4.2 Results

In this section we report the silicon thin film in-plane thermal conductivities predictions at $T_{MD} = 400$ and 1000 K. The in-plane thermal conductivity at $T_{MD} = 400$ K is compared to existing experimental silicon thin film thermal conductivity data (Ju and Goodson 1999; Liu and Asheghi 2004; Liu and Asheghi 2005). The prediction of the in-plane thermal conductivity at 1000 K allows the verification of bulk behavior as the film's thickness increases. A smaller film thickness is required to reproduce bulk thermal conductivity magnitude at 1000 K than at 300 K due to the smaller phonon mean free path at higher temperatures. The silicon phonon mean free path is estimated from the kinetic theory as 30 nm at 1000 K, and from the reduction of the bulk thermal conductivity by a factor given by the Boltzmann equation (Ju and Goodson 1999) as 300 nm at 300 K.

Figure 4.4.2 compares the predicted in-plane thermal conductivity (for all the boundary conditions used) to the available experimental data at 300 K. The temperature of the MD simulation is $T_{MD} = 400$ K, which, according to Table 2.2.2, Section 2.2.5, corresponds to quantum-corrected temperatures of 375 K or 305 K, depending on whether the quantum correction is computed from the experimental specific heat or analytically, respectively. Figure 4.4.3 shows the predicted in-plane thermal conductivity at 1000 K for the three boundary conditions used. A fitting curve of the form $a d_s / (b + d_s)$ is adjusted using minimum squares to the in-plane thermal conductivity predicted using the repulsive potential. The mathematical form of the fitting curve is chosen because it goes to zero as d_s goes to zero and it approaches a as d_s grows. The parameter a in the fitting equation represents the bulk thermal conductivity. The parameters a and b resulting from the fittings are reported in the respective figures. Figures 4.4.2 and 4.4.3 show that the predicted in-plane thermal conductivity decrease as the film's thickness decreases except for $d_s < 10$ nm when frozen atoms are used as boundary conditions. Special attention to this finding will be given latter in this section.

We observe good agreement, within the standard deviation, between the MD-predictions and the experimental data for film thicknesses larger than approximately 74 nm. The discrepancy between the MD-predictions and the experimental data is larger at smaller thickness. Molecular dynamics simulations have been performed assuming crystallographically perfect films of 100% ^{28}Si , while the experimental samples could contain silicon isotopes and vacancies. Scattering with the isotopes and vacancies could reduce the thermal conductivity at 300 K. In addition, a limitation of the molecular dynamics methodology is that does not account for quantum effects, which might be important at 300 K, especially at small thickness. These quantum effects might not be adequately accounted for by the correction factors described in section 2.2.5.

The predicted in-plane thermal conductivity at 1000 K (Fig. 4.4.3) increases monotonically with the film's thickness reaching a plateau of approximately 34 W/mK at a film thickness of approximately 75 nm. The thermal conductivity's plateau is consistent with the experimentally determined thermal conductivity of bulk single-crystal natural silicon at 1000 K, which ranges from 31 W/mK (Glassbrenner and Slack 1964) to 33 W/mK (Ho, Powell et al. 1972). The predicted thermal conductivity at $T_{MD} = 400$ K (Fig. 4.4.2) shows a plateau at a larger film thickness than at 1000 K, corroborating that the film thickness required to

reproduce bulk behavior in the in-plane direction is larger at $T_{MD} = 400$ K than at 1000 K. These results are attributed to a larger phonon mean free path at 300 K.

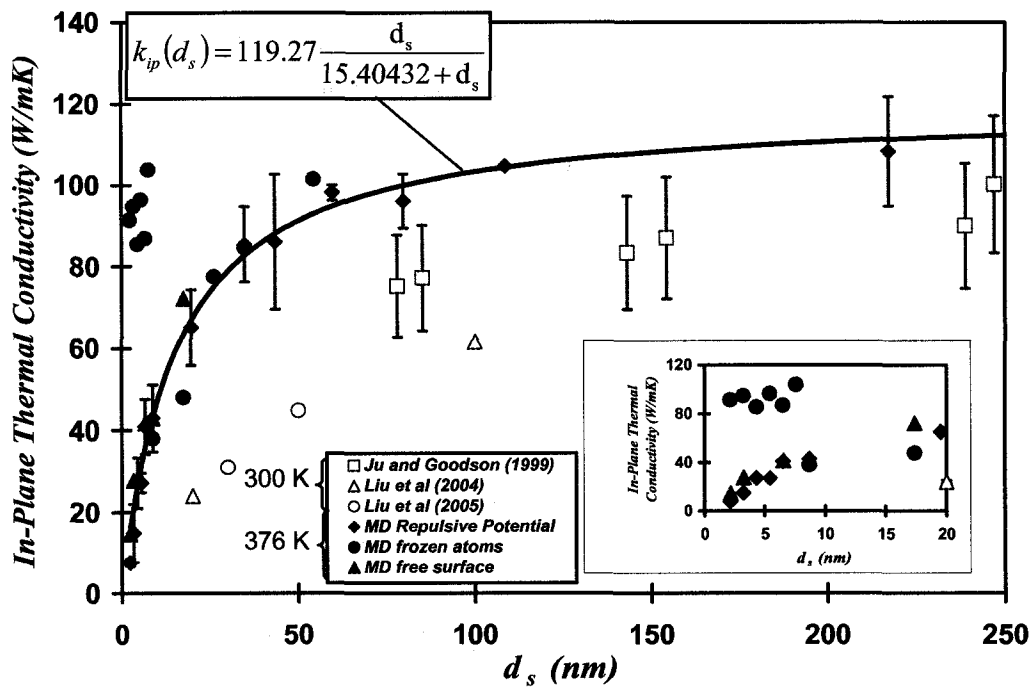


Figure 4.4.2. In-plane silicon thin film thermal conductivity at 300 K.

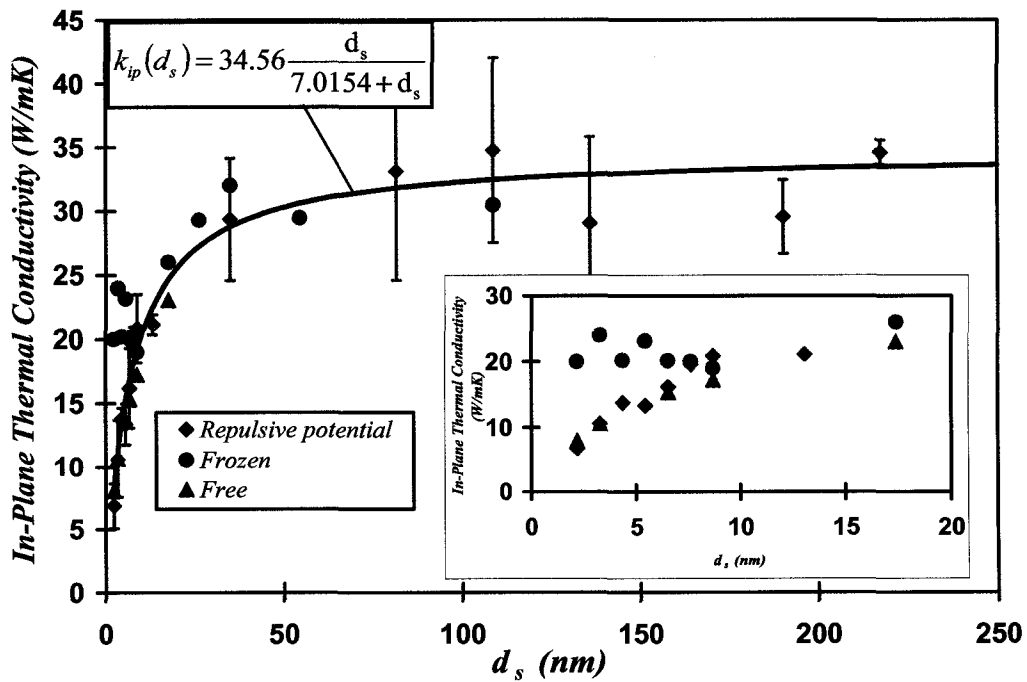


Figure 4.4.3. In-plane silicon thin film thermal conductivity at 1000 K.

Figures 4.4.2 and 4.4.3 show that the in-plane thermal conductivities predicted with the repulsive potential and with atoms kept frozen are within the statistical error, about 20%, of each other for film's thickness above ~10 nm. However, for film thicknesses below ~10 nm the thermal conductivity predicted using frozen atoms increases as the film thickness decreases, while the thermal conductivity predicted using either repulsive potential or free surfaces decreases as the film's thickness decreases.

The increase of the thermal conductivity predicted using frozen atoms for film's thicknesses smaller than ~10 nm is explained as follow. The two-dimensional radial distribution function, Eq. (4.4.1), gives an indication of the atomic structure by computing the relative distance amongst the atoms contained in an ensemble.

$$g_r(r) = \frac{1}{N_{atoms} \cdot N_s} \sum_{i=1}^{N_s} \sum_{j=1}^{N_{atoms}-1} \sum_{k=j+1}^{N_{atoms}} \left\{ \begin{array}{l} 2 \quad \text{if } \left| \sqrt{(x_j - x_k)^2 + (y_j - y_k)^2} - r \right| < \text{binwidth} \\ 0 \quad \text{otherwise} \end{array} \right\} \quad (4.4.1)$$

number of atoms at the solid's density occupying the same bin area

where N_s is the number of samples, N_{atoms} is the number of atoms in a layer and *binwidth* is the width of the bin at the radial distance r . Figure 4.4.4 shows the two-dimensional radial distribution function of the center, third, second and surface layers of a 7x7x8 lattice constant thin film ($d_s = 4.34$ nm) simulated at 1000 K with periodic boundary condition in the in-plane direction and repulsive potential, atoms kept frozen or vacuum (free) boundary condition in the out-of-plane direction. The two-dimensional radial distribution functions reported in Fig. 4.4.4 are computed using 2000 bins of width 0.0027 nm.

Figure 4.4.4(a) shows that the atoms at the film's center layer vibrate with the same relative amplitude (width of the peaks at their base) and that the atoms are located at the same relative equilibrium distances (peak location) for the three boundary conditions considered. However, the two-dimensional radial distribution function of the third, second and surface layers, Figs. 4.4.4 (b)-(d), show that, for the frozen atoms boundary condition, the amplitude of vibration of the atoms decrease as the distance of the layer to the film's surface decreases. This is shown by the narrowing of the peaks at their base and the increment on peaks' amplitude. In other words, the first non-frozen layers of atoms vibrate quasi-harmonically, dividing the film's thickness in three zones; two zones: one at each film surface, that behave quasi-harmonically and a third zone, the film core, that behaves an-harmonically.

The contribution of the in-plane thermal conductivity of the quasi-harmonic zones might be larger than the contribution to the thermal conductivity of the an-harmonic zone, because quasi-harmonic behavior inhibits phonon-phonon scattering. Therefore, for relatively thick films (thicknesses larger than ~10 nm), where the ratio of the quasi-harmonic zones to the an-harmonic zones seems to be negligible, the in-plane thermal conductivity is given by the an-harmonic zone. However, for film thicknesses smaller than ~10 nm, the ratio of the quasi-harmonic zone to the an-harmonic zone becomes significant; therefore, the thermal conductivity is given by the quasi-harmonic zone. The quasi-harmonic behavior close to the film's surfaces inhibits phonon-phonon interactions, but not phonon-surface scatterings. Therefore, the reduction on the

magnitude of the thermal conductivity due to the surface scattering is still present but it influences the phonons traveling in the core of the film rather than the phonons propagating in the quasi-harmonic zone. This is because a phonon propagating entirely in the quasi-harmonic zone (which should be smaller than 10 nm considering our results) would propagate parallel to the surface and therefore would not scatter with the surface, while phonons propagating in the core would propagate parallel or diagonal to the surfaces scattering with them.

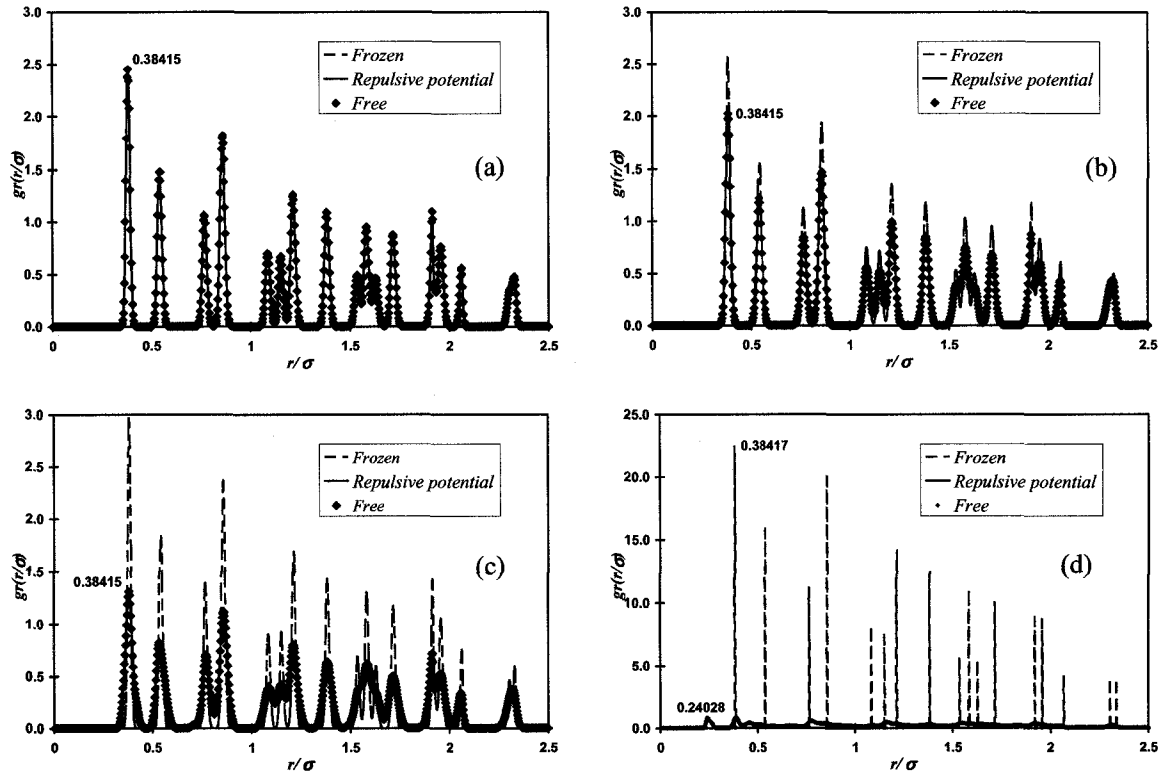


Figure 4.4.4. Two-dimensional radial distribution function for the film's (a) center layer, (b) third layer from the surface, (c) second layer from the surface and (d) the surface layer. The two-dimensional radial distribution function computed using the repulsive potential and free boundary condition are overlap in all the plots.

Additionally, Figs. 4.4.2 and 4.4.3 show that the in-plane thermal conductivity predicted with the repulsive potential and with free surfaces agree very well for all the film thickness investigated. Thus, in the thin film limit, the atomic trajectories simulated with the repulsive potential and with free surfaces are similar.

Table 4.4.1 presents the variation of the ratio of the predicted in-plane thermal conductivity to the experimental bulk thermal conductivity (Ho, Powell et al. 1972) with the film thickness at 376 and 1000 K. It seen that the in-plane thermal conductivity approaches the bulk silicon experimental value faster at 1000 K than it does at 376 K, a consequence of the smaller phonon mean free path at 1000 than at 376 K. Table 4.4.1 also reports the bulk silicon thermal conductivity predicted using the interpolation functions fitted to

the predicted in-plane thermal conductivity, Figs. 4.4.2 and 4.4.3. The extrapolated bulk thermal conductivity shows an excellent agreement with the experimental data at both temperatures.

4.4.3 In-plane silicon thin films thermal conductivity: Additional results

Figure 4.4.5 shows the predicted in-plane thermal conductivity as a function of the molecular dynamics temperature for different film thicknesses using repulsive potentials as boundary condition. The results show that the in-plane thermal conductivity in the very thin limit is temperature independent, within the standard deviation. In the very thin limit, where the film thickness is smaller than the phonon mean free path for all the molecular dynamics temperatures reported, the scattering of the phonons with the film's surfaces is the only scattering mechanism in our simulations, and therefore the in-plane thermal conductivity is independent of the molecular dynamics temperature. As the film's thickness increases and the phonon mean free path is determined by scattering with other phonons (normal and umklapp), the in-plane thermal conductivity becomes temperature dependent.

Table 4.4.1. Fraction of the in-plane thermal conductivity to the experimental bulk thermal conductivity at 376 and 1000 K.

d_s (nm)	Percentage of the bulk TC (%)	
	$T = 376$ K	$T = 1000$ K
2.17	6.87	20.70
3.26	13.39	32.12
4.34	24.43	41.83
5.43	24.54	40.52
6.52	41.80	49.02
7.60	- o -	59.33
8.69	38.68	63.22
13.03	- o -	64.09
19.55	58.55	- o -
34.75	76.91	88.97
43.44	77.45	- o -
59.73	88.36	- o -
79.82	86.51	- o -
81.45	- o -	100.35
108.60	94.29	105.34
217.20	97.47	104.83
Experimental value	111 W/mK	33 W/mK
Bulk thermal conductivity extrapolated using the fitting functions reported in Figs. 4.4.2 and 4.4.3	119.27 W/mK	34.56 W/mK

4.5 In-plane Autocorrelation Time

Figure 4.5.1 shows the in-plane thermal conductivity as a function of the time integral of the in-plane heat-current-autocorrelation-function, Eq. (4.3.5), for different film thicknesses, at 1000 K. Figure 4.5.1

shows that the time required for the heat-current-autocorrelation-function to decay to zero (the in-plane autocorrelation time), represented by the time at which each of the curves in Fig. 4.5.1 reaches their respective plateaus, decreases as the film thickness decreases. This reduction can be attributed to the presence of an additional scattering mechanism, not present in the bulk system, which makes the system lose the memory of its original state faster than in the bulk case. The effect of the *new* scattering mechanism, scattering with the surfaces, on the system increases as the film's thickness decreases. The reduction in the autocorrelation time indicates that the Green-Kubo formalism captures the phonon-surface scattering events.

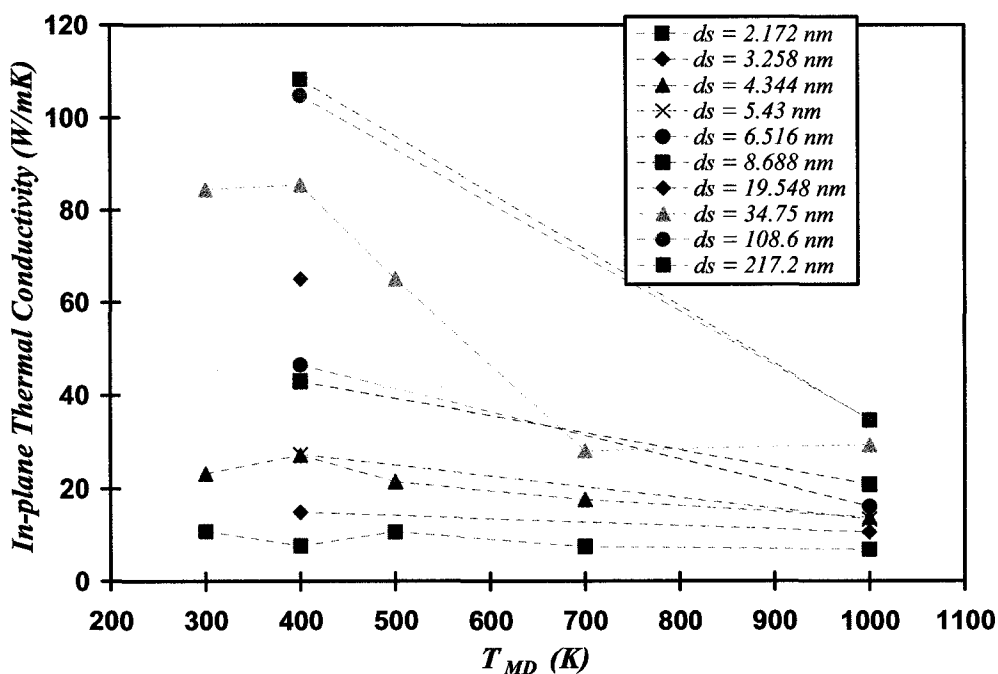


Figure 4.4.5. In-plane thermal conductivity vs molecular dynamics temperature for different film thicknesses.

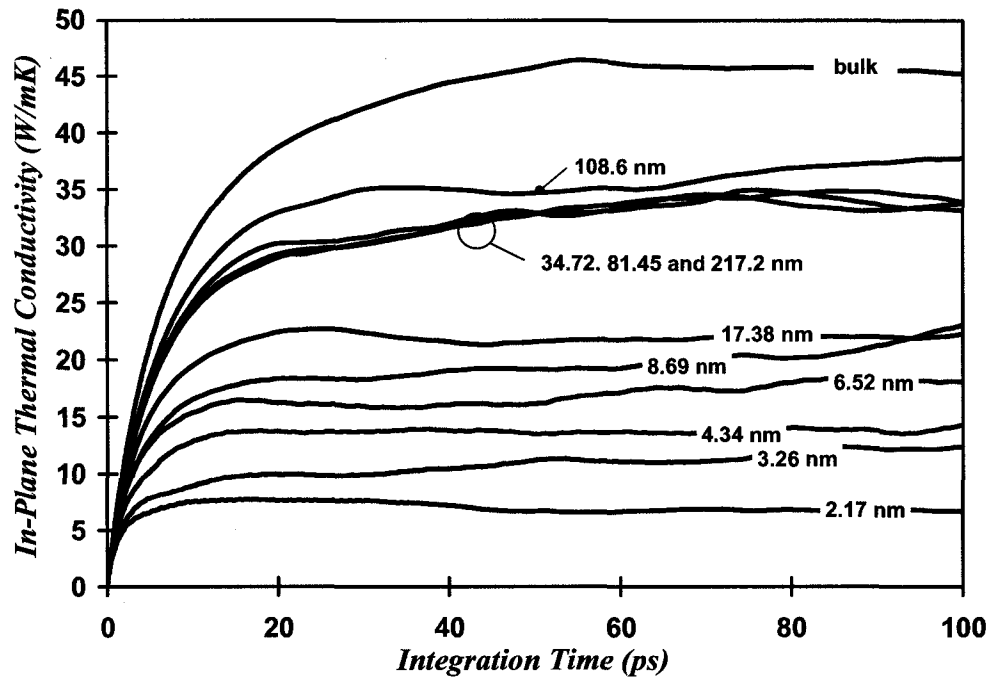


Figure 4.5.1. Variation of the time integral of the in-plane heat-current-autocorrelation-function for different film thickness.

4.6 Conclusions

A repulsive potential is proposed for treating the atoms located at the (100) silicon film surfaces during an equilibrium molecular dynamics prediction of in-plane thermal conductivity. The repulsive potential simulates the effect of a surrounding, macroscopically static gas, in thermal equilibrium with the thin film. It is verified that equilibrium molecular dynamics simulations using the repulsive potential conserve energy, number of atoms, and volume, and therefore are suitable for the prediction of in-plane thermal conductivity of thin films using the Green-Kubo formalism. The predicted in-plane thermal conductivity does not depend on the parameters chosen for the potential, as long as the potential is positioned such that the thin film is kept static in the out-of-plane direction. This indicates that other mathematical expressions for the repulsive potential could be experimented with, as long as the potential acts perpendicular to the film surfaces. The repulsive potential allows the reconstruction of the (100) silicon surfaces into aligned dimes. The orientation of the dimes and the inter-atomic distances in the dimes are in agreement with the available experimental data and to results of first principle studies.

Two additional strategies previously used to treat the surface atoms are used for our equilibrium molecular dynamics predictions of in-plane thin film thermal conductivity: adding four layers of atoms kept frozen at their equilibrium positions and free surfaces. The atoms kept frozen, the free surfaces and the repulsive potential strategies result in similar in-plane thermal conductivities predictions for film thicknesses larger than approximately ~ 10 nm at molecular dynamics temperatures of 400 and 1000 K.

Thus, in this limit, the predicted thermal conductivities do not depend strongly on the exact potential used to treat the surface atoms. However, in the very thin limit, there are significant differences in the predicted thermal conductivities with atoms kept frozen. The thermal conductivity predicted with frozen atoms is higher than the predicted with either the repulsive potential or free surfaces. Since the forces due to the repulsive potential act only in the direction perpendicular to the surfaces and do not affect the in-plane heat current, other effects must account for these differences. Delimiting the surface by four layers of atoms kept frozen at their crystallographic positions alters the vibration of the atoms adjacent to the frozen layers, as revealed by the planar radial distribution function, affecting the thermal conductivity.

The radial distribution function analysis and the agreement between the in-plane thermal conductivity predicted using the repulsive potential and free surfaces as boundary condition show that the repulsive potential boundary condition is more suitable for modeling the atomistic behavior of thin films over the film's thickness span considered in this work. Considering the difference between the atomic vibrations close to the film surfaces revealed by the planar radial distribution function, the repulsive potential could be more suitable than frozen atoms for predicting non-homogeneous properties close to the film's surfaces for thickness larger than ~ 10 nm.

The comparison of the predicted thermal conductivity to the experimental data at 300 K, the trends shown by the results at 300 and 1000 K and the reproducibility of bulk thermal conductivities for thick films at 1000 K indicate that equilibrium molecular dynamics and the Green-Kubo formalism can be used for the prediction of the lattice contribution to the in-plane thermal conductivity.

The predicted in-plane thermal conductivity for different temperatures and film thicknesses suggest that for small film thicknesses the scattering with the boundaries becomes the dominant scattering mechanism. In this limit, the in-plane thermal conductivity is independent of temperature. As the film thickness approaches the thick limit and the in-plane phonon flow is less influenced by the film surfaces, the predicted in-plane thermal conductivity becomes more dependent on temperature and approaches the bulk thermal conductivity magnitude.

The film thickness at which the in-plane thermal conductivity approaches the bulk value as the film becomes thick for different temperatures shows that the molecular dynamics simulations capture the variation of the phonon mean free path with temperature. The simulations are consistent with the fact that the phonon mean free path decreases as the temperature increases.

The reduction in the in-plane autocorrelation time as the film thickness decreases indicates that the Green-Kubo formalism is capable of capturing the phonon-surface scattering mechanism of phonons propagating in the in-plane direction.

4.7 References

- Allen, M. P. and D. J. Tildesley (1987). Computer Simulation of Liquids. Oxford, UK, Clarendon Press.
Aono, M., Y. Hou, et al. (1982). "Low-Energy Ion Scattering from the Si(001) Surface." Physical Review Letters **49**: 567-570.

- Chantrenne, P. and J.-L. Barrat (2003). "Finite Size Effect in Determination of Thermal Conductivities: Comparing Molecular Dynamics Results with Simple Models." Journal of Heat Transfer **in press**.
- Chantrenne, P. and J.-L. Barrat (2004). "Finite Size Effects in Determination of Thermal Conductivities: Comparing Molecular Dynamics Results with Simple Models." Journal of Heat Transfer **126**: 577-585.
- Feng, X.-L., Z.-X. Li, et al. (2003). "Molecular Dynamics Simulation of Thermal Conductivity of Nanoscale Thin Silicon Films." Microscale Thermophysical Engineering **7**: 153-161.
- Glassbrenner, C. J. and G. A. Slack (1964). "Thermal Conductivity of Silicon and Germanium from 3K to the Melting Point." Physical Review **134(4A)**: A1058-A1068.
- Gomes, C., M. Madrid, et al. (2003). Parallel Molecular Dynamics Code Validation Through Bulk Silicon Thermal Conductivity Calculations. 2003 ASME International Mechanical Engineering Congress and Exposition, Washington DC, ASME.
- Gomes, C., M. Madrid, et al. (2004). Thin Film In-Plane Silicon Thermal Conductivity Dependence on Molecular Dynamics Surface Boundary Conditions. 2004 ASME International Mechanical Engineering Congress and RD&D Expo, Anaheim, CA, ASME.
- Hardy, R. J. (1963). "Energy-Flux Operator for a Lattice." Physical Review **132(1)**: 168-177.
- Ho, C. Y., R. W. Powell, et al. (1972). "Thermal Conductivity of the Elements." Journal of Physical Chemistry Ref. Data **1**: 279-421.
- Hu, X., G. Wang, et al. (2004). "The Vibrational Density of States and Specific Heat of Si Nanocrystals." Journal of Physics: Condensed Matter **13(39)**: L835-L840.
- Ju, Y. S. and K. E. Goodson (1999). "Phonon scattering in Silicon Thin Films with Thickness of Order 100 nm." Applied Physics Letters **74(20)**: 3305-3307.
- Ju, Y. S. and K. E. Goodson (1999). "Phonon Scattering in Silicon Thin Films with Thickness of Order 100 nm." Applied Physics Letters **74(20)**: 3005-3007.
- Liu, W. and M. Asheghi (2004). "Phonon-Boundary scattering in Ultrathin Single-Crystal Silicon Layers." Applied Physics Letters **84(19)**: 3819-3821.
- Liu, W. and M. Asheghi (2004). Thermal Conductivity of Ultra Thin Single Crystal Silicon Layers, Part 1 - Experimental Measurements at Room and Cryogenic Temperatures. Proceedings of the 2004 ASME International Mechanical Engineering Congress and Exposition, IMECE 2004-62105, Anaheim, California.
- Liu, W. and M. Asheghi (2005). Thermal Conduction in Ultra-Thin Pure and Doped Single Crystal Silicon Layers at High Temperatures. 2005 ASME Summer Heat Transfer Conference, San Francisco, CA, USA.
- Lukes, J. R., D. Y. Li, et al. (2000). "Molecular Dynamics Study of Solid Thin-Film Thermal Conductivity." Journal of Heat Transfer **122**: 536-543.
- McGaughey, A. J. H. and M. Kaviani (2002). Molecular Dynamic Calculation of the Thermal Conductivity of Silica Based Crystal. 8th AIAA/ASME Joint Thermophysics and Heat Transfer Conference, St. Louis, MO.
- Porter, L. J., S. Yip, et al. (1997). "Empirical Bond-Order Potential Description of Thermodynamic Properties of Crystalline Silicon." Journal of Applied Physics **81(1)**: 96-106.
- Stillinger, F. H. and T. A. Weber (1985). "Computer Simulation of Local Order in Condensed Phases of Silicon." Physical Review B **31(8)**: 5262-5271.
- Volz, S. G. and G. Chen (1999). "Molecular Dynamics Simulation of Thermal Conductivity of Silicon Nanowires." Applied Physics Letters **75(14)**: 2056-2058.
- Weakliem, P. C. and E. A. Carter (1992). "Constant Temperature Molecular Dynamics Simulations of Si(100) and Ge(100): Equilibrium Structure and Short-Time Behavior." Journal of Chemical Physics **96(4)**: 3240-3259.
- Weakliem, P. C. and E. A. Carter (1992). "Constant Temperature Molecular Dynamics Simulations of Si(100) and Ge(100): Equilibrium Structure and Short-Time Behavior." Journal of Chemical Physics **96(4)**: 3240-3250.
- Yang, W. S., F. Jona, et al. (1983). "Atomic Structure of Si₂." Physical Review B **28(4)**: 2049-2059.
- Yu, Q. and P. Clancy (1994). "Molecular Dynamics Simulation of the Surface Reconstruction and Strain Relief in Si_{1-x}Ge_x/Si(100) Heterostructures." Modeling and Simulation in Material Science and Engineering **2**: 829-844.

Chapter 5:

Conclusions and Future Work

5.1 Conclusions

In this thesis we describe our equilibrium molecular dynamics studies, with the Green-Kubo formalism, of the lattice contribution to bulk and silicon thin film thermal conductivity. Previously, this approach has been applied to the study of the thermal conductivity of bulk materials. For the first time, we apply the Green-Kubo formalism to determine the thermal conductivity of silicon thin films, with thicknesses between 2 and 217 nm, and for temperatures of the simulations between 300 and 1000 K. We also perform a systematic study of the dependence of bulk silicon thermal conductivity on the simulation domain size and the temperature, for temperatures between 240 and 1000 K.

Since molecular dynamics is a classical method, it does not account for quantum effects, which are important at temperatures below the Debye temperature (which, for silicon is $\theta_D = \sim 625\text{K}$). In order to account for these quantum corrections, one protocol currently available in the literature equals the total energies per unit volume of the classical and phonon systems. Instead of using mathematical simplifications to predict the phonon energy and its derivative, we take advantage of the fact that the derivative of the phonon energy is the specific heat. The quantum corrections to the thermal conductivity are obtained from the experimental specific heat per unit volume. The integral of the specific heat gives the quantum corrections for the temperature. We believe this approach is more accurate because it uses experimental data, avoiding several mathematical simplifications. We show that for temperatures below the Debye temperature ($T < \theta_D$), the values of the quantum correction factors depend on the method used to calculate them (whether analytical or from the experimental specific heat), while the quantum corrections are negligible for temperatures much larger than the Debye temperature ($T \gg \theta_D$).

Molecular dynamics simulations performed using the Stillinger Weber potential predict bulk silicon thermal conductivities that are independent, within the statistical deviations, of the value of the equilibrium silicon lattice constant, for lattice constants of 0.543 and 0.545 nm, and molecular dynamics temperatures of 300 and 1000 K. Therefore, the experimentally determined silicon lattice parameter (0.543 nm at 295.7 K (Madelung 1996)) is used for the simulations at all temperatures.

An infinite system such as bulk silicon can be simulated by means of molecular dynamics by using a simulation domain consisting of a finite number of lattice constants, and applying periodic boundary conditions. Our molecular dynamics predictions show that silicon bulk thermal conductivity is independent of the size of the simulation domain, for simulation domains between $3 \times 3 \times 3$ and $10 \times 10 \times 10$ lattice constants, and temperatures between 240 and 1000 K. Thus, a relatively small simulation domain, with

periodic boundary conditions, can be used to predict bulk silicon thermal conductivity, with the consequent savings of computational time.

The use of periodic boundary conditions restricts the phonon wavelengths allowed in the simulation. The phonon wavelengths are discretized (only certain wavelengths are allowed), and there is a maximum possible wavelength. The effect of these phonon wavelength restrictions on the predicted bulk thermal conductivity is studied by solving the Boltzmann transport equation, excluding the forbidden wavelengths. The study shows that the BTE-predicted bulk thermal conductivity remains nearly constant with the number of lattice constants, when enough lattice constants and periodic boundary conditions are used. Although fewer phonons are allowed by the system, the relaxation times and the mean free paths of the allowed phonons increase. The increase in phonon relaxation time appears to compensate for the missing contribution to the thermal conductivity of the phonons not included in the simulation. In other words, the phonons allowed by the system carry the energy longer distances in their propagation direction before scattering with other phonons. The trend shown by the bulk thermal conductivity computed in this BTE study agrees with that shown by the molecular dynamics determined thermal conductivity. That is, the bulk thermal conductivities computed using relatively small simulation domains and periodic boundary conditions are within the statistical deviations of those computed using larger domains.

Predicting the thermal conductivity of thin films, whose surfaces are of physical importance, requires the inclusion of the actual surface in the atomistic simulation. This requires the inclusion of a large number of atoms in the simulation. Hence, there is a need for a computer code capable of managing large atomic systems within a reasonable amount of time. We developed a molecular dynamics code that incorporates the Stillinger-Weber potential for serial and massively parallel computers. The serial code was validated by comparing the location of a set of atoms after 100,000 molecular dynamics steps to the locations predicted using a serial shareware code (known as XMD), for the same initial conditions and integration algorithm. The atomic location was identical up to the eighth significant figure in reduced units. Then the serial code was used to validate the parallel code by comparing the atom locations of periodic and semi-periodic systems after 10^6 molecular dynamics steps. The parallel version of the code has been tested in two massively parallel computing systems Jaromir (CRAY T3E) and Lemieux (HP Alphaserver) at the Pittsburgh Supercomputing Center. The code ran on both platforms without the need of platform-specific modifications.

We next discuss our silicon thin film thermal conductivity studies. A repulsive surface potential is proposed for treating the atoms located at the (100) silicon film surfaces during an equilibrium molecular dynamics prediction of in-plane thermal conductivity. The repulsive potential simulates the effect of a surrounding, macroscopically static gas, in thermal equilibrium with the thin film. It is verified that equilibrium molecular dynamics simulations using the repulsive potential conserve energy, number of atoms, and volume, and therefore are suitable for the prediction of in-plane thermal conductivity of thin films using the Green-Kubo formalism. Our molecular dynamics simulations show that the predicted in-plane thermal conductivity does not depend on the parameters chosen for the potential, if the potential is

positioned such that the thin film is held static in the out-of-plane direction. This indicates that other mathematical expressions for the repulsive potential could be proposed, as long as the potential acts perpendicular to the film surfaces.

When a surface is created on the [100] crystallographic direction, the silicon atoms on the surface rearrange themselves into dimer, in order to minimize the number of dangling atomic bonds. The proposed repulsive potential allows for the rearrangement of the atoms on the (100) silicon surfaces into aligned dimers, thus providing a physically realistic representation of the film's surfaces. The orientation of the dimers and the inter-atomic distance of the atoms in the dimers are in agreement with experimental data and first principle studies.

For comparison purposes, we use two additional strategies, reported in the literature (Lukes, Li et al. 2000), to treat the surface atoms: 1. adding four layers of atoms kept frozen at their equilibrium positions, and 2. free surfaces. These two strategies or the repulsive potential result in similar in-plane thermal conductivity predictions, for film thicknesses larger than approximately ~ 10 nm, at 376 and 1000 K. Thus, for thicknesses larger than 10 nm, the predicted thermal conductivities do not depend strongly on the exact potential used to treat the surface atoms. However, for thinner films, there are significant differences in the in-plane thermal conductivities predicted with atoms kept frozen. The thermal conductivity predicted with frozen atoms is higher than that predicted with either the repulsive potential or free surfaces, and does not follow the experimentally observed trend of decreasing with decreasing film thickness. Since the forces due to the repulsive potential act only in the direction perpendicular to the surfaces and do not affect the in-plane heat current, other effects must account for these differences. Analysis of the radial distribution function show that delimiting the surfaces by four layers of atoms kept frozen at their crystallographic positions decreases the amplitude of vibration of the adjacent atoms, affecting the predicted in-plane thermal conductivity.

The radial distribution function analysis and the agreement between the in-plane thermal conductivity predicted using the repulsive potential or free surfaces as boundary conditions show that the repulsive potential boundary condition is more suitable than the frozen atoms strategy for modeling the atomistic behavior of thin films, over the films' thickness span considered in this work. In addition, while the molecular dynamics simulations using either the repulsive potential or free surfaces allow for the reconstruction of the silicon surfaces, simulations using atoms kept frozen do not. Considering the difference between the atomistic behaviors close to the film surfaces revealed by the planar radial distribution function, the repulsive potential surfaces strategy appears to be more suitable than frozen atoms for predicting non-homogeneous properties close to the free film's surfaces, for thickness larger than ~ 10 nm.

The predicted in-plane thermal conductivity decreases with decreasing film thickness, in agreement with the experimental data (Ju and Goodson 1999; Liu and Asheghi 2004; Liu and Asheghi 2005) at 300 K. This decrease suggests that, for film thicknesses smaller than the bulk phonon mean free path, the scattering with the boundaries becomes the dominant scattering mechanism. For thicknesses smaller than

~3 nm, the in-plane thermal conductivity is independent of temperature. As the film thickness approaches the thick limit (thickness larger than the bulk phonon mean free path), the in-plane phonon flow is less influenced by the film surfaces and the predicted thermal conductivity becomes more dependent on temperature. In the thick limit, the predicted in-plane thermal conductivity approaches the bulk thermal conductivity. The bulk thermal conductivity value is reached faster at 1000 K than at 300 K, due to the smaller phonon mean free path at higher temperatures. These results show that molecular dynamics simulations reproduce the expected variation of the phonon mean free path with temperature. The simulations indicate that the magnitude of the phonon mean free path decreases as the temperature increases.

In summary, the predicted in-plane thermal conductivities at 300 and 1000 K decrease with decreasing film thickness, and this tendency agrees with the experimental results at 300 K. As the film thickness increases, the thermal conductivity asymptotically approaches the experimental bulk value. This limit is reached faster at 1000 K, due to the smaller phonon mean free path at this temperature. These results indicate that equilibrium molecular dynamics and the Green-Kubo formalism can be used for the prediction of the lattice contribution to the in-plane thermal conductivity. The approach is capable of capturing the phonon-surface scattering mechanism of phonons propagating in the in-plane direction and the variation of the phonon mean free path with temperature.

5.2 Future Work

In this Section I suggest improvements to the molecular dynamics code and propose additional numerical studies for the in-plane thermal conductivity and new studies for the out-of-plane thermal conductivity

The molecular dynamics code expends most of the execution time computing the interatomic forces. Consequently, improvements to the interatomic force calculation function would considerably reduce the time per simulation. Some suggestions are:

1. The function that computes the interatomic distance to the nearest imaging needs to be optimized.
2. The interatomic distance calculation can be piped. Thus, the interatomic distance to the next atom (atom $i+1$) in the neighbor list should be computed while still computing the interatomic force with atom i in the neighbor list.
3. Since the interatomic distance has to be calculated and the Stillinger-Weber potential is composed of diverse mathematical functions, the Stillinger-Weber potential can be written as a piecewise linear interpolating function such that by using an appropriate length scaling factor the integer part of the interatomic distance would readily provide the index of the portion of the interpolating function.
4. Although the current codification for the interchanging of ghost atoms location and velocities works, it blocks the higher rank processors until the lower rank processors are done with the interchanging. A

more efficient coding could reduce the communication portion of the time per molecular dynamics step.

The planar radial distribution function reported in Chapter 4 revealed that the behavior of the atoms close to the films' surfaces depends on the type of boundary condition used to treat the surfaces. Moreover, the results show that the in-plane behavior of the atoms located at the center of the film is different than the behavior of the atoms near the surfaces of the film. That is, the atoms close to the film's surfaces vibrate with larger or smaller amplitude than the atoms at the center depending upon whether repulsive potential or frozen atoms are used as boundary conditions, respectively. These characteristics could lead to thermal transport properties that depend on the out-of-plane location and require further investigation. I am planning to perform numerical simulations using non-equilibrium molecular dynamics to predict the thermal conductivity of thin films as a function of the location with respect to the films surfaces.

5.3 References

- Ju, Y. S. and K. E. Goodson (1999). "Phonon Scattering in Silicon Thin Films with Thickness of Order 100 nm." Applied Physics Letters 74(20): 3005-3007.
- Liu, W. and M. Asheghi (2004). Thermal Conductivity of Ultra Thin Single Crystal Silicon Layers, Part 1 - Experimental Measurements at Room and Cryogenic Temperatures. Proceedings of the 2004 ASME International Mechanical Engineering Congress and Exposition, IMECE 2004-62105, Anaheim, California.
- Liu, W. and M. Asheghi (2005). Thermal Conduction in Ultra-Thin Pure and Doped Single Crystal Silicon Layers at High Temperatures. 2005 ASME Summer Heat Transfer Conference, San Francisco, CA, USA.
- Lukes, J. R., D. Y. Li, et al. (2000). "Molecular Dynamics Study of Solid Thin-Film Thermal Conductivity." Journal of Heat Transfer 122: 536-543.
- Madelung, O., Ed. (1996). Semiconductors Basic Data. Berlin, Springer-Verlag.

Appendix A:

Boltzmann Transport Equation

This appendix describes the mathematical formulation of the Boltzmann transport equation used for the analytical size artifact study presented in Chapter 3. Only the characteristics of the Boltzmann transport equation relevant to the size artifact study are presented. The full phonon dispersion model (Narumanchi 2003) is chosen over the gray model (Holland 1963) because the study is intended to expose the influence of artificially removing phonons from the atomistic system on the predicted thermal conductivity. The gray model (Holland 1963) incorporates the relaxation time of the phonons as a function of the phonon frequency and temperature, while the full dispersion model (Narumanchi 2003) incorporates the relaxation time as a function of the phonons involved in the scattering event and the temperature. The full dispersion model also incorporates phonon scattering rules (Han and Klemens 1993). It is assumed that the energy is transported by the acoustic phonons and that the optical phonons serve as energy reservoirs and resistance to the acoustic phonon flow.

A.1 Boltzmann Transport Equation in the Relaxation Time Approximation

The Boltzmann transport equation in the relaxation time approximation for acoustic phonons of frequency i and without source term is (Narumanchi 2003)

$$\frac{\partial f_i}{\partial t} + \vec{v}_i \cdot \nabla f_i = \sum_j \frac{f_{ij}^o - f_i}{\tau_{ij}} + \frac{f_{io}^o - f_i}{\tau_{io}} \quad (\text{A.1.1})$$

where f_i is the phonon distribution function for phonons of frequency i , v_i is the phonon propagation velocity in m/s, f_{ij}^o and f_{io}^o are the phonon equilibrium functions for phonon scattering between phonons i and j , and between phonons i and optical phonons, respectively, τ_{ij} and τ_{io} are the relaxation times for phonon-phonon scattering between acoustic phonons i and j and optical phonons (Han and Klemens 1993), respectively.

Equation (A.1.1) can be rewritten as

$$\frac{\partial f_i}{\partial t} + \vec{v}_i \cdot \nabla f_i = - \left(\sum_j \gamma_{ij} \right) f_i + \left(\sum_j \gamma_{ij} \right) f_{ij}^o + \gamma_{io} f_{io}^o \quad (\text{A.1.2})$$

where γ_{ij} is the inverse of the relaxation time in s^{-1} . The first summation is over all the phonon frequencies including the optical branch and the second summation is only over the acoustics branches.

A.2 Phonon Bands Approach

The Boltzmann transport equation presented in Eq. (A.1.2) is for phonons of frequencies i , which interact with phonons of frequencies j . Capturing the phonon behavior in a bulk-like domain requires solving Eq. (A.1.2) for each phonon frequency i , which is computationally expensive. Therefore, this analysis relies on the phonon bands approach (Narumanchi 2003), where the phonon dispersion curve is divided into phonon bands. The Boltzmann transport equation written using the phonon band approach is:

$$\frac{\partial \bar{f}_i}{\partial t} + \bar{v}_i \cdot \nabla \bar{f}_i = \left(\sum_j \bar{\gamma}_{ij} \right) \bar{f}_i + \left(\sum_j \bar{\gamma}_{ij} \right) \bar{f}_{ij}^o + \bar{\gamma}_{io} \bar{f}_{io}^o \quad (\text{A.2.1})$$

where the meaning of the quantities is the same as in Eq. (A.1.2) but here they represent the *average* over the frequency band i (with center at frequency i) instead of the value *at* frequency i . The averaged relaxation time represents the relaxation time between the phonon band i (or a portion of it) that overlaps with the phonon band j (or a portion it) according to Klemens' scattering rules (Klemens 1958).

The phonon band approach (Narumanchi 2003) divides the dispersion relation in equal size frequency bands. However, since the dispersion curves are not linear, this approach produces different size wavevector bands, which are not equally spaced. In order to accommodate the phonon wavelength restriction rules ($\lambda_i = L/i$, where L is the simulation domain length and i an integer from one to the number of lattice constants in a simulation direction) used in Chapter 3, the dispersion relation is divided in equally sized reduced wavenumber bands. Figure A.2.1 shows the dispersion relation for silicon (Holland 1963) divided in eight bands, using the constant size frequency band (a) and the constant size reduced wavenumber band (b).

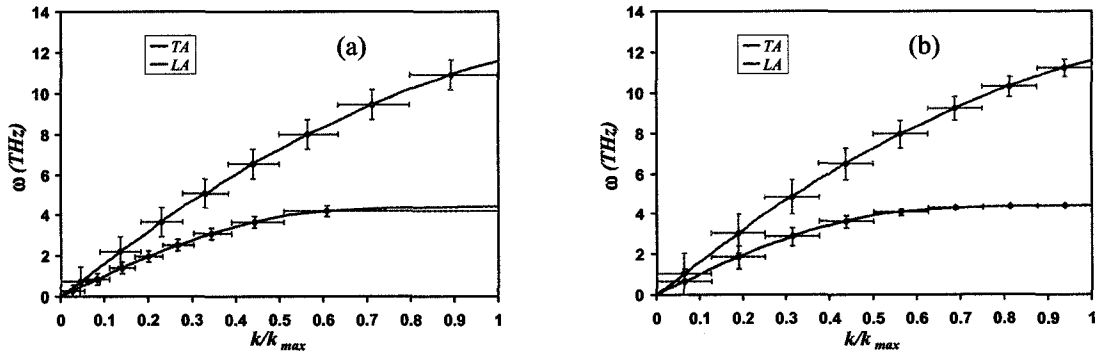


Figure A.2.1. Discrete acoustic dispersion curves using (a) equal size frequency bands and (b) equal size reduced wavenumber bands.

A.3 Bulk Thermal Conductivity Equation

The procedure to obtain an analytical expression for the thermal conductivity starting with the BTE is well documented elsewhere (Reif 1965; Liboff 1990; Tien, Majumdar et al. 1998). The main hypotheses are that the system is at steady state and that there is a small one-dimensional temperature gradient such that the gradient of the phonons' distribution function is approximated by the gradient of the equilibrium distribution function. Additionally, the problem of obtaining an analytical expression is further simplified by considering that the phonons' dispersion relation and velocities are isotropic and identical to those in the [100] crystallographic direction. Moreover, the first Brillouin zone is assumed spherical and the dispersion relation is assumed to be continuous. The analytical expression for the thermal conductivity is then:

$$K(T) = \frac{1}{3} \frac{k_B}{2\pi^2} [K_L(T) + 2K_T(T)] \quad (\text{A.3.1})$$

where $K(T)$ is the bulk silicon thermal conductivity in W/mK at temperature T , k_B is the Boltzmann constant, K_L and K_T are the longitudinal acoustic and transversal acoustic thermal conductivities, respectively. The longitudinal and transversal acoustic terms are both of the form

$$K_{L,T}(T) = \sum_i \tau_i(T) \cdot \Delta\omega_i \cdot \bar{v}_i \cdot k_i^2 \frac{x_i(T) \cdot e^{x_i(T)}}{(e^{x_i(T)} - 1)^2} \quad (\text{A.3.2})$$

where $\Delta\omega_i$ is the frequency band width, k_i is the wavevector at the center of the reduced wavevector bandwidth, τ_i is the band relaxation time and x_i is given by:

$$x_i(T) = \frac{\hbar \cdot \omega_i}{k_B \cdot T} \quad (\text{A.3.3})$$

where ω_i is the phonon frequency at k_i . The relaxation time τ_i in Eq. (A.3.2) is given by

$$\tau_i(T) = \frac{1}{\sum_j \bar{\gamma}_j(T)} \quad (\text{A.3.4})$$

where the summation j is over the phonon bands that scatter with the phonon band i , including the optical branch.

Figure A.3.1 shows the thermal conductivity computed using Eq. (A.3.2) with 50 equal size wavevector bands. The thermal conductivity predicted with six equal size frequency bands is also presented (Narumanchi 2003).

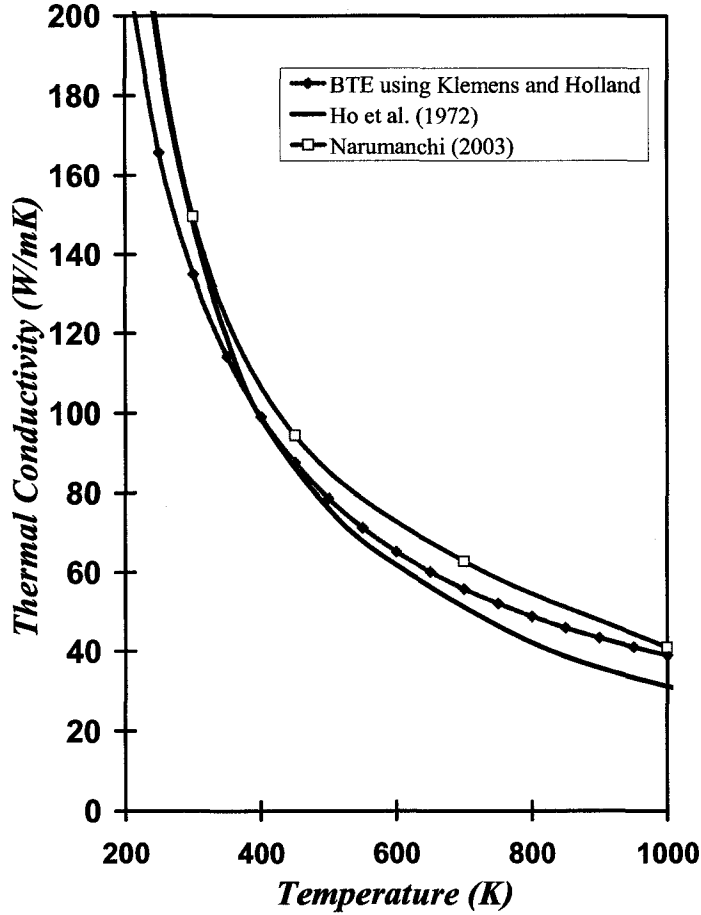


Figure A.3.1. Variation of the thermal conductivity with temperature, predicted using the Boltzmann transport equation.

A.4 Relaxation Times and Scattering Rules

The mathematical expressions for the relaxation times used in this work are those reported in (Han and Klemens 1993). The expressions are modified to compute the average relaxation time between phonon bands. The scattering rules implemented for this analysis are: $T+L_{zone} \leftrightarrow L$, $L+T_{zone} \leftrightarrow L$, $T+T_{zone} \leftrightarrow L$, $L+L_{zone} \leftrightarrow O$ and $T+L_{zone} \leftrightarrow O$; where the letters T, L and O refer to transversal, longitudinal and optical, respectively. The subscript “zone” refers to phonons at the border of the first Brillouin zone in the [100] crystallographic direction and the bidirectional arrow means that the scattering process could happen in either direction. The overlapping of the phonon bands are estimated using the energy conservation equation ($\omega \pm \omega_{zone} \leftrightarrow \omega'$) for the appropriate scattering rule. Figure A.4.1 shows, as an example of the scattering

rules, the portions of the longitudinal and transversal polarizations undergoing a $T+T_{\text{zone}} \leftrightarrow L$ scattering process while satisfying the energy conservation equation. Three scattering events are shown in Fig. A.4.1; the scattering events indicated with the path (a) and (c) are the limits of the range for which the energy conservation equation is satisfied for the $T+T_{\text{zone}} \leftrightarrow L$ scattering process. Path (a) corresponds to transversal acoustic phonons with nearly zero frequency, scattering with transversal acoustic phonons on the edge of the first Brillouin zone (T_{zone}) to produce longitudinal acoustic phonons of frequency similar to the latter according to the energy conservation equation. Path (c) corresponds to two transversal acoustic phonons on the edge of the first Brillouin zone where they scatter with each other to produce a longitudinal acoustic phonon with a frequency twice the frequency of the transversal acoustic phonon. Path (b) represents an allowed scattering process within the limits (a) and (c). The longitudinal acoustic phonons to the left of the path (a) and to the right of the path (c) cannot undergo a $T+T_{\text{zone}} \leftrightarrow L$ scattering process since these portions of the longitudinal acoustic curve do not satisfy the energy conservation equation.

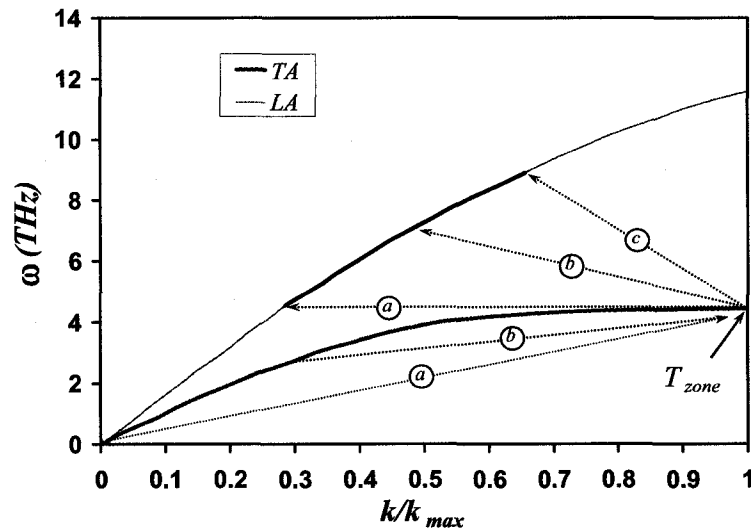


Figure A.4.1. Longitudinal and transversal polarizations that undergo $T+T_{\text{zone}} \leftrightarrow L$ scattering processes while satisfying energy conservation.

Figures A.4.2(a)-(e) show the average relaxation time per phonon band for the longitudinal and transversal acoustic polarization for each of the possible scattering rules. The relaxation times are computed using 50 phonon bands per acoustic polarization and one phonon band for the optical branch. The portions of the plots without symbols indicate that those phonon bands do not scatter with the others for the specific scattering rule and energy conservation equation. Figure A.4.2(f) shows the phonon band relaxation time computed by adding the relaxation time from each scattering process using Matthiessen's rule, Eq. (A.3.4) (Srivastava 1990). Matthiessen's rule states that given multiple relaxation times due to possible different scattering processes, the relaxation time of a phonon band is the inverses of the sum of the inverse of the relaxation times. Computing the relaxation time using Matthiessen's rule ensures that the magnitude of the resultant relaxation time is dominated by the smaller of the individual relaxation times. This last

observation is seen in Fig. A.4.2(f) where, for instance, the relaxation time of the transversal polarization, in the frequency range where multiple phonon scattering rules apply, is dominated by the relaxation time of the $T+L_{\text{zone}} \leftrightarrow O$ scattering rule, Fig. A.4.2(e).

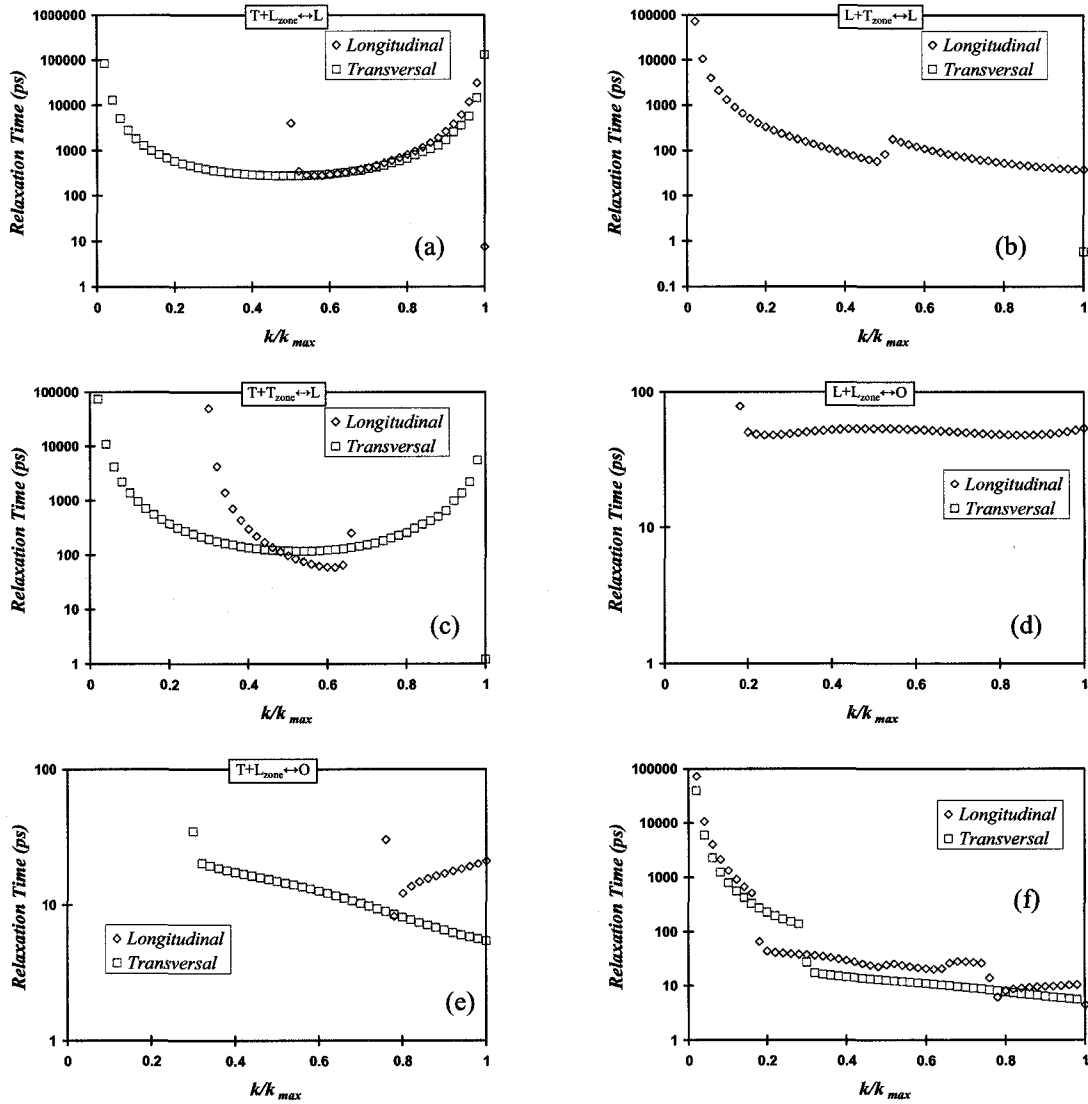


Figure A.4.2. Phonon band relaxation times vs. reduce wavevector for (a) $T+L_{\text{zone}} \leftrightarrow L$, (b) $L+T_{\text{zone}} \leftrightarrow L$, (c) $T+T_{\text{zone}} \leftrightarrow L$, (d) $L+L_{\text{zone}} \leftrightarrow O$, (e) $T+L_{\text{zone}} \leftrightarrow O$ scattering rules, and (f) total relaxation time.

The discontinuities in the phonon band relaxation times reported in Fig. A.4.2(f) are due to the range of applicability of the scattering rules and the relative magnitude of the relaxation times for the different scattering processes. For instance, the discontinuity shown at $k/k_{\text{max}} \sim 0.3$ on the transversal acoustic relaxation times is due to the range of applicability of the $T+L_{\text{zone}} \leftrightarrow O$ scattering rule, Fig. A.4.2(e). Notice that the discontinuities in the phonon band relaxation times are the source of the discontinuities in the phonon band contribution to the thermal conductivity reported in Section 3.3.2, Figs. 3.3.5 and 3.3.7.

Phonons with short wavevectors interact weakly with all the other phonons; therefore the relaxation times of phonons with short wavevectors are larger than the relaxation times of all the other phonons, Figs. A.4.2(a)-(e). This accounts for the larger contribution to the thermal conductivity of the phonon bands with short wavevectors reported in Chapter 3. The weak interaction also explains why the contribution to the thermal conductivity of the phonon bands with wavevectors larger than the cutoff wavevector enforced in Chapter 3 is not altered by the removal of the small-wavevector phonons presented in Fig. 3.3.5, Chapter 3.

A.5 Phonon Wavelength Restriction

The phonon wavelength restriction enters the thermal conductivity predictions through the summation index i in Eq. (A.3.2) and the summation index j in Eq. (A.3.4). The summation index i is only over phonon bands with center at reduced wavenumbers $1/p$, where p is an integer ranging from one to the number of lattice constant per simulation domain side. The index j includes only the scattering between the phonon bands included through the index i , according to Klemens' scattering rules.

A.6 References

- Han, Y.-J. and P. G. Klemens (1993). "Anharmonic Thermal Resistivity of Dielectric Crystals at Low Temperatures." Physical Review B **48**(9): 6033-6042.
- Holland, M. G. (1963). "Analysis of Lattice Thermal Conductivity." Physical Review **132**(6): 2461-2471.
- Klemens, P. G. (1958). Thermal Conductivity and Lattice Vibrational Modes. Solid State Physics. F. Seitz and D. Turnbull. New York, Academic Press. **7**: 1-98.
- Liboff, R. L. (1990). Kinetic Theory: Classical, Quantum, and Relativistic Descriptions, Prentice Hall.
- Narumanchi, S. V. J. (2003). Heat Transport in Sub-micron Conduction. Mechanical Engineering. Pittsburgh, Ph.D. thesis, Carnegie Mellon University.
- Reif, F. (1965). Fundamentals of Statistical and Thermal Physics. New York, M^cGraw-Hill.
- Srivastava, G. P. (1990). The Physics of Phonons. New York, Adam Hilger.
- Tien, C.-L., A. Majumdar, et al., Eds. (1998). Microscale Energy Transport. Series in Chemical and Mechanical Engineering. Washington DC, Taylor and Francis.

Appendix B:

Molecular Dynamics Thermal Conductivity Data

This appendix contains the predicted thermal conductivity data reported in this thesis. The predicted bulk thermal conductivity is reported in Section B.1 and the in-plane thin film thermal conductivity is reported in Section B.2.

B.1 Bulk Thermal Conductivity

Table B.1.1 reports the predicted bulk thermal conductivity reported in Chapter 3. The temperatures and thermal conductivities are reported before quantum corrections and the lattice constant is 0.543 nm.

Table B.1.1. Bulk silicon thermal conductivity.

Simulation domain size in number of lattice constants	Thermal Conductivity (W/mK)			
	300 K	500 K	700 K	1000 K
2x2x2	- o -	159.68	57.84	- o -
3x3x3	293.22	172.66	84.16	38.75
4x4x4	344.66	- o -	95.50	46.67
5x5x5	297.00	182.49	97.38	51.02
7x7x7	- o -	- o -	93.68	- o -
10x10x10	340.99	180.30	88.80	- o -

B.2 In-Plane Thin Film Thermal Conductivity

Tables B.2.1, B.2.2 and B.2.3 report the predicted in-plane thin film thermal conductivity predicted using repulsive potential, atoms kept frozen and free surfaces, respectively. The temperatures and thermal conductivities are reported before quantum corrections. The predictions were done using a 2x2 lattice constant cross section and the lattice constant is 0.43 nm.

Table B.2.1. In-plane thin film thermal conductivity predicted using the repulsive potential.

d_s		Thermal Conductivity (W/mK)							
lattice constants	nm	300	400	433	475	500	520	700	1000
4	2.17	15.33	9.03			11.81		7.85	6.83
6	3.26		17.59						10.60
8	4.34	32.99	32.08			23.86		18.54	13.80
10	5.43		32.23						13.37
12	6.52		54.90						16.18
14	7.60								19.58
16	8.69		50.80						20.86
24	13.03								21.15
36	19.55		76.90	65.37	57.38		75.68		
64	34.75	120.03	101.01			72.25		29.44	29.36
80	43.44		101.72						
110	59.73		116.04						
147	79.82		113.62						
200	108.60		123.83	159.87	84.92		108.13		34.76
250	135.75								29.04
350	190.05								29.55
400	217.20		128.00						34.59

Table B.2.2. In-plane thin film thermal conductivity predicted using atoms kept frozen.

d_s		Thermal Conductivity (W/mK)				
lattice constants	nm	300	400	500	700	1000
4	2.17	114.73	108.00	57.00	34.00	20.00
6	3.26		112.00			24.00
8	4.34		101.00			20.21
10	5.43		113.89			23.15
12	6.52		102.66			20.12
14	7.60		122.66			19.99
16	8.69		45.00			19.00
32	17.38		56.75			26.00
48	26.06		91.61			29.29
64	34.75		100.00	143.00	60.00	32.00
100	54.30		120.00			29.46
200	108.60					30.45

Table B.2.3. In-plane thin film thermal conductivity predicted using free surfaces.

d_s		Thermal Conductivity (W/mK)	
lattice constants	nm	400	1000
4	2.17	17.23	8.01
6	3.26	32.80	10.66
12	6.52	49.31	15.34
16	8.69	50.67	17.25
32	17.38	85.29	23.07